

# REPORT DOCUMENTATION PAGE

AFRL-SR-BL-TR-01-

0008

Public reporting burden for this collection of information is estimated to average 1 hour per response, including the time for reviewing the collection of information, Send comments regarding this burden estimate or any other aspect of this collection of information, including suggestions for reducing this burden to Washington Headquarters Service, Directorate for Information Operations and Reports, Paperwork Reduction Project (0704-0188) Washington DC 20503  
PLEASE DO NOT RETURN YOUR FORM TO THE ABOVE ADDRESS.

1. REPORT DATE (DD-MM-YYYY) 29/11/2000		2. REPORT DATE Final Report		3. DATES COVERED: (From - To) June 1996-Dec. 1998	
4. TITLE AND SUBTITLE  Nonlinear Control using Forebody Tangential Blowing				5a. CONTRACT NUMBER N/A	
				5b. GRANT NUMBER F49620-96-1-0248	
				5c. PROGRAM ELEMENT NUMBER N/A	
6. AUTHOR(S)  Takahara, Yuji Rock, Stephen				5d. PROJECT NUMBER N/A	
				5e. TASK NUMBER N/A	
				5f. WORK UNIT NUMBER N/A	
7. PERFORMING ORGANIZATION NAME(S) AND ADDRESS(ES) Stanford University 651 Serra Street Stanford, CA 94305				8. PERFORMING ORGANIZATION REPORT NUMBER N/A	
9. SPONSORING/MONITORING AGENCY NAME(S) AND ADDRESS(ES) Dr. Marc Jacobs AFOSR/NM 801 North Randolph Street Room 732 Arlington, VA 22203-1977				10. SPONSOR/MONITOR'S ACRONYM(S) AFOSR/NM	
				AGENCY REPORT NUMBER N/A	
12. DISTRIBUTION AVAILABILITY STATEMENT Unlimited					
13. SUPPLEMENTARY NOTES N/A					
14. ABSTRACT Forebody Tangential Blowing (FTB) is a pneumatic device that modifies the vortical flow over the forebody of an aircraft operating at high angles of attack. Modified vortical flow in turn creates roll and yaw moments for control. Consequently, it provides a mechanism that could greatly expand the flight envelope of future aircraft systems. One major factor that currently limits the use of FTB as a control effector is that it produces highly nonlinear and uncertain forces. In this work we develop a technique that will yield for the first time robust control at small levels of blowing thus enabling a new level of efficiency in the use of FTB as a device for flight control at high angles of attack.					
15. SUBJECT TERMS Nonlinear control, Vortex Control, High Angle-of-Attack					
16. SECURITY CLASSIFICATION OF:			17. LIMITATION OF ABSTRACT UU	18. NUMBER OF PAGES 108	19a. NAME OF RESPONSIBLE PERSON Stephen M. Rock
a. REPORT U	b. ABSTRACT U	c. THIS PAGE U			20b. TELEPHONE NUMBER (include area code) 650-723-3343

20010109 110

# **Nonlinear Control using Forebody Tangential Blowing**

AFOSR Grant No. F49620-96-1-0248

**Final Report**  
**June 1996 through December 1998**

submitted to the  
Air Force Office of Scientific Research

submitted by  
Stephen M. Rock, P.I.  
Yuji Takahara, Ph.D.

Department of Aeronautics and Astronautics  
Stanford University  
Stanford, CA 94305-4035

NONLINEAR FLIGHT CONTROL USING FOREBODY  
TANGENTIAL BLOWING

A DISSERTATION

SUBMITTED TO THE DEPARTMENT OF AERONAUTICS & ASTRONAUTICS  
AND THE COMMITTEE ON GRADUATE STUDIES

OF STANFORD UNIVERSITY

IN PARTIAL FULFILLMENT OF THE REQUIREMENTS

FOR THE DEGREE OF  
DOCTOR OF PHILOSOPHY

By

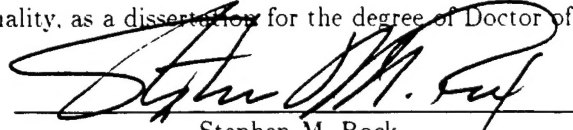
Yuji Takahara

June 1999


Copyright © 1999 by Yuji Takahara  
All Rights Reserved.



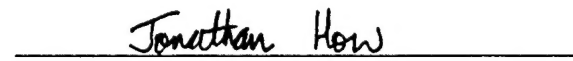
I certify that I have read this dissertation and that in my opinion it is fully adequate,  
in scope and quality, as a dissertation for the degree of Doctor of Philosophy.

  
Stephen M. Rock  
Department of Aeronautics and Astronautics  
(Principal Adviser)

I certify that I have read this dissertation and that in my opinion it is fully adequate,  
in scope and quality, as a dissertation for the degree of Doctor of Philosophy.

  
Brian J. Cantwell  
Department of Aeronautics and Astronautics

I certify that I have read this dissertation and that in my opinion it is fully adequate,  
in scope and quality, as a dissertation for the degree of Doctor of Philosophy

  
Jonathan P. How  
Department of Aeronautics and Astronautics

Approved for the University Committee on Graduate Studies:

\_\_\_\_\_

*To my wife, Yoshimi and my son, Keiichi (James)*

# Abstract

This dissertation is on the development and experimental demonstration of a new nonlinear approach to developing control laws for the lateral-directional dynamics of aircraft at high angles of attack using Forebody Tangential Blowing (FTB).

FTB is a pneumatic device that modifies the vortical flow over the forebody. The modified vortical flow in turn creates roll and yaw moments for control. FTB has been shown to be a very powerful means of generating forces and moments on aircraft operating in flight regimes where the effectiveness of conventional aerodynamic surfaces is reduced (e.g. post stall). Consequently, it provides a mechanism that could greatly expand the flight envelope of future aircraft systems. Further, it offers a means of generating forces and moments that could replace conventional surfaces in other regions of the operating envelop.

One major factor that currently limits the use of FTB is that it is a highly nonlinear and uncertain effector. In particular, FTB can provide very powerful effects (e.g. forces and moments) at low levels of blowing but the characteristic relating input to output is highly nonlinear in this region. On the other hand, if higher levels of blowing are used, the characteristics become well behaved. Hence, the trade-off between robustness and control usage is particularly acute.

The goal of this thesis is to develop a technique that will yield for the first time robust control at small levels of blowing thus enabling a new level of efficiency in the use of FTB as a device for flight control at high angles of attack.

The approach developed is based on combining High-Gain Control (HGC) and Lyapunov techniques. By employing a robust inversion of uncertain static nonlinearities, the new control law can be applied to a class of systems represented by a cascade connection of a nonlinear system and an uncertain linear system. In particular, the nonlinear control approach is applied to the control of an aircraft utilizing FTB and can fully exploit the FTB efficiency. Simulation and experimental results are provided that demonstrate the

effectiveness of the approach. Further, the design consists of a few simple steps and does not require a Lyapunov function for the entire system or upper bounds on the uncertainties.

# Acknowledgments

I would like to thank Prof. Stephen M. Rock, my advisor for his guidance and support throughout my PhD studies. In addition, I would like to thank Prof. Cantwell and Prof. How for their suggestions and insights, as well as their gracious service on my reading committee. Prof. Alonso and Prof. Tomlin provided both support and valuable insight as members of my Orals Committee, and Prof. Kailath kindly chaired it.

I would also like to thank the members of the FTB group. Dr. Nelson Pedreiro introduced me to the research in control of aircraft at high angles of attack using Forebody Tangential Blowing and helped me in many occasions during this work. Jonathan K. Chow provided me with insights into the aerodynamic phenomena. Fellow graduate students, Tom Pa e, Sungyung Lim, John Pye, Bruce Woodley, Carl Adams, Chad Jennings, Dana Clarke, Calving Wong and Chengyu Lee provided companionship, encouragement, as well as suggestions which helped to make my graduate studies a pleasant experience. I owed much to Aerospace Robotics Laboratory, in particular, Gad Shelf for his splendid mechanical designs and Godwin Zhang for his knowledge on electronic devices.

I wish to express my appreciation to the Technical Research and Development Institute, Japan Defense Agency that provided me with an opportunity to study at Stanford, and to the Air Force Office of Scientific Research that funded this research under Grant NO. F49620-96-0248.

Most of all, I am grateful for my family. My parents, Jun and Keiko Takahara for their support and my son, Keiichi for the joy and happiness he brings me. Lastly, I must thank you my wife, Yoshimi. Her love, patience, encouragement and sacrifice have transformed this stage of our lives into one of growth. I can never repay her for sustaining me through these years.

# Contents

<b>Abstract</b>	<b>v</b>
<b>Acknowledgments</b>	<b>vii</b>
<b>List of Tables</b>	<b>xi</b>
<b>List of Figures</b>	<b>xii</b>
<b>List of Symbols</b>	<b>xv</b>
<b>List of Acronyms</b>	<b>xviii</b>
<b>1 Introduction</b>	<b>1</b>
1.1 Background . . . . .	1
1.2 Control using FTB . . . . .	5
1.3 Previous Research . . . . .	6
1.4 Research Objectives . . . . .	9
1.5 Contributions . . . . .	9
1.6 Thesis Outline . . . . .	10
<b>2 Experimental Apparatus</b>	<b>12</b>
2.1 Wind Tunnel Facilities . . . . .	13
2.2 Model Support System . . . . .	13
2.3 Wind Tunnel Aircraft Model . . . . .	15
2.4 Air Injection System . . . . .	16
2.5 Flaperon System . . . . .	18
2.6 Data Acquisition and Real-time Control . . . . .	18

<b>3</b>	<b>Mathematical Model</b>	<b>20</b>
3.1	Rigid Body Dynamics . . . . .	21
3.2	Aerodynamic Model . . . . .	23
3.3	FTB characteristics . . . . .	24
3.3.1	Static characteristics . . . . .	24
3.3.2	Dynamic characteristics . . . . .	26
3.3.3	Summary . . . . .	26
3.4	Model Uncertainties . . . . .	40
3.5	Nominal Static Aerodynamic Moment . . . . .	42
3.6	FTB system . . . . .	43
3.7	Summary . . . . .	44
<b>4</b>	<b>Approach to Nonlinear Control</b>	<b>45</b>
4.1	Problem Statement . . . . .	46
4.1.1	System Description . . . . .	46
4.1.2	Assumptions . . . . .	47
4.2	Nonlinear Control Design . . . . .	48
4.2.1	Step 1: Virtual Control . . . . .	49
4.2.2	Step 2: Reduced Order Observer . . . . .	49
4.2.3	Step 3: High-Gain Lyapunov Control . . . . .	51
4.2.4	Discussion . . . . .	55
4.3	Proofs . . . . .	56
4.3.1	Boundedness of $\tilde{\eta}$ . . . . .	56
4.3.2	Boundedness of $s$ . . . . .	56
4.3.3	Boundedness of $x$ . . . . .	59
4.3.4	Boundedness of $\eta$ . . . . .	60
4.4	Summary . . . . .	60
<b>5</b>	<b>Control Results</b>	<b>62</b>
5.1	Application to the FTB system . . . . .	63
5.1.1	Control Objective . . . . .	63
5.1.2	System Description . . . . .	63
5.1.3	Virtual Control . . . . .	64
5.1.4	High-Gain Lyapunov Control . . . . .	64

5.2	1-DOF ( $\phi$ )	66
5.2.1	System Description	66
5.2.2	Set-point Tracking	67
5.2.3	Summary of 1-DOF cases	74
5.3	2-DOF ( $\phi$ and $\gamma$ )	74
5.3.1	Stabilization	74
5.3.2	Set-Point Tracking	81
5.3.3	Summary of 2-DOF cases	83
5.4	Summary	85
<b>6</b>	<b>Conclusions</b>	<b>86</b>
6.1	Summary	86
6.2	Conclusions and Contributions	87
6.3	Recommendations	88
<b>A</b>	<b>Model Properties</b>	<b>90</b>
A.1	Dimensions	90
A.2	Mass/Inertia Properties	91
A.3	Other Parameters	91
<b>B</b>	<b>Active Torque Cancellation</b>	<b>93</b>
B.1	Hardware	93
B.2	Inertia cancellation	93
B.2.1	Bandwidth of ATC	95
B.2.2	Selection of $\xi$	100
B.3	Gravity torque cancellation	103
	<b>Bibliography</b>	<b>104</b>



# List of Tables

2.1 Data Acquisition and Control Equipment . . . . .	19
5.1 Summary of 1-DOF simulation results . . . . .	70
5.2 Summary of 1-DOF experimental results . . . . .	72
A.1 Geometric characteristics of the wing tunnel model . . . . .	90
A.2 Mass/Inertia Properties of the wind tunnel model . . . . .	92
A.3 Other physical parameters . . . . .	92

# List of Figures

1.1	F/A-18 HARV	2
1.2	Movable strake	3
1.3	Flow visualization of FTB on forebody vortices	4
1.4	Roll moment v.s. $C_\mu, \phi$ ( $\gamma = 0^\circ, \delta_f = 0^\circ$ )	5
1.5	Control Plant structure	5
1.6	Control Structure in [1]	6
1.7	Control Structure in [34]	7
2.1	Top view of the wind tunnel	13
2.2	A schematic of the wind tunnel experimental apparatus	14
2.3	Wind tunnel model and detail of forebody slots	16
2.4	$C_\mu$ control system	17
2.5	Blowing servo step response	17
2.6	$\delta_f$ control system	18
2.7	Flaperon servo step response	19
3.1	Roll/"Yaw" moment v.s. $C_\mu, \phi$ ( $\gamma = 0^\circ, \delta_f = 0^\circ$ )	27
3.2	Roll/"Yaw" moment v.s. $C_\mu, \phi$ ( $\gamma = -10^\circ, \delta_f = 0^\circ$ )	28
3.3	Roll/"Yaw" moment v.s. $C_\mu, \phi$ ( $\gamma = 10^\circ, \delta_f = 0^\circ$ )	29
3.4	Roll/"Yaw" moment v.s. $C_\mu, \gamma$ ( $\phi = 0^\circ, \delta_f = 0^\circ$ )	30
3.5	Roll/"Yaw" moment v.s. $C_\mu, \gamma$ ( $\phi = -20^\circ, \delta_f = 0^\circ$ )	31
3.6	Roll/"Yaw" moment v.s. $C_\mu, \gamma$ ( $\phi = 20^\circ, \delta_f = 0^\circ$ )	32
3.7	Roll/"Yaw" moment v.s. $\phi, C_\mu$ ( $\gamma = 0^\circ, \delta_f = 0^\circ$ )	33
3.8	Roll/"Yaw" moment v.s. $\gamma, C_\mu$ ( $\phi = 0^\circ, \delta_f = 0^\circ$ )	34
3.9	Roll/"Yaw" moment v.s. $C_\mu, \delta_f$ ( $\phi = 0^\circ, \gamma = 0^\circ$ )	35
3.10	Roll/"Yaw" moment increment v.s. $\delta_f, \phi$ ( $\gamma = 0^\circ, C_\mu = 0$ )	36
3.11	Roll/"Yaw" moment increment v.s. $\delta_f, \gamma$ ( $\phi = 0^\circ, C_\mu = 0$ )	37

3.12	Roll/"Yaw" moment increment v.s. $\delta_f, C_\mu$ ( $\phi = 0^\circ, \gamma = 0^\circ$ ) . . . . .	38
3.13	Transient moment due to blowing . . . . .	39
3.14	Transient roll moment due to flaperon . . . . .	40
3.15	Uncertain Static Moment . . . . .	41
3.16	Block Diagram of FTB system structure . . . . .	43
4.1	Block Diagram of nonlinear system under consideration . . . . .	46
4.2	Block Diagram of Controller/Plant structure . . . . .	48
4.3	Virtual Closed Loop . . . . .	49
4.4	Inversion of nonlinearity (Determination of $u$ ) . . . . .	53
4.5	High-Gain Lyapunov Control . . . . .	55
4.6	Boundedness of $s$ . . . . .	57
5.1	Inversion of a nonlinear static moment (Determination of $C_\mu$ ) . . . . .	65
5.2	Block Diagram of the 1-DOF system ( $\phi$ ) . . . . .	67
5.3	Virtual control (1-DOF set-point tracking) . . . . .	68
5.4	1-DOF ( $\phi$ ) set-point tracking (Simulation), $\kappa = 5$ . . . . .	69
5.5	1-DOF ( $\phi$ ) set-point tracking (Simulation), $\kappa = 50$ . . . . .	70
5.6	1-DOF ( $\phi$ ) set-point tracking (Simulation), $\kappa = 500$ (Bang-Bang) . . . . .	71
5.7	1-DOF ( $\phi$ ) set-point tracking (Experiment), $\kappa = 50$ . . . . .	72
5.8	1-DOF ( $\phi$ ) set-point tracking (Experiment), $\kappa = 500$ (Bang-Bang) . . . . .	73
5.9	Open-loop response (2-DOF) . . . . .	75
5.10	Virtual control (2-DOF stabilization) . . . . .	78
5.11	2-DOF Stabilization (Simulation, bias error) . . . . .	79
5.12	2-DOF Stabilization (Simulation, periodic disturbance) . . . . .	80
5.13	Virtual control (2-DOF set-point tracking) . . . . .	82
5.14	2-DOF set-point tracking (Experiment), $\kappa = [40 \ 140]$ . . . . .	83
5.15	2-DOF set-point tracking (Experiment), $\kappa = [400 \ 1400]$ (Bang-Bang) . . . . .	84
A.1	Wind tunnel model - 3 view . . . . .	91
B.1	Hardware of Active Torque Cancellation . . . . .	94
B.2	Block Diagram of Active Cancellation . . . . .	94
B.3	Torque Command . . . . .	95
B.4	Normalized step response of $\ddot{\gamma}$ . . . . .	97
B.5	"yaw" moment v.s. $C_\mu, \gamma$ ( $\phi = 0^\circ, \delta_f = 0^\circ$ ) . . . . .	98
B.6	Filtered $\ddot{\gamma}$ . . . . .	99

B.7	Power spectrum of $\ddot{\gamma}$ signal . . . . .	100
B.8	Open-loop Bode plot of the torque characteristic . . . . .	101
B.9	Block Diagram of Torque Control . . . . .	101
B.10	Step response of torque control . . . . .	102
B.11	Gravity torque . . . . .	103

# List of Symbols

$A_i$	Linearized system matrix (rigid body)
$B_i$	Linearized input matrix (rigid body)
$C_f$	Friction coefficient matrix
$C(q, \dot{q})$	Generalized damping matrix
$C_l$	Roll moment coefficient
$C_n$	Yaw moment coefficient
$C_\mu$	Jet moment coefficient
$c_{fi}$	Friction coefficient
$c_i, c'$	Positive scalar constant ( $i = 1, \dots, 4$ )
$c_{gi}$	Positive scalar constant ( $i = 1, 2$ )
$c_s$	Upper bound of $s$
$F_a$	System matrix (aerodynamic system)
$\delta F_a$	System matrix (uncertain part)
$F_r$	System matrix Rigid body (1 – DOF)
$f(x)$	Nonlinear system function (rigid body)
$G_a$	Input matrix (aerodynamic system)
$\delta G_a$	Input matrix (uncertain part)
$G_r$	Input matrix Rigid body (1 – DOF)
$g(x)$	Nonlinear input function (rigid body)
$H_a$	Output matrix (aerodynamic system)
$H(q)$	Generalized inertia matrix
$I$	Identity Matrix

$I_A$	Moment of inertia of apparatus
$I_x, I_y, I_z$	Moment of inertia of model $x, y, z - axis$
$I_{xz}$	Product of inertia of model $y - axis$
$K_d$	Derivative gain matrix
$K_i$	Integral gain matrix
$K_p$	Proportional gain matrix
$K_s$	Positive definite High – Gain matrix
$k(x)$	Virtual control for rigid Body
$k_{\delta_f}$	flaperon effectiveness coefficient
$k_g$	gravity torque coefficient
$m$	Aerodynamic moment
$m_f$	Friction moment
$m_g$	Gravity torque
$m_m$	Motor torque
$m_s$	static aerodynamic moment
$\overline{m}_s$	nominal static aerodynamic moment
$\delta m_s$	unknown static aerodynamic moment
$m_T$	Total moment
$m_v$	Virtual moment = $k(x)$
$\dot{m}_j$	mass flow rate through the slot
$N$	Number of linearized systems (rigid body)
$n_u$	Dimension of $u$
$n_x$	Dimension of $x$
$n_\eta$	Dimension of $\eta$
$P_s$	Positive definite Lyapunov matrix for $s$
$Q_x$	Positive definite Lyapunov matrix for $x$
$q$	Generalized coordinates = $[\phi \ \gamma]^T$
$q_\infty$	freestream dynamic pressure
$S_{ref}$	reference area, wing planform area
$s$	manifold = $m - k(x)$
$u$	input = $[C_\mu \ \delta_f]^T$

$V$	Lyapunov function
$V_s$	Lyapunov function for $s$
$V_x$	Lyapunov function for $x$
$V_j$	jet exit velocity
$V_\infty$	Wind tunnel speed
$w$	Lumped uncertainty
$\dot{x}$	Rigid body state = $[\phi \ \gamma \ \dot{\phi} \ \dot{\gamma}]^T$
$x_e$	Augmented rigid body state
$y$	Output = $[x^T \ m^T]^T$
$\alpha_s$	Decay rate of $s$
$\alpha_x$	Decay rate of $x$
$\beta$	Condition number
$\gamma$	“yaw” angle
$\delta_f$	flaperon deflection
$\eta$	Aerodynamic states
$\hat{\eta}$	Estimate of aerodynamic states
$\tilde{\eta}$	Estimation error = $\eta - \hat{\eta}$
$\kappa$	High – Gain parameter
$\tilde{\kappa}$	Modified High – Gain parameter
$\lambda$	Eigenvalue
$\mu$	Upper bound of normalized input
$\nu$	Inertia ratio = $I_A/I_z$
$\rho$	Upper bound of uncertainties
$\tilde{\rho}$	Modified upper bound of uncertainties
$\tau_i$	Time constant, aerodynamic lag ( $i = 1, 2$ )
$\tau_c$	Time constant, Active Torque cancellation
$\phi$	Roll angle
$\xi$	Inertia ratio uncanceled

# List of Acronyms

ATC	Active Torque Cancellation
BW	Band Width
CM	Center of Mass
DOF	Degree of Freedom
FTB	Forebody Tangential Blowing
HGC	HIGH-Gain Control
LMI	Linear Matrix Inequality
LTI	Linear Time-Invariant
LPF	Low Pass Filter



# Chapter 1

## Introduction

### 1.1 Background

Flying capability at high angles of attack is beneficial to both military and commercial aircraft. For a modern fighter aircraft, the enhancement of maneuverability is increasingly important. During an initial contact, the ability to turn quickly or point and shoot provides greatly improved survivability in hostile environment. For a commercial aircraft such as the planned High-Speed Civil Transport, an increase in lift at high angle of attack could yield a short take-off and landing capability and hence a reduction in airport noise.

However, flow separation, vortex shedding and possibly vortex breakdown at high angles of attack decrease the efficiency of conventional control surfaces at a time when they are most needed due to the onset of destabilizing asymmetric flow. As a result of the inefficiency of the conventional control surfaces, an alternate means for generating control power is required to augment the flight control. Figure 1.1 shows separated flow around F/A-18 HARV (High-Alpha Research Vehicle) flying at  $20^\circ$  angle of attack. Because the vortex shed from the strake breaks down in front of the vertical tails, the effectiveness of the rudders is greatly reduced.

Creation of aerodynamic loads/moments through displacement of forebody vortices is a promising way of providing additional control power with minimal modification to an aircraft. Extensive work has been done to investigate the effect of forebody fineness ratio, shape, and bluntness and flow tripping stripes on the onset of side forces loads, see for example [28]. Also using a rotating forebody tip has been shown to alleviate side forces on a slender body at high angles of attack [48].

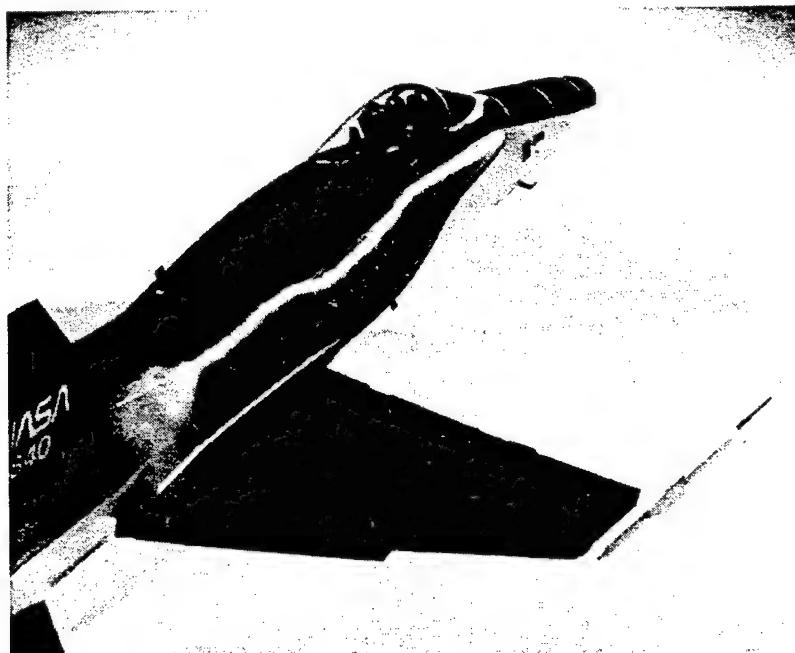


Figure 1.1: F/A-18 HARV

The potential of actively altering the flow to control an aircraft has also been investigated. Several actuation methods such as deployable forebody strakes, rotating miniature nose-tip strake, and forebody blowing have been applied.

Deployable forebody strakes have shown the capability of controlling side forces and yaw moment. Figure 1.2 shows a movable forebody strake. NASA/Langley wind tunnel tests [39] indicate that the stability of an F/A-18 could be improved by the use of forebody strakes. Ng Terry and Malcom [32] investigated the use of a rotating miniature nose-tip strake. The system was effective in generating controllable yaw moment and is mechanically simpler than the deployable strakes.

The use of pneumatic flow control on aircraft flying at high angle of attack has been a topic of aerodynamic research over the past several years [22, 40, 47, 20, 13, 12, 46, 30], since it can be as effective as movable strakes and potentially mechanically simpler and smaller than movable strakes. Wong [30] experimentally demonstrated the use of injecting a thin jet of air tangentially to the rounded leading-edge of a wing to control the roll oscillation of a delta wing at 55 degrees angle of attack. Skow [41] investigated the concept of forebody vortex blowing as a means to alter the symmetric vortices on the leeside of an aircraft forebody. Nozzles located at the leeside of the forebody were used to inject a jet of air



**Figure 1.2:** Movable strake

directed to the rear of the vehicle. In the work of Skow, experimental results showed that the method could generate significant yaw moments for angles of attack between 22 and 55 degrees and simulations indicated that departure/spin recovery characteristics could be improved.

Another pneumatic technique is the concept of Forebody Tangential Blowing (FTB) [7,6,4,5]. It is one of the most studied and promising ways of altering the flow over the forebody and is the method used in this study. In this technique, a thin sheet of air is injected tangent to the forebody of an aircraft. The injected air moves the separation lines on the forebody and changes the amount of vorticity that is shed. As a consequence, the strength and positions of the vorticities are affected by blowing [36,22]. For example, Figure 1.3 [9] represents a flow visualization result that shows the basic structure of the flow. The effect of blowing is mainly to increase or decrease the asymmetry, depending on which side

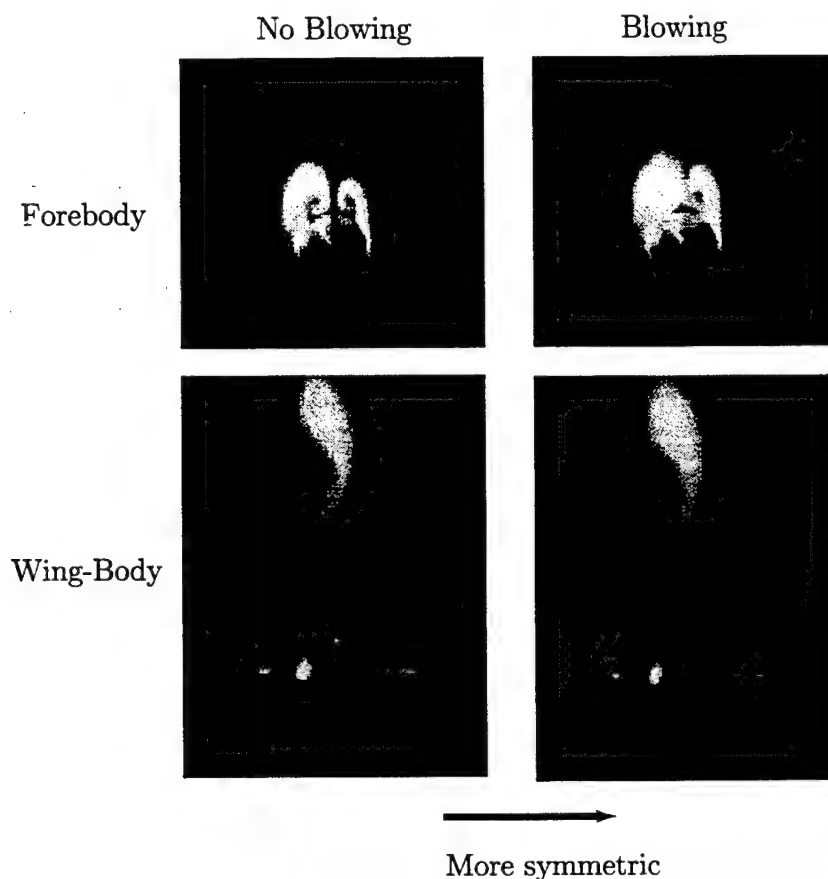


**Figure 1.3:** Flow visualization of FTB on forebody vortices

the blowing is applied from. In the figure, a small amount of blowing at the forebody is applied to decrease the asymmetry. The blowing makes the two vortex strengths over the wing-body position more symmetric. This leads to a smaller roll moment. A similar effect can be achieved in the yaw direction.

One major factor that currently limits the use of FTB is that it is a highly nonlinear and uncertain effector. The forces and moments it produces on an aircraft are complex functions of the actuating air supply, and also depend on the aircraft state. Figure 1.4 shows one example. In the figure, the horizontal axis represents the amount of blowing and the vertical axis is the nondimensional coefficient of roll moment. The various curves correspond to the various roll angles. (Details of this plot are discussed in Chapter 3.) From the plot, it is observed that blowing characteristics are not only highly nonlinear in the amount of blowing but also are dependent on the aircraft state (roll angle in this case).

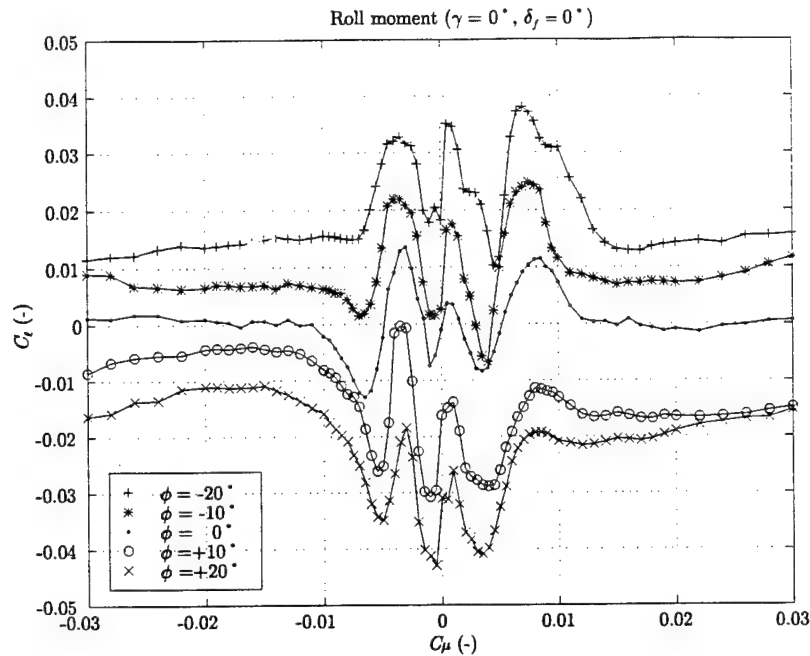


Figure 1.4: Roll moment v.s.  $C_\mu, \phi$  ( $\gamma = 0^\circ, \delta_f = 0^\circ$ )

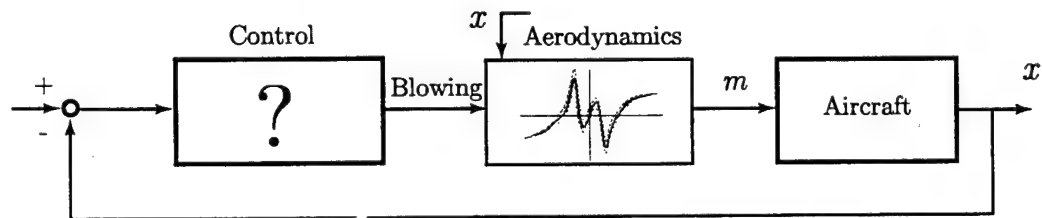


Figure 1.5: Control Plant structure

Further, FTB differs from conventional devices in that it is not represented well as an incremental control device. That is, the aircraft stability derivatives depend on the level of blowing. Furthermore, the nonlinear properties have many uncertain factors due to the highly nonlinear nature of the device.

## 1.2 Control using FTB

The generic problem of using FTB to control an aircraft is presented in Figure 1.5. It shows a blowing characteristic (represented by the fuzzy nonlinear curve). (See Figure 1.4 for real data.) In this figure,  $m$  represents the forces and moments that act on the aircraft

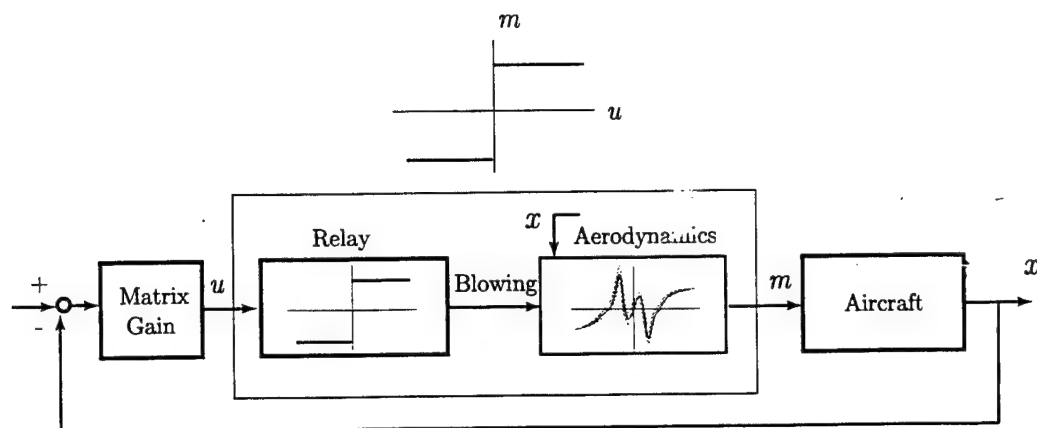


Figure 1.6: Control Structure in [1]

due to blowing. The three standard issues associated with all control designs are of course applicable to this system: The control must provide adequate performance, be sufficiently robust, and must minimize the amount of control power consumed. The factor that makes addressing these issues particularly challenging in this application is that the control device in question is highly nonlinear and uncertain where it is most efficient. That is, FTB provides very powerful effects (e.g. forces and moments) at low levels of blowing but the characteristic relating input to output is very nonlinear in this region. On the other hand, if higher levels of blowing are used, then the characteristics become well behaved but the control authority decreases and the control effort increases. Hence, the trade between robustness and control usage is particularly acute (Figure 1.4). In order to exploit the high efficiency possible with FTB, a new approach must be developed. The ultimate goal of this work, therefore, is to develop a new generic approach to nonlinear control that can robustly exploit the efficiency of powerful but highly nonlinear and uncertain systems. The new approach will be able to robustly use the small levels of blowing in the regime where FTB is most efficient but the characteristic is highly nonlinear and uncertain. With such an approach, FTB can be a very efficient device for flight control at high angles of attack.

### 1.3 Previous Research

Previous studies have shown that control laws using FTB can be developed using conventional nonlinear control approaches [1, 35].

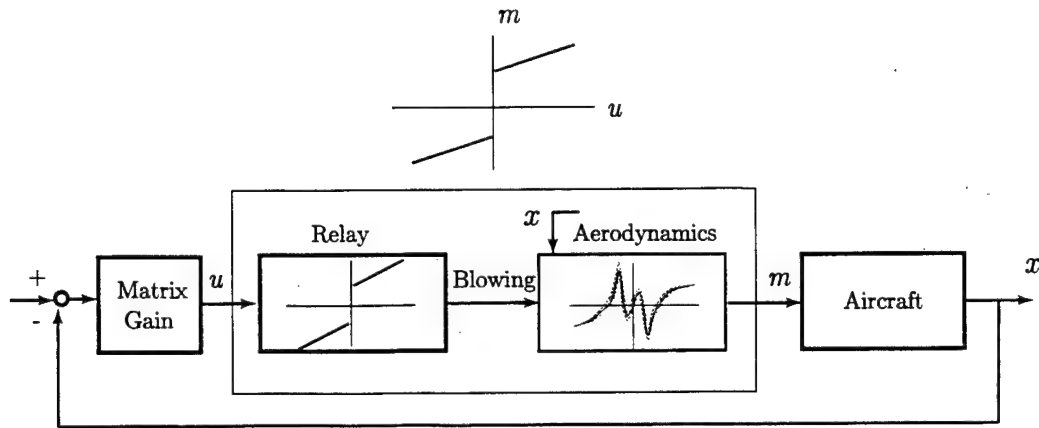


Figure 1.7: Control Structure in [34]

Adams *et al.* [1] used experimental data on the effects of forebody blowing to augment the yaw control of a modified VISTA F-16 aircraft in simulation. Assumptions were made that blowing provided additional control and that vehicle characteristics were not affected by blowing. They used Bang-Bang control to achieve a sliding mode and the Bang-Bang control used a fixed amount of blowing air. This control scheme is depicted in Figure 1.6. By using the fixed amount of air that is outside of the highly nonlinear region, the highly nonlinear characteristics of FTB were effectively replaced with a known relay nonlinearity (Figure 1.6). Simulation results showed that significant improvement in high angle of attack performance could be achieved using this technique. Further, they analyzed the closed-loop system using describing function and  $\mu$  techniques and showed that the closed-loop system was robust. The amount of air used in the Bang-Bang control was chosen so that the highly nonlinear but efficient characteristics of FTB at small levels of blowing were avoided. Consequently, the potential efficiency of using FTB at small levels of blowing was not explored.

In a separate study, Pedreiro [34] developed a dynamic FTB aerodynamic model. Based on the model, he simplified an FTB system as a connection of a linear system and a known nonlinearity (relay-type) by using a fixed minimum amount of air. Figure 1.7 shows the control structure he used. He demonstrated the effectiveness of this approach in wind tunnel experiments using a unique apparatus. Since a fixed minimum amount of air was also chosen large enough to avoid highly nonlinear but powerful characteristics, the high efficiency of FTB was not explored fully in this work either.

As mentioned above, in order to exploit the full efficiency possible with FTB, a controller must operate at low levels of blowing where the actuation effects are highly nonlinear. This objective could be achieved with a control law that could invert the nonlinear characteristics. However, the inversion of these highly nonlinear effect which involve a high degree of uncertainty can lead to a very sensitive, and possibly even unstable, closed loop system. Any such inversion technique must be robust and explicitly take into account the associated uncertainties. Only in this way can satisfactory performance be guaranteed.

Several nonlinear control techniques for robustification for highly nonlinear system with significant uncertainties (such as the FTB system) have been proposed. Reviews of these techniques are available in the literature, for example, [10, 43]. None of these existing techniques is directly applicable to robustifying the inversion of highly nonlinear uncertain characteristics encountered in FTB, however, because the upper bounds of uncertainties and/or a full dimensional Lyapunov function are required in their basic forms. Tight upper bounds of uncertainties are difficult to achieve for the FTB system. Also, it can be extremely difficult to find a full dimensional Lyapunov function. Even if it is found, using it could be a problem for the real-time implementation because of the added complexity with higher dimensionality. Brief descriptions of some of these techniques are given below:

Sliding Mode Control [16, 45, 24, 23, 19, 44] is a powerful technique for dealing with matched uncertainties [27]. It only needs a low dimensional Lyapunov function. However, it requires the information on the upper bounds of uncertainties in the system. This information is not precisely known in most systems (including the FTB system). Usually, over-estimated values are used to guarantee the stability of the system, because under-estimated bounds can lead to instability of the closed-loop system. Also, discontinuous control results from sliding mode control. Some measures such as boundary layer need to be taken to avoid chattering due to discontinuity.

Lyapunov Redesign [21, 11] is another effective way of handling uncertainties when the upper bounds of uncertainties are known, uncertainties are matched and a full dimensional Lyapunov function for the nominal system is available. The necessity of the upper bounds of uncertainties is again problematic. This technique also generates discontinuous control. Furthermore, the requirement of a full dimensional Lyapunov function for the nominal system limits the usefulness of this technique.

High-Gain Control [49, 31, 45] is a classical tool for reduction of the effects of uncertain factors such as disturbances, parameter variations, and distortions. In its basic form, the



technique is effective when uncertainties are matched. Also, High-Gain control requires that systems be transformable to a singular perturbation form. Transforming the FTB system into the form requires an artificial introduction of singular parameters, which are difficult to identify.

Dynamic Nonlinear Damping [26,27,29] is a promising technique for generating a control law when the information on the upper bounds of uncertainties is unknown but uncertainties are matched. In its basic form, however, a full dimensional Lyapunov function for the nominal system is required. The advantage of not requiring the information on the upper bounds is blended into the control approach proposed in this dissertation. (See Section 4.3.2.)

In summary, none of these existing techniques is directly applicable to the problem of FTB control.

## 1.4 Research Objectives

The primary objective of this research is to develop a new generic approach to nonlinear control that can robustly invert highly nonlinear and uncertain characteristics without requiring the upper bounds of uncertainties and a full dimensional Lyapunov function.

The secondary objective is to validate experimentally this new approach in the control of an FTB system and hence demonstrate the efficiency possible with FTB while providing sufficient robustness.

## 1.5 Contributions

In pursuit of achieving the objectives stated above, the research reported in this dissertation has resulted in the following contributions.

- A new nonlinear control approach is developed that robustly controls a class of uncertain nonlinear systems. This approach is generically applicable to a class of nonlinear systems represented by a cascade connection of a nonlinear dynamical system and an uncertain linear dynamical system. It robustly inverts uncertain static nonlinearities and consists of a few simple steps that allow time-scale separation of each step. Neither upper bounds on the uncertainties nor a full dimensional Lyapunov function is required. It allows explicit trade-off between the performance and the control efforts

- This approach is applied to the problem of FTB. It is shown to enable FTB to operate efficiently in a sense that it can operate in small levels of blowing where it is most efficient but highly nonlinear and uncertain.
- The approach is demonstrated experimentally to achieve independent set-point tracking control of 2-DOF system (roll and “yaw” angles) with FTB and flaperons at high angle of attack. The results demonstrate reduction in air usage to about 1/3 of that achieved with conventional Bang-Bang control while the bound of the controlled output is only doubled.

## 1.6 Thesis Outline

The experimental apparatus used in this thesis is introduced in Chapter 2. The characteristics of the wind tunnel, wind tunnel aircraft model, model support system, air injection system, flaperon system and data acquisition and real-time control are presented.

In Chapter 3, a mathematical model of the FTB system described in Chapter 2 is developed. This model consists of the rigid body dynamics and the aerodynamic model. FTB characteristics are presented in this chapter. Also included are descriptions of the model uncertainties and the simplifications of the static aerodynamic characteristics.

The details of the control design approach are described in Chapter 4. A class of systems represented by a cascade connection of a nonlinear dynamical system and an uncertain linear dynamical system is introduced. The main control design approach which consists of three steps (virtual control design, reduced order observer design and High-Gain Lyapunov control design) is described in detail. The proofs of stability are also given.

In Chapter 5, the nonlinear control design is applied to the FTB system in three configurations: one Degree of Freedom (1-DOF) roll tracking, 2-DOF (roll and “yaw”) stabilization with blowing only and 2-DOF tracking with blowing and flaperons. Each step of the control design for these three configurations is explained in detail. Simulation and experimental results are presented.

Chapter 6 presents the summary of this thesis, the conclusion and the contributions. The recommendations for future studies are also presented.

Appendix A contains information on the detailed geometry and mass/inertia properties of the the wind tunnel aircraft model used in the research.

Appendix B discusses an active torque cancellation (ATC) technique employed in the experiments. ATC eliminates the effect of the gravity torque and reduces the effect of the large moment of inertia of the model supporting system so that the motion of the wind tunnel aircraft model is dominated by aerodynamic loads.

## Chapter 2

# Experimental Apparatus

This chapter describes in detail the experimental apparatus which was used for FTB experiments.

The system consists of a tailless, delta wing model that is constrained to move in two degrees of freedom inside a small wind tunnel located at Stanford University. This model has both an FTB system and movable flaperons as control effectors. This system was originally developed by Pedreiro [33]. With the flaperons added during this research, this system provides both the motivation for and the means to validate experimentally the nonlinear control approach developed in Chapter 4.

This chapter begins with the main characteristics of the wind tunnel facilities followed by a description of a unique model support system with two degrees-of-freedom which approximates the lateral-directional motion of the aircraft. Then, a wind tunnel aircraft model which has FTB capability as well as movable flaperons is introduced. Regarding the model, the air injection system and measurement of the amount of blowing air in terms of non-dimensional coefficient are described. Also described are the servo control of the injected flow and the servo control of two movable flaperons. Lastly, detailed information on the computer hardware and software used in data acquisition and real-time control is presented.

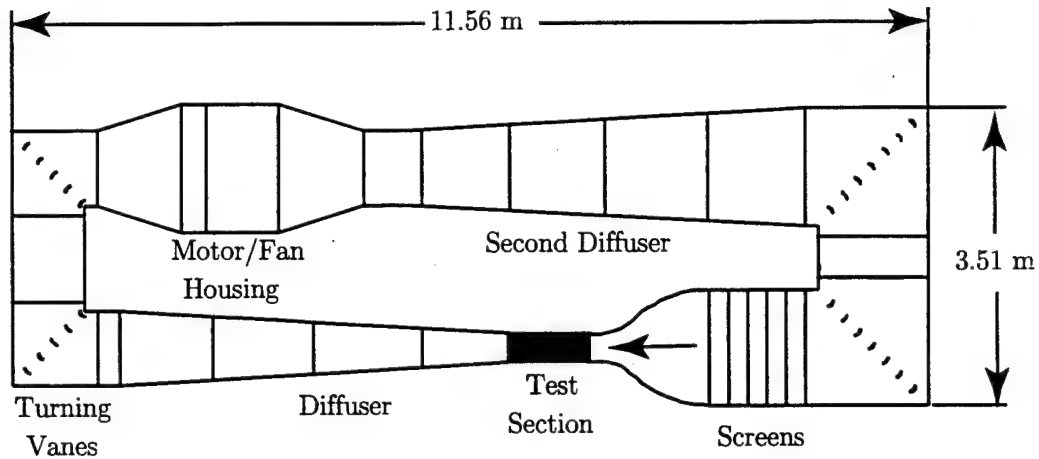


Figure 2.1: Top view of the wind tunnel

## 2.1 Wind Tunnel Facilities

The wind tunnel facility of the Aeronautics and Astronautics Department at Stanford University was used for the experiments conducted in this research. It consists of a closed circuit low speed wind tunnel. The top view of the wind tunnel is shown in Figure 2.1. The maximum free stream centerline speed at the test section is 60 m/s. The air speed can be closed-loop controlled by a variable speed motor to which a variable pitch fan is attached, and the temperature is also controlled by an air conditioner [38]. Screens are located upstream of the test section which reduce the main turbulence level at the test section to approximately 0.1 %. For the experiments conducted in this research, a nominal free stream speed of 24.5 m/s was used.

Test section dimensions are:  $0.45\text{m} \times 0.45\text{m} \times 0.91\text{m}$ , width, height and length respectively. It consists of a welded cast-iron frame. The bottom wall is made of sheet metal and top and side walls are made of plexiglas. The entire section is mounted on cast-iron castors so that it can be attached or removed from the rest of the wind tunnel. When in place, the test section is bolted to the exit of the tunnel contraction section.

## 2.2 Model Support System

The 2-DOF experimental wind tunnel apparatus being used in this investigation is shown schematically in Figure 2.2. A unique support system is used that constrains the model to

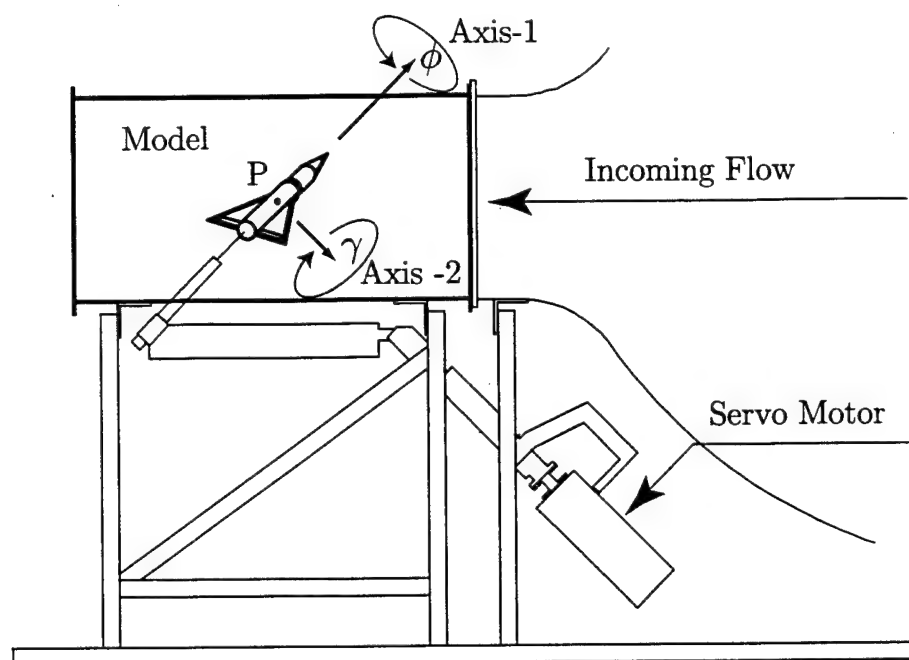


**Figure 2.2:** A schematic of the wind tunnel experimental apparatus

2-DOF [33]. The objective is to approximate the lateral-directional dynamics of an aircraft. Of particular interest is the roll-yaw coupling at high angles of attack. The support system can be divided into two main sub-systems. The first implements the roll degree-of-freedom, (roll:  $\phi$ ). The entire roll sub-system is mounted on the second sub-system which consists of a mechanical arm that can rotate about an axis perpendicular to the longitudinal axis of the model. This sub-system provides the second degree-of-freedom, ("yaw":  $\gamma$ ). The following sign conventions are used: Roll angle ( $\phi$ ) is positive for the model starboard wing down and "yaw" angle ( $\gamma$ ) is positive when the forebody moves in the starboard direction while the rear of the model moves to the port-side. The mechanical constraints limit the degrees-of-freedom to the following ranges:  $|\phi| < 105^\circ$  and  $|\gamma| < 30^\circ$ , and it is possible to change the nominal incidence angle,  $\alpha_0$ , in the range from 37 to 55 degrees. In the experiments conducted in this research,  $\alpha_0$  is fixed at 45 degree. This incidence is chosen because it is the worst angle in a sense that control authority from FTB is minimum [34]. For details of the support system, refer to [33].

Low friction precision potentiometers<sup>1</sup> are used to measure  $\phi$  and  $\gamma$ . An angular accelerometer<sup>2</sup> is used to measure angular acceleration of  $\phi$ . Two linear accelerometers<sup>3</sup> are used to measure angular acceleration of  $\gamma$ .

Point P is defined as a point on the body through which "yaw" motion occurs. All the inertia properties and moments<sup>3</sup> are about this point unless noted otherwise. Point P is about 0.8 in behind from the center of mass (CM) of the model. Inertia properties about CM is also given in Appendix A.

The servo motor<sup>4</sup> attached to the yaw shaft provides torque for the active torque cancellation that eliminates the effect of the gravity torque and reduces the effect of the large moment of inertia of the apparatus so that the motion of the aircraft model is dominated by aerodynamic loads. The active torque cancellation is explained in detail in Appendix B.

## 2.3 Wind Tunnel Aircraft Model

The aircraft model used in this research consists of a sharp leading-edge delta wing with 70 degrees sweep angle and a cone-cylinder fuselage. The length is about 11 inches and the wing span is 5.8 inches. Details of the model are described in Appendix A.

Blowing slots exist along both sides of the model's forebody through which air can be injected tangent to the body surface (Figure 2.3). Air is provided to the forebody plenum through flexible tubing that enters the model through the rear end of the fuselage. In this research, air is blown through only one slot at a time because the focus is on minimization of air usage. The sign convention for the blowing is that the right (starboard) side blowing is defined as positive blowing and the left (port) side as negative.

Movable flaperons are attached to the trailing edges. They can move up to  $\pm 45$  degrees. The flaperons constitute 20 % of the main wing area. Refer to [37] for details about the sizing of the flaperons. Two motors<sup>5</sup> each with a built-in encoder<sup>6</sup> are placed inside of the

---

<sup>1</sup>Precision potentiometer MKV-F78S, Conductive plastic REISITOFILM, New England Instrument Company, Woonsocket, RI 02895-1129

<sup>2</sup>SR-220RNP, Columbia Research Labs, Inc., 1925 Macdade Blvd., Woodlyn, PA 19094

<sup>3</sup>Systron Donner 4310A-1-P116 Linear Servo Accelerometer, Systron Donner Company, Inertial Division, Concord, CA 94518

<sup>4</sup>Electro-Craft Brushless Servo System, DM-30 Drive, S-4075-R-H00AA Motor, Reliance Motion Control Inc., Eden Prairie, MN 55344

<sup>5</sup>DC MicroMotors Series 1624 012s, Micro Mo Electronics Inc., 742 Second Avenue S. St. Petersburg, Florida 33701

<sup>6</sup>Magnetic Encoder Series HE 16PPR, Micro Mo Electronics Inc.

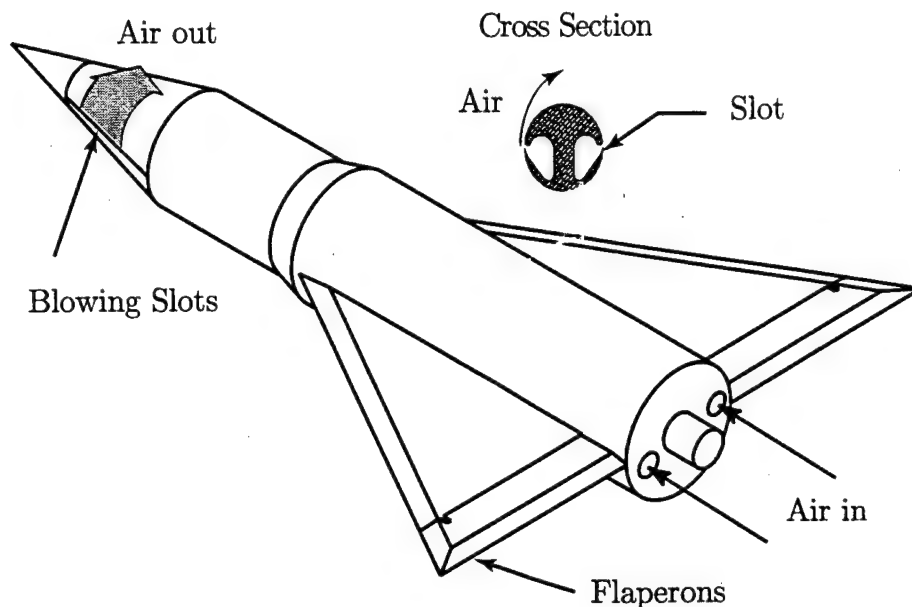


**Figure 2.3:** Wind tunnel model and detail of forebody slots

rear body. They drive the flaperons through gears and can be controlled independently. In this research, however, they are used in opposition, *i.e.*, they are always deflected by the same amount in the opposite direction. The sign conventions used here are that when the flaperons generate positive roll moment, the deflection is considered positive, *i.e.*, the right (starboard) side up and the left (port) side down.

## 2.4 Air Injection System

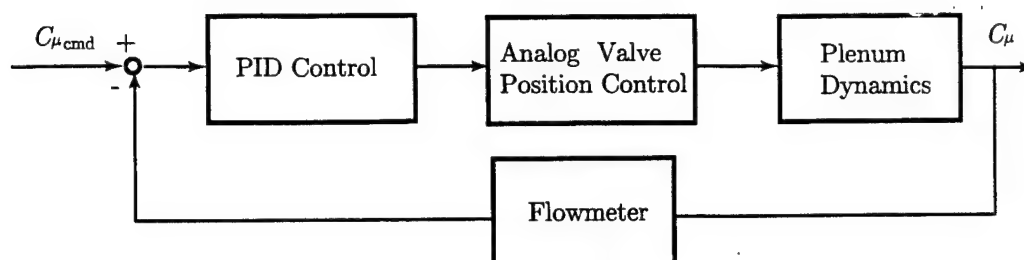
The amount of air injected through the slots was quantified by the jet moment coefficient,  $C_\mu$ , defined as

$$C_\mu = \frac{\dot{m}_j V_j}{q_\infty S_{ref}},$$

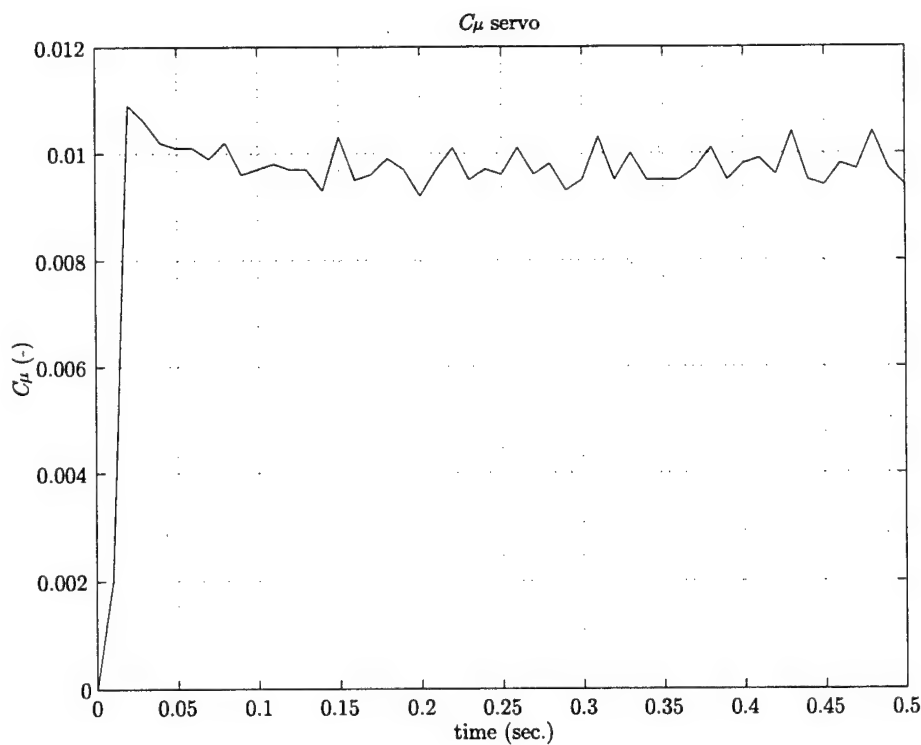
where

- $\dot{m}_j$  mass flow rate through the slot
- $V_j$  jet exit velocity
- $q_\infty$  free stream dynamic pressure
- $S_{ref}$  reference area, wing planform area



**Figure 2.4:**  $C_\mu$  control system

Specially designed flowmeters were used to measure the mass flow rate from which the jet momentum coefficient was calculated. They are located outside the test section and connected to the exit of the servo-valves which control the air flow rate and tubing which

**Figure 2.5:** Blowing servo step response

bring air to the model. For details of the measurement of jet moment coefficient using the flowmeter, refer to [33].

A closed-loop control system was used to control the amount of air that was injected through each slot on the model. Figure 2.4 shows the block diagram for the closed-loop control of  $C_\mu$ . For details about the analog valve control, refer to [30]. The block diagram for the closed-loop control of  $C_\mu$  is basically the same as the one in [34] except that the feedforward term is removed here because it was found to produce a noisy command signal to the valve position control.

The performance of the  $C_\mu$  closed-loop control is shown in Figure 2.5 in terms of the response to a step command. The rise time is about 0.02 seconds, which corresponds to about 100 rad/s bandwidth.

## 2.5 Flaperon System

Figure 2.6 shows the block diagram for the closed-loop control of flaperons. The performance of the flaperon control system is shown in Figure 2.7.  $\delta_f$  represents the flaperon deflection. The rise time is about 0.05 seconds, which corresponds to about 20 rad/s bandwidth.

## 2.6 Data Acquisition and Real-time Control

Stand alone personal computers equipped with plug-in data acquisition boards are used to acquire experimental data as well as to control the FTB system. A summary of the computer systems and software used is included in Table 2.1.

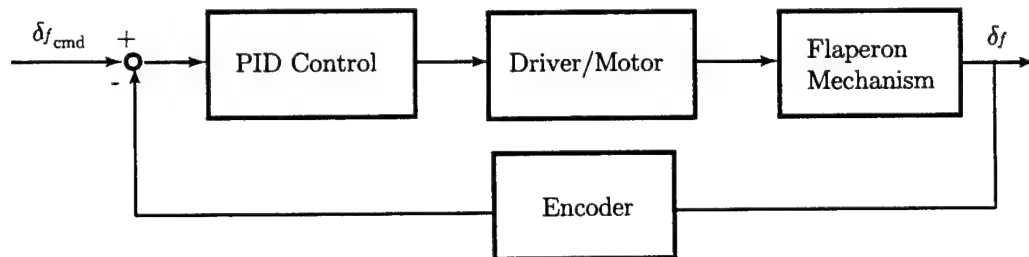


Figure 2.6:  $\delta_f$  control system

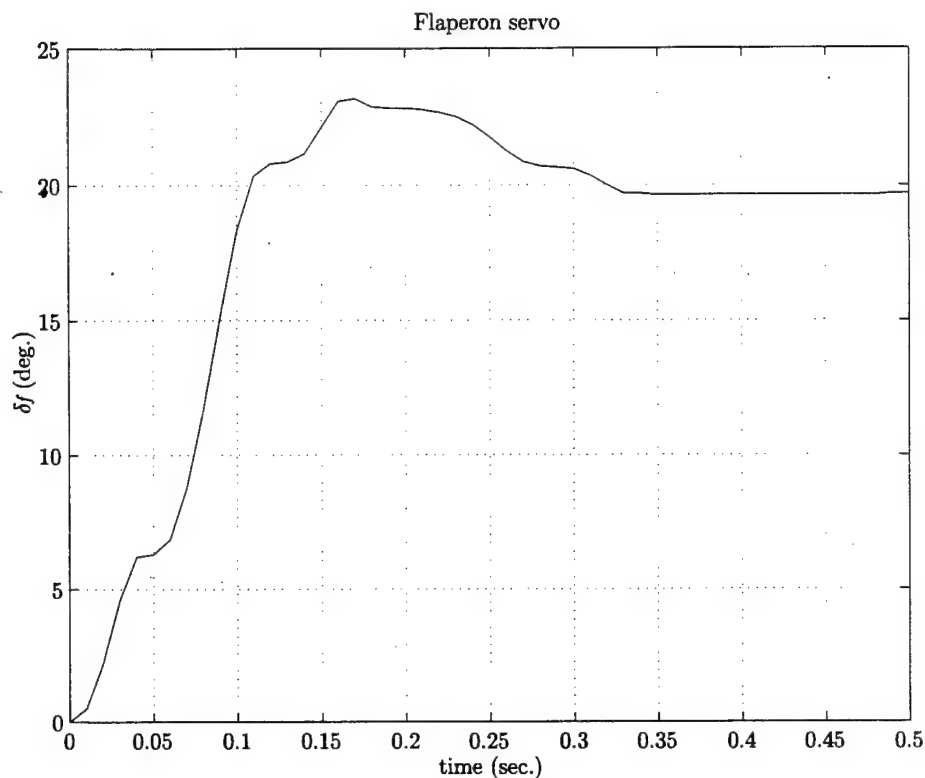


Figure 2.7: Flaperon servo step response

Computer System	Analog Digital I/O Card	Programming Language	Program Callable Subroutine	Tasks Description
Dell XPS Pentium II 300MHz	AT-MIO-16DE-10 <sup>1</sup> AT-AO-6 <sup>1</sup>	Borland C++ 5.02 <sup>2</sup>	NI-DAQ 6.0 <sup>3</sup>  Windows NT 4	Real Time Control Data Acquisition Static/Dynamic
Dell 310 80387 20MHz	DT2821-F-16SE <sup>4</sup>	Turbo C++ 3.0 <sup>5</sup>	287Lab <sup>6</sup> MS-DOS 6.22	Active Torque Cancellation

<sup>1</sup> National Instruments, 11500 N MOPAC Expway Austin, TX 78759-3504<sup>2</sup> C/C++ compiler for Win16/32 by Inprise Corporation, 100 Enterprise Way Scotts Valley, CA 95066<sup>3</sup> I/O subroutines by National Instruments<sup>4</sup> Data Translation, Inc., 100 Locke Drive Marlboro, MA 01752-1192<sup>5</sup> C/C++ compiler for DOS by Inprise Corporation<sup>6</sup> Assembly Language C callable real-time I/O subroutines written by Marc Ullman

Table 2.1: Data Acquisition and Control Equipment

## Chapter 3

# Mathematical Model

A mathematical model of the FTB system described in Chapter 2 is developed in this chapter. The key element of the FTB system model is the aerodynamics. Aerodynamics at high angles of attack is very complicated due to separated flow, vortex shedding and possibly vortex breakdown. In this research, the model of aerodynamic effects is based on the work by Pedreiro [34] in which it was shown that the aerodynamic moments can be well modelled using lagged static loads. This approach is not only simple enough for the use of control design but also captures the important aspects of aerodynamics.

This chapter begins with a discussion of the rigid body dynamics of the FTB system. The dynamics of the rigid body are expressed in terms of generalized coordinates ( $\phi$  and  $\gamma$ ) through Euler-Lagrange equations. This is followed by a discussion of the aerodynamics. The aerodynamics are modeled as lagged static moments, which are highly nonlinear functions of the amount of blowing. Data are presented which show that the effects of the attitude on the static moments are well behaved, the effectiveness of flaperons in generating roll moment can be approximated as being independent of blowing and the attitude, and that the dependency of the roll moment on the flaperon deflection can be approximated using a linear relation.

Included is a discussion on model uncertainties, the main source of which is considered to be aerodynamics. Specifically, the static moment characteristics and the time constants of the aerodynamic lags are treated as uncertain factors. Simplifications of the static moments for real-time implementation are also described.

The total FTB system is represented by a cascade connection of highly nonlinear uncertain aerodynamics that generates moments acting on the aircraft and a nonlinear rigid body aircraft dynamics.

The model motivates a definition of a class of nonlinear systems represented by a cascade connection of a nonlinear dynamical system and an uncertain linear dynamical system. A new approach to nonlinear control for the class of systems are developed in Chapter 4, and the nonlinear control is applied to the control of the FTB system in Chapter 5.

### 3.1 Rigid Body Dynamics

The equations of motion of the rigid body aircraft expressed in terms of the two degrees of freedom,  $\phi$  and  $\gamma$ , for large angles are developed in [34]. They are

$$I_x \ddot{\phi} + I_{xz} \ddot{\gamma} \cos \phi + (I_z - I_y) \dot{\gamma}^2 \sin \phi \cos \phi = m_{T1} \quad (3.1)$$

$$(I_A + I_y \sin^2 \phi + I_z \cos^2 \phi) \ddot{\gamma} + I_{xz} (\ddot{\phi} \cos \phi - \dot{\phi}^2 \sin \phi) + 2(I_y - I_z) \dot{\phi} \dot{\gamma} \sin \phi \cos \phi = m_{T2} \quad (3.2)$$

where,  $I_*$ 's represent the inertia properties about the point P and  $m_*$  represent moments. The suffixes are  $x, y, z$  for the body fixed orthonormal frame, 1 for the roll axis (body-fixed  $x$  axis), 2 for the "yaw" shaft axis (inertia frame), A for the "apparatus" and T for "total". (See Figure 2.2.) In the above equations

$$m_{T1} = m_1 + m_{f1} \quad (3.3)$$

$$m_{T2} = m_2 + m_{f2} + m_g + m_m$$

where  $m_1$  and  $m_2$  are the aerodynamic moments, and the other subscripts indicate the origin of additional moments:

$f$ : friction of bearings and potentiometer,

$g$ : gravity restoring moment,

$m$ : motor.

Incorporating an active torque cancellation (ATC) also developed in [34], yields torque applied by the motor equal to

$$m_m = -m_g + 0.9 I_A \ddot{\gamma} \quad (3.4)$$

The purpose of ATC is to eliminate the effect of the gravity torque and reduce the effect of the large moment of inertia of the apparatus (90% cancellation) so that the motion of the aircraft model is dominated by aerodynamic loads. For details about ATC, refer to Appendix B. Finally, the moments due to friction of the bearings and potentiometers can be written as:

$$m_{f1} = -c_{f1}\dot{\phi}, \quad m_{f2} = -c_{f2}\dot{\gamma} \quad (3.5)$$

Substituting (3.4) and (3.5) into (3.1) and (3.2) yields the equations of motion as:

$$I_x\ddot{\phi} + I_{xz}\ddot{\gamma} \cos \phi + (I_z - I_y)\dot{\gamma}^2 \sin \phi \cos \phi = m_1 - c_{f1}\dot{\phi} \quad (3.6)$$

$$(I_y \sin^2 \phi + I_z \cos^2 \phi + 0.1I_A)\ddot{\gamma} + I_{xz}(\ddot{\phi} \cos \phi - \dot{\phi}^2 \sin \phi) + 2(I_y - I_z)\dot{\phi}\dot{\gamma} \sin \phi \cos \phi = m_2 - c_{f2}\dot{\gamma} \quad (3.7)$$

These can be rewritten in Euler-Lagrange form as

$$H(q)\ddot{q} + C(q, \dot{q})\dot{q} = m - C_f\dot{q} \quad (3.8)$$

where,

$$q = [\phi \ \gamma]^T$$

$$H(q) = \begin{bmatrix} I_x & I_{xz} \cos \phi \\ I_{xz} \cos \phi & I_y \sin^2 \phi + I_z \cos^2 \phi + 0.1I_A \end{bmatrix}$$

$$C(q, \dot{q}) = \begin{bmatrix} 0 & (I_z - I_y)\dot{\gamma} \sin \phi \cos \phi \\ (I_y - I_z)\dot{\gamma} \sin \phi \cos \phi - I_{xz}\dot{\phi} \sin \phi & (I_y - I_z)\dot{\phi} \sin \phi \cos \phi \end{bmatrix}$$

$$C_f = \begin{bmatrix} c_{f1} & 0 \\ 0 & c_{f2} \end{bmatrix}$$

Finally, these equations can be written in a state-variable form by solving for  $\ddot{\phi}$  and  $\ddot{\gamma}$ :

$$\begin{bmatrix} \ddot{q} \\ \dot{q} \end{bmatrix} = \begin{bmatrix} 0 & I \\ 0 & -H(q)^{-1}\tilde{C}(q, \dot{q}) \end{bmatrix} \begin{bmatrix} q \\ \dot{q} \end{bmatrix} + \begin{bmatrix} 0 \\ H(q)^{-1} \end{bmatrix} m \quad (3.9)$$

$$\tilde{C}(q, \dot{q}) = C(q, \dot{q}) + C_f \quad (3.10)$$

Hence,

$$\dot{x} = f(x) + g(x)m, \quad f(0) = 0 \quad (3.11)$$

where  $x = [q^T \dot{q}^T]^T = [\phi \ \gamma \ \dot{\phi} \ \dot{\gamma}]^T$  and the vector  $m$  is the applied aerodynamic moment in each degree of freedom,  $m = [m_1 \ m_2]^T$ .

### 3.2 Aerodynamic Model

The model of the aerodynamic effects of FTB is based on the work [35,34] in which it was shown that the aerodynamic moments can be well modeled with lagged static loads. (Static and dynamic characteristics are described in Section 3.3.) That is,

$$\dot{\eta} = F_a \eta + G_a m_s(x, u) \quad (3.12)$$

$$m = H_a \eta \quad (3.13)$$

where  $\eta$  is the vector of internal states of the aerodynamics,  $m$  is the resultant aerodynamic moments, and  $u$  is the control input ( $u = [C_\mu \ \delta_f]^T$ ).  $m_s(x, u)$  is the vector of static aerodynamic moments, which are highly nonlinear functions of  $C_\mu$ . The static aerodynamic moments are described in Section 3.3. Since two independent first order lags for both aerodynamic moments are used,  $F_a$ ,  $G_a$  and  $H_a$  are expressed as:

$$F_a = \begin{bmatrix} -\frac{1}{\tau_1} & 0 \\ 0 & -\frac{1}{\tau_2} \end{bmatrix}, G_a = \begin{bmatrix} \frac{1}{\tau_1} & 0 \\ 0 & \frac{1}{\tau_2} \end{bmatrix}, H_a = \begin{bmatrix} 1 & 0 \\ 0 & 1 \end{bmatrix} \quad (3.14)$$

$\tau_i$ , ( $i = 1, 2$ ) is the time constant of the lag from  $m_{s_i}(x, u)$  to  $m_i$ . (Justification of the two independent lags is given in Section 3.3.2.) The numerical values are shown in Appendix A. The aerodynamic equation can be simplified as

$$\dot{m} = F_a m + G_a m_s(x, u), \quad (3.15)$$

because with the  $H_a = I$ ,  $\eta \equiv m$ .

### 3.3 FTB characteristics

FTB characteristics are discussed in this section. Static characteristics of FTB are introduced first, and a discussion of the dynamic characteristics then follows.

#### 3.3.1 Static characteristics

Figure 3.1 to Figure 3.6 show the static moment characteristics as functions of  $C_\mu$ , Figure 3.7 and Figure 3.8 show the effects of the aircraft model attitude ( $\phi$  and  $\gamma$ ). Figure 3.9 to Figure 3.12 provide data on the effect of the flaperon deflection ( $\delta_f$ ). Static moments (roll moment and “yaw” moment) are plotted for various  $C_\mu$ ,  $\delta_f$ ,  $\phi$  and  $\gamma$  in nondimensional coefficients,  $C_l$  (roll moment) and  $C_n$  (“yaw” moment). All the static data were measured over 3.0 seconds at 1,000Hz and averaged over the 3,000 data points. Each of these characteristics is described below.

##### Effect of $C_\mu$

Figure 3.1 to Figure 3.3 present roll and “yaw” moment coefficients as functions of  $C_\mu$  for various  $\phi$  with  $\delta_f = 0$  with  $\gamma$  fixed at  $0^\circ$ ,  $-10^\circ$ ,  $10^\circ$  respectively. Figure 3.4 to Figure 3.6 show data for various  $\gamma$  with  $\delta_f = 0^\circ$  with  $\phi$  fixed at  $0^\circ$ ,  $-20^\circ$ ,  $20^\circ$  respectively. The following observations can be made from the data.

- Both roll and “yaw” static moments are highly nonlinear functions of  $C_\mu$ .
- Nonlinearities of  $C_l$  and  $C_n$  as functions of  $C_\mu$  in small levels of blowing ( $|C_\mu| < 0.01$ ) are more severe than those in larger levels of blowing at any fixed  $\phi$  and  $\gamma$  in the sense that the slopes are steeper and the sign changes of the slopes are more frequent (especially in  $C_l$ ).
- Roll moment can be generated with small levels of blowing at almost all attitudes, although the characteristics change abruptly. For example,  $C_l$  curve in Figure 3.1 at  $\phi = 0^\circ$  reaches at maximum value ( $\approx 0.013$ ) at  $C_\mu \approx -0.004$ .
- “Yaw” moment exhibits cubic-like curves in small levels of blowing at any attitudes, which lead to control reversal. For example, the  $C_n$  curve in Figure 3.1 at  $\phi = 0^\circ$  changes the sign of the slope at  $C_\mu \approx 0.0015$  and changes the sign of the value at  $C_\mu \approx 0.003$ .



- Nonlinearities in the roll moment characteristic are more severe than that of “yaw” moment. For example, comparison between the  $C_l$  curve at  $\phi = 0^\circ$  and the  $C_n$  curve at  $\phi = 0^\circ$  in Figure 3.1 reveals that  $C_l$  curve changes more abruptly.
- Characteristics are not sector bounded nor do they pass through the origin.

### Effect of $\phi$ and $\gamma$

Figure 3.7 and Figure 3.8 show roll and yaw moment coefficients as functions of  $\phi$  and  $\gamma$  for various  $C_\mu$  with  $\delta_f = 0^\circ$ . Both coefficients are not highly nonlinear functions of  $\phi$  and  $\gamma$ . However, it can be seen that the stability derivatives ( $\frac{\partial C_l}{\partial \phi}$  and  $\frac{\partial C_n}{\partial \gamma}$ ) change due to  $C_\mu$ . (The slopes of the curves depend on  $C_\mu$ .) Static moment is symmetric in both  $\phi$  and  $\gamma$  regardless of  $C_\mu$ .

### Effect of flaperon (collective deflection)

Figure 3.9 shows the effects of the flaperons on the roll and the “yaw” moment for various  $C_\mu$  at  $\phi = 0^\circ, \gamma = 0^\circ$ . The data clearly show that the flaperon deflection ( $\delta_f$ ) is more effective in generating roll moment ( $C_l$ ) than does  $C_\mu$  while it has smaller effects on the “yaw” moment ( $C_n$ ) than  $C_\mu$ . The maximum change in  $C_l$  due to  $C_\mu$  is about 0.015 (for example, from the center curve corresponding to  $\delta_f = 0^\circ$ ), and the maximum change in  $C_l$  due to  $\delta_f$  is about 0.04 (the change in  $C_l$  from the center curve to the bottom one corresponding to  $\delta_f = +40^\circ$  for all values of  $C_\mu$ ). This is more than twice the change due to  $C_\mu$ . The maximum change in  $C_n$  due to  $C_\mu$  is about 0.25 (for example, from the center curve corresponding to  $\delta_f = 0^\circ$ ) and the maximum change in  $C_n$  due to  $\delta_f$  is at most about 0.05 for all values of  $C_\mu$ . This is about 1/5 of the change due to  $C_\mu$ . Figure 3.10, Figure 3.11 and Figure 3.12 respectively show the incremental moment changes due to the flaperon deflection. The effectiveness of the flaperon deflection in generating roll moments is, to a first approximation, independent of  $C_\mu, \phi$  and  $\gamma$ , since the curves are unaffected by changes in these quantities. Furthermore, all the curves are nearly straight lines. Therefore, the dependency of the roll moment on the flaperon deflection can be approximated as a linear relation. In contrast to the roll moment, the “yaw” moment changes due to the flaperon deflection cannot be approximated by a linear relation, but the amount of the changes is much smaller than the changes due to blowing. As explained above, the effectiveness of the flaperon in generating “yaw” moments is at most about 1/5 of that of  $C_\mu$ .

### 3.3.2 Dynamic characteristics

#### Effect of $C_\mu$

The measured time histories for roll and yaw moment responses to blowing are presented in Figure 3.13 [34] as well as first order lag approximations. It is seen that the first order lag approximation adequately represents the response of roll and yaw moments.

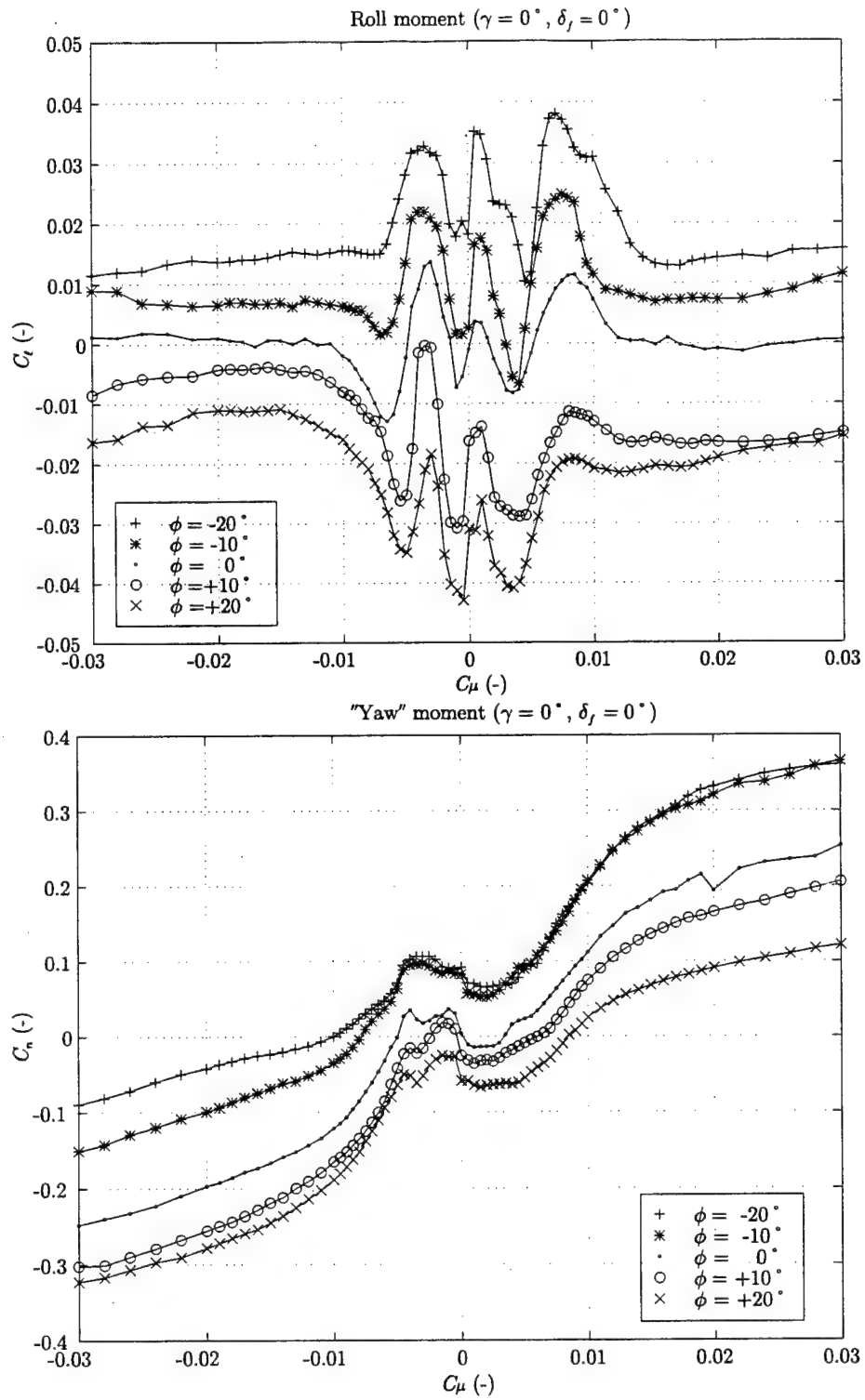
#### Effect of flaperon (collective deflection)

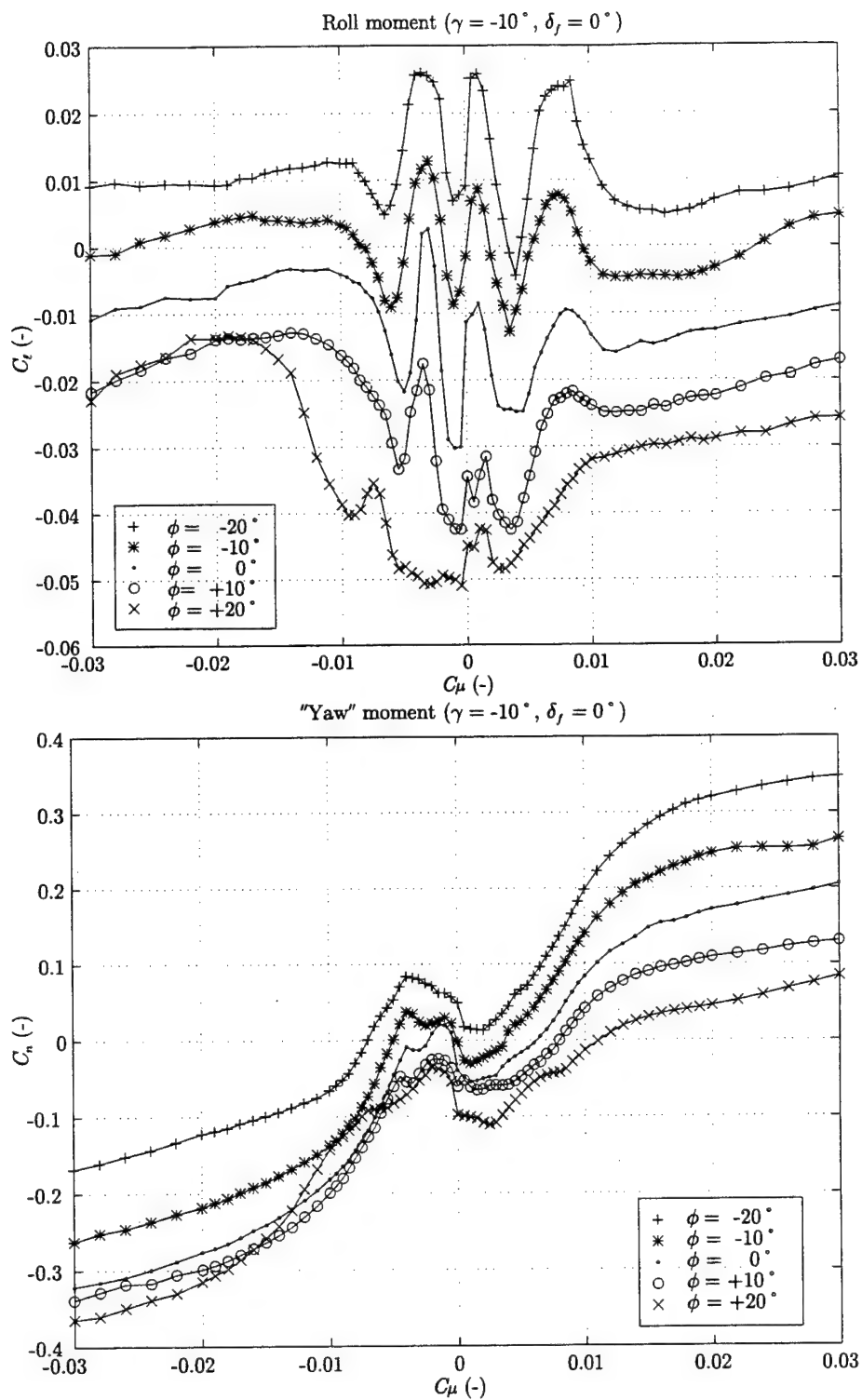
Figure 3.14 shows roll moment response to the deflection of flaperons. The first order lag approximation is also shown in the same plot. As in the case of blowing, the response to the flaperon is also well approximated with the first order lag.

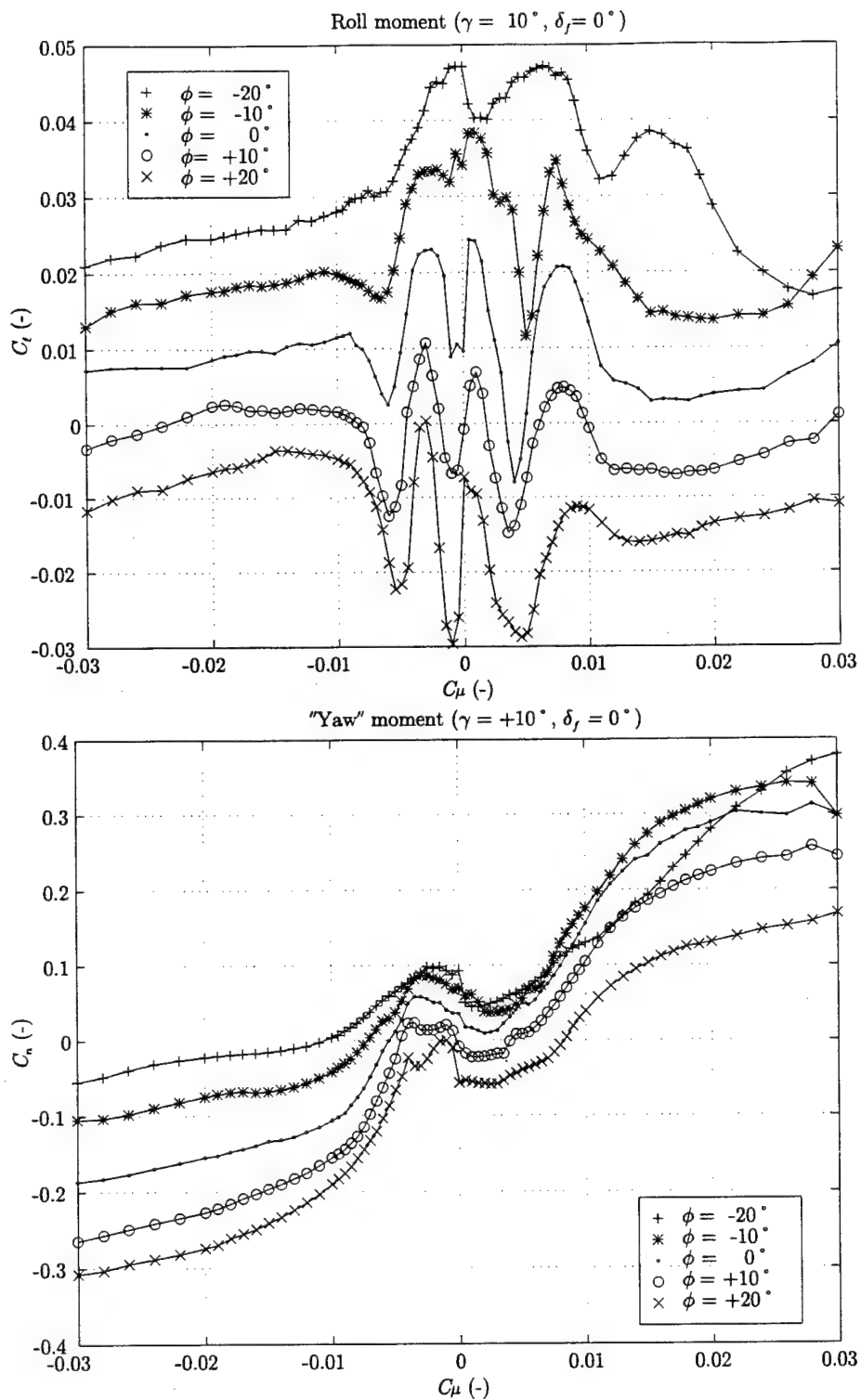
### 3.3.3 Summary

Static roll and “yaw” moments are highly nonlinear functions of the amount of blowing in the small levels of blowing in the sense that the slopes are steep or the sign changes of the slopes are frequent, while they are well behaved in the large levels of blowing.

The effect of the attitude on moments is well behaved. Effectiveness of flaperons in generating roll moment can be approximated as being independent of blowing and the attitude, and the dependency of the roll moment on the flaperon deflection can be approximated as a linear relation. The dynamic effects can be adequately approximated with first order lags.

Figure 3.1: Roll/"Yaw" moment v.s.  $C_\mu, \phi$  ( $\gamma = 0^\circ, \delta_f = 0^\circ$ )

Figure 3.2: Roll/"Yaw" moment v.s.  $C_\mu, \phi$  ( $\gamma = -10^\circ, \delta_f = 0^\circ$ )

Figure 3.3: Roll/"Yaw" moment v.s.  $C_\mu, \phi$  ( $\gamma = 10^\circ, \delta_f = 0^\circ$ )

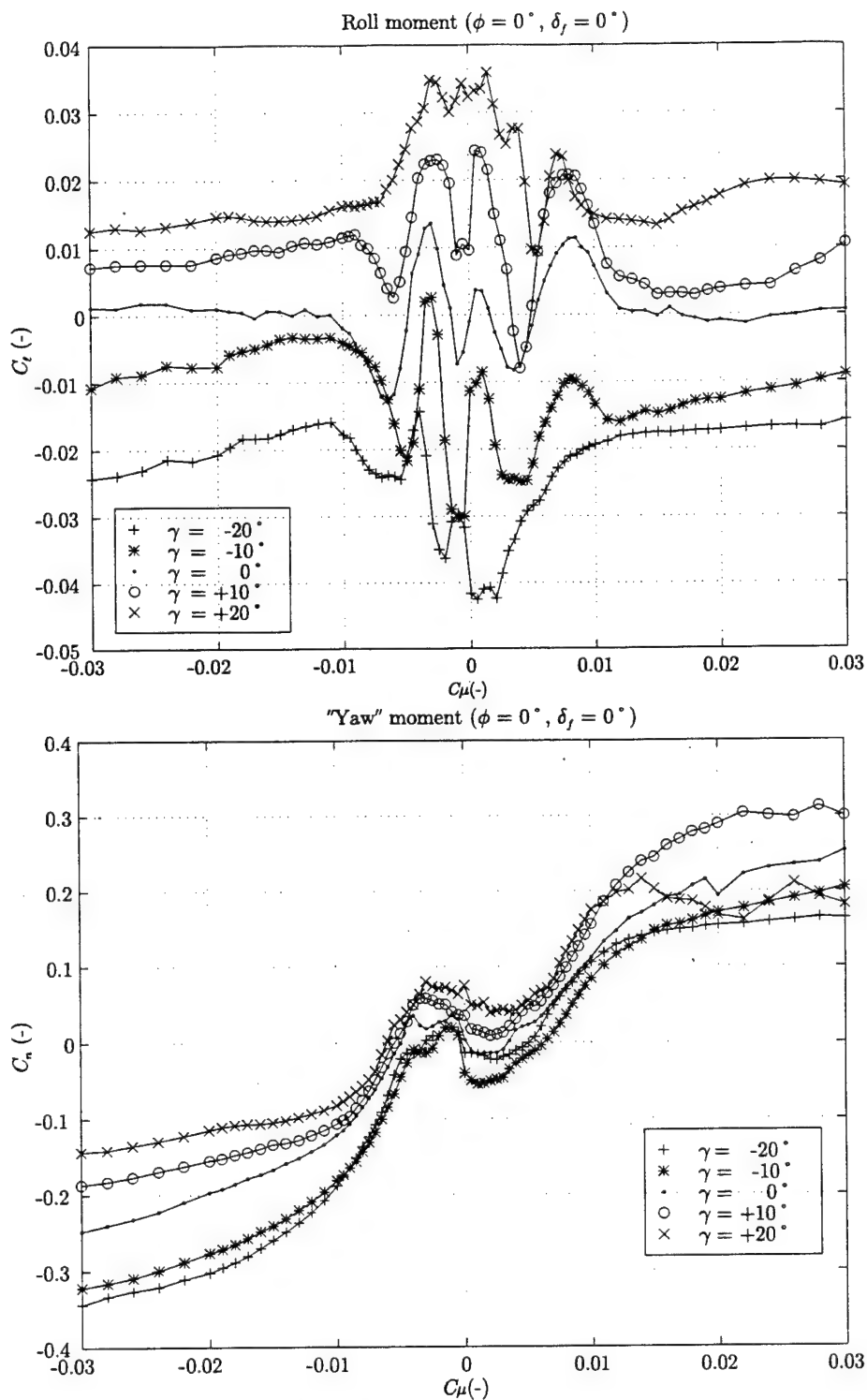
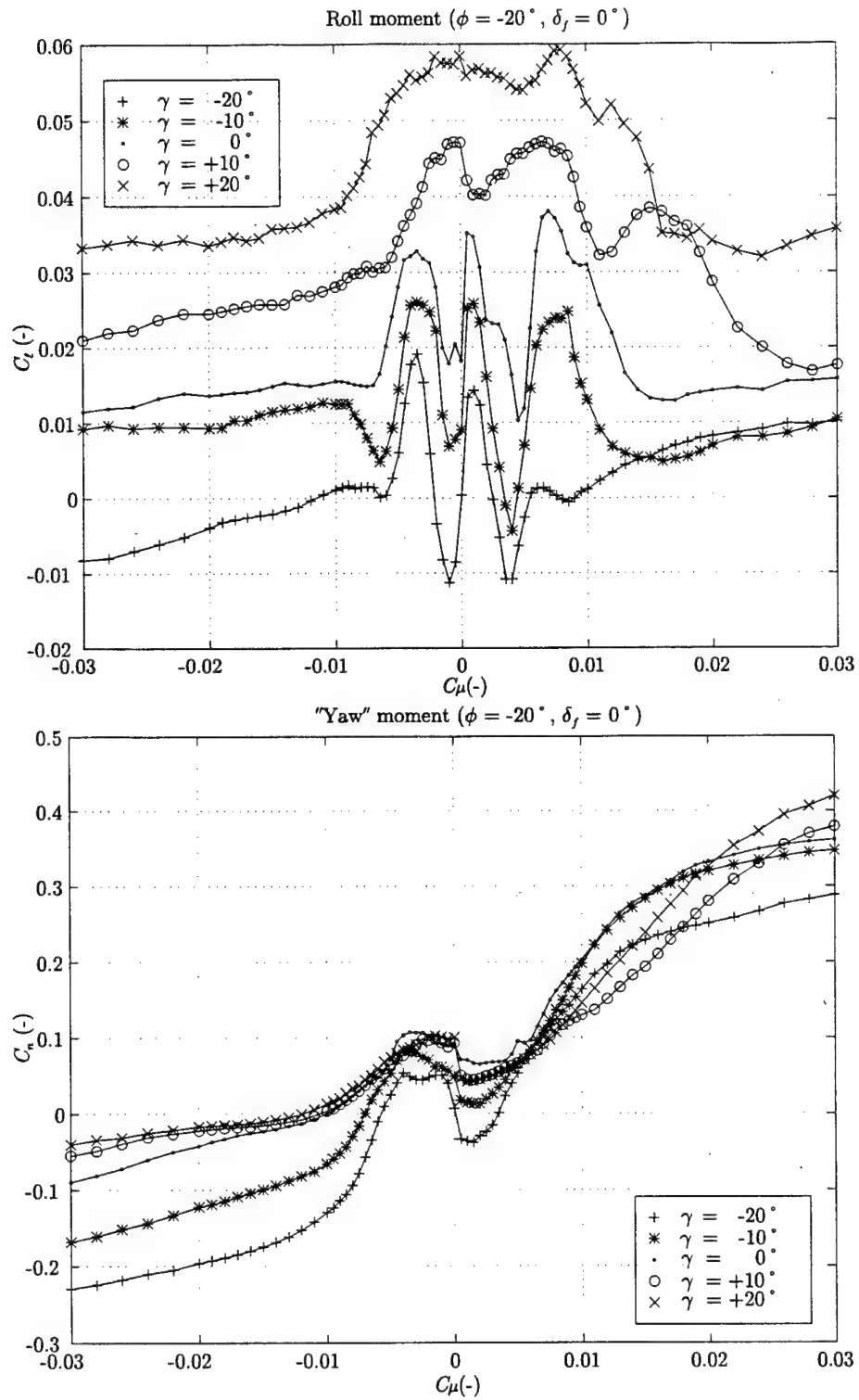
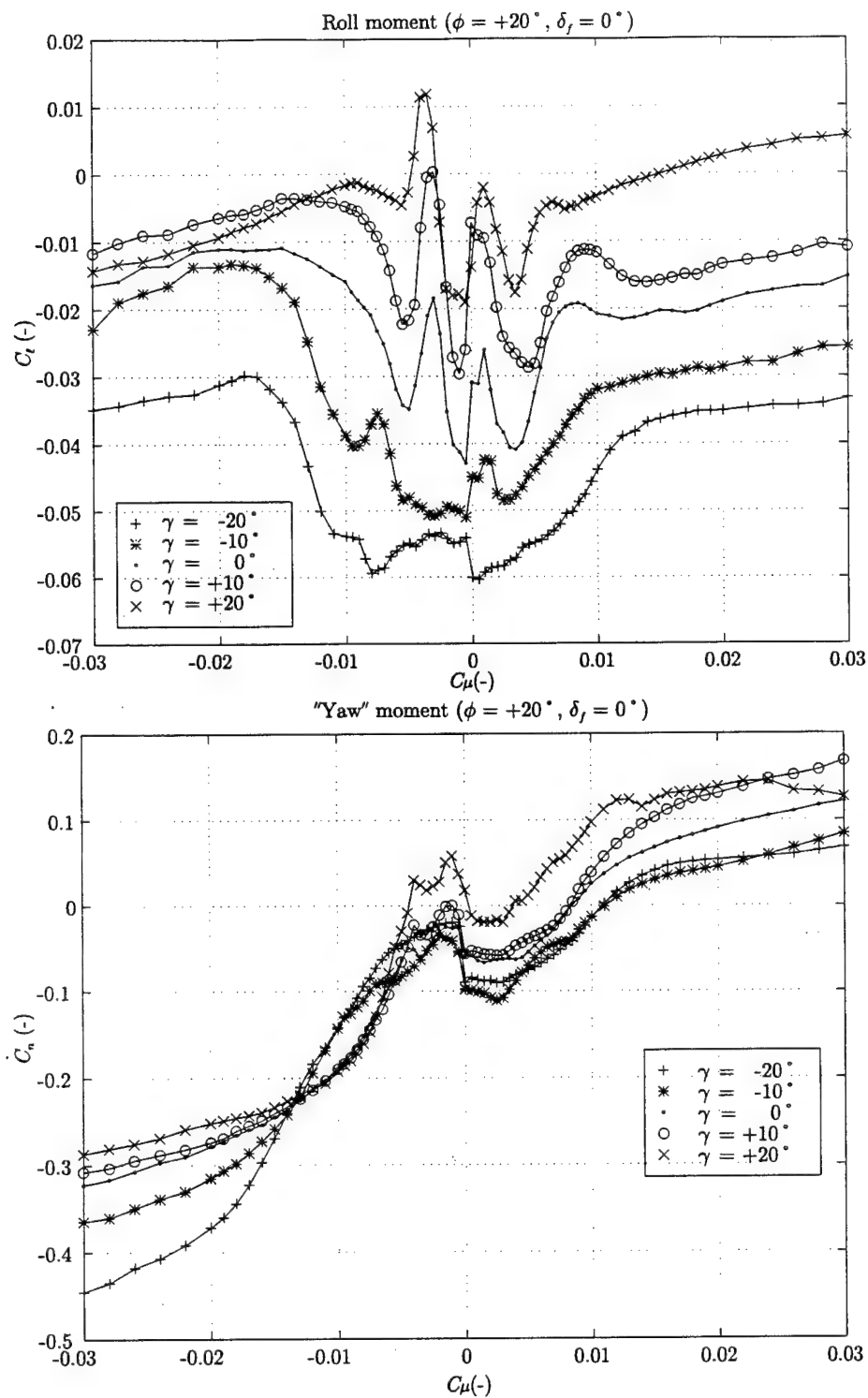
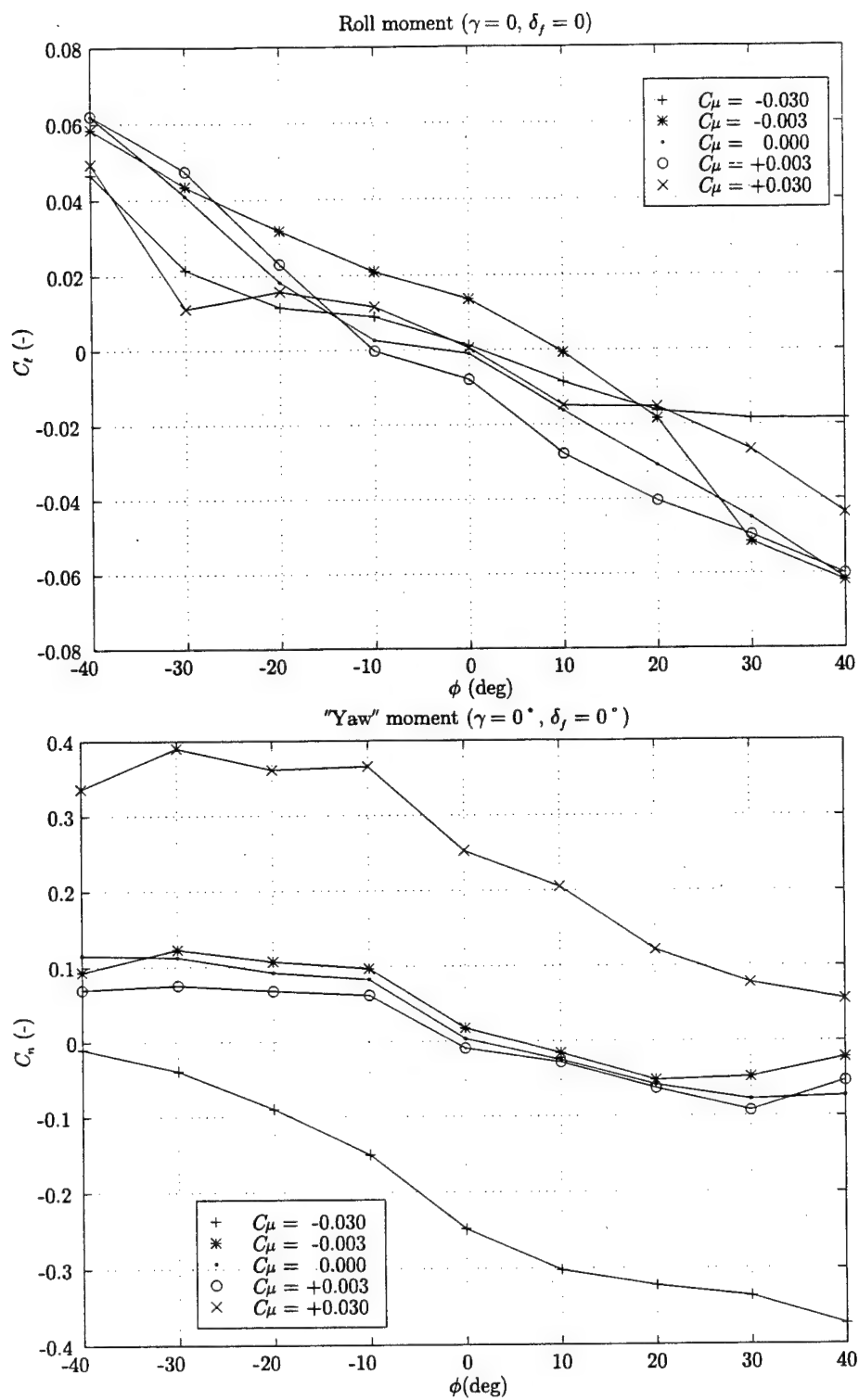


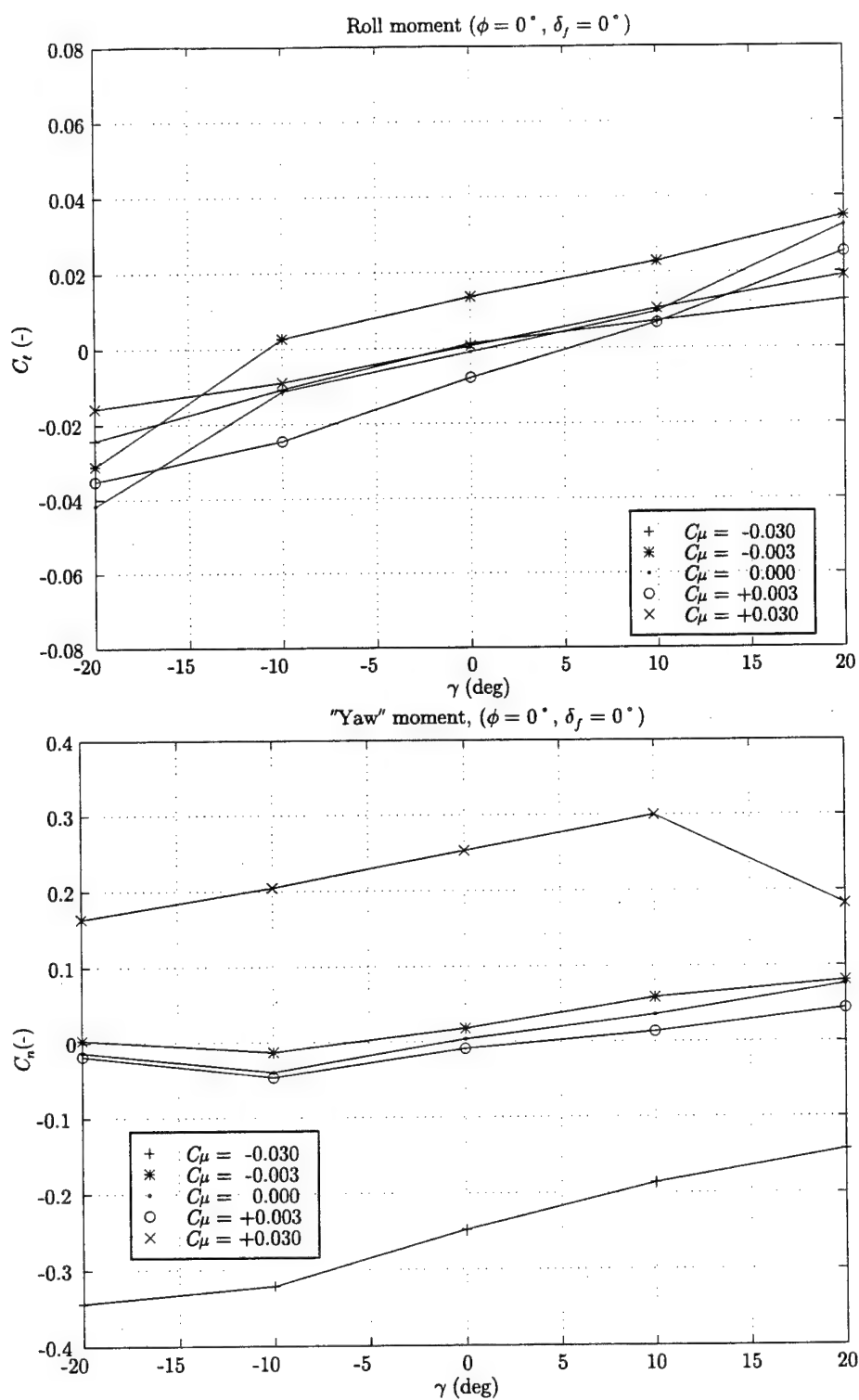
Figure 3.4: Roll/"Yaw" moment v.s.  $C_\mu, \gamma$  ( $\phi = 0^\circ, \delta_f = 0^\circ$ )

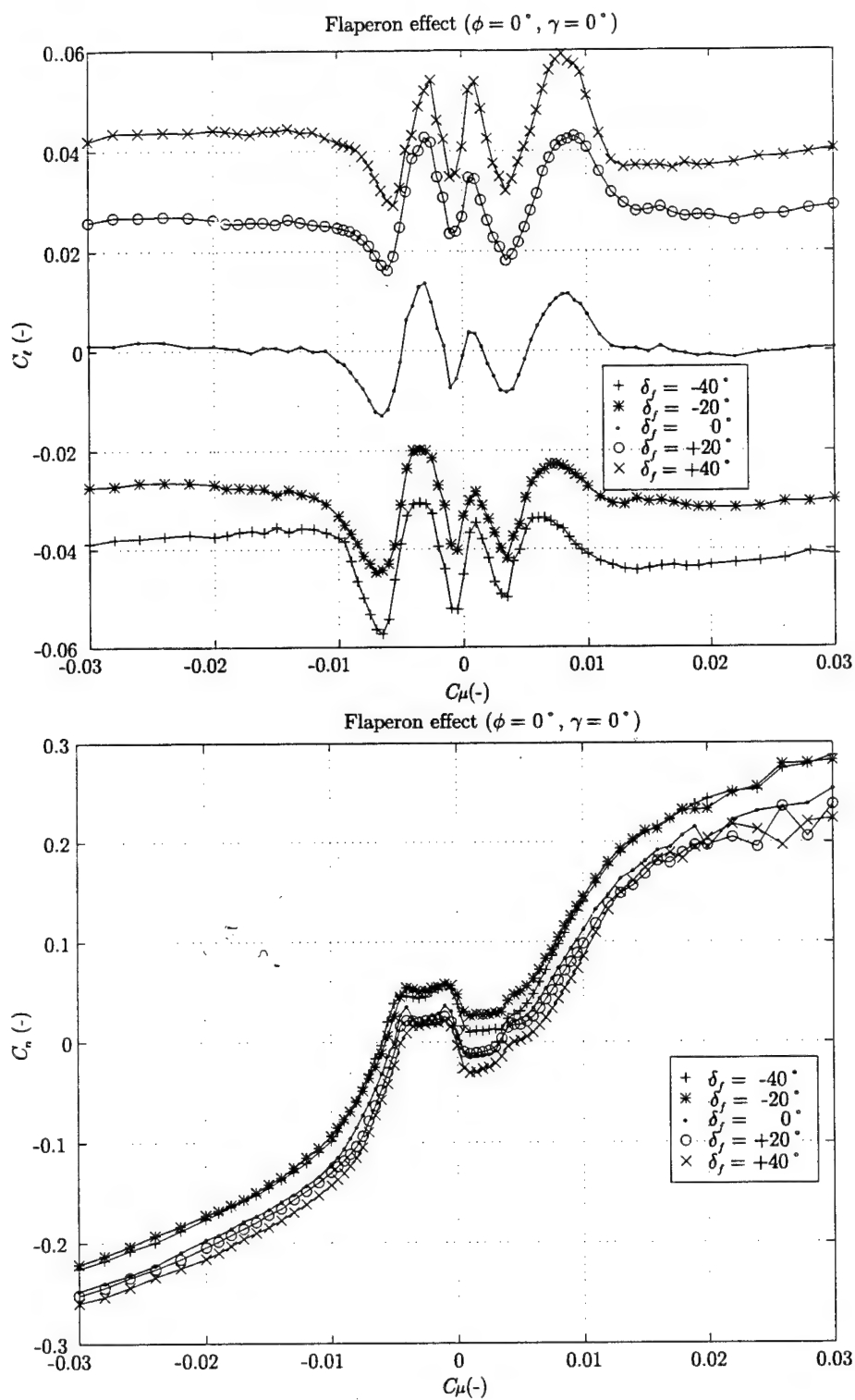


Figure 3.6: Roll/"Yaw" moment v.s.  $C_{\mu}$ ,  $\gamma$  ( $\phi = 20^\circ$ ,  $\delta_f = 0^\circ$ )



Figure 3.7: Roll/"Yaw" moment v.s.  $\phi, C_\mu$  ( $\gamma = 0^\circ, \delta_f = 0^\circ$ )

Figure 3.8: Roll/"Yaw" moment v.s.  $\gamma, C_\mu$  ( $\phi = 0^\circ, \delta_f = 0^\circ$ )

Figure 3.9: Roll/"Yaw" moment v.s.  $C_\mu, \delta_f$  ( $\phi = 0^\circ, \gamma = 0^\circ$ )

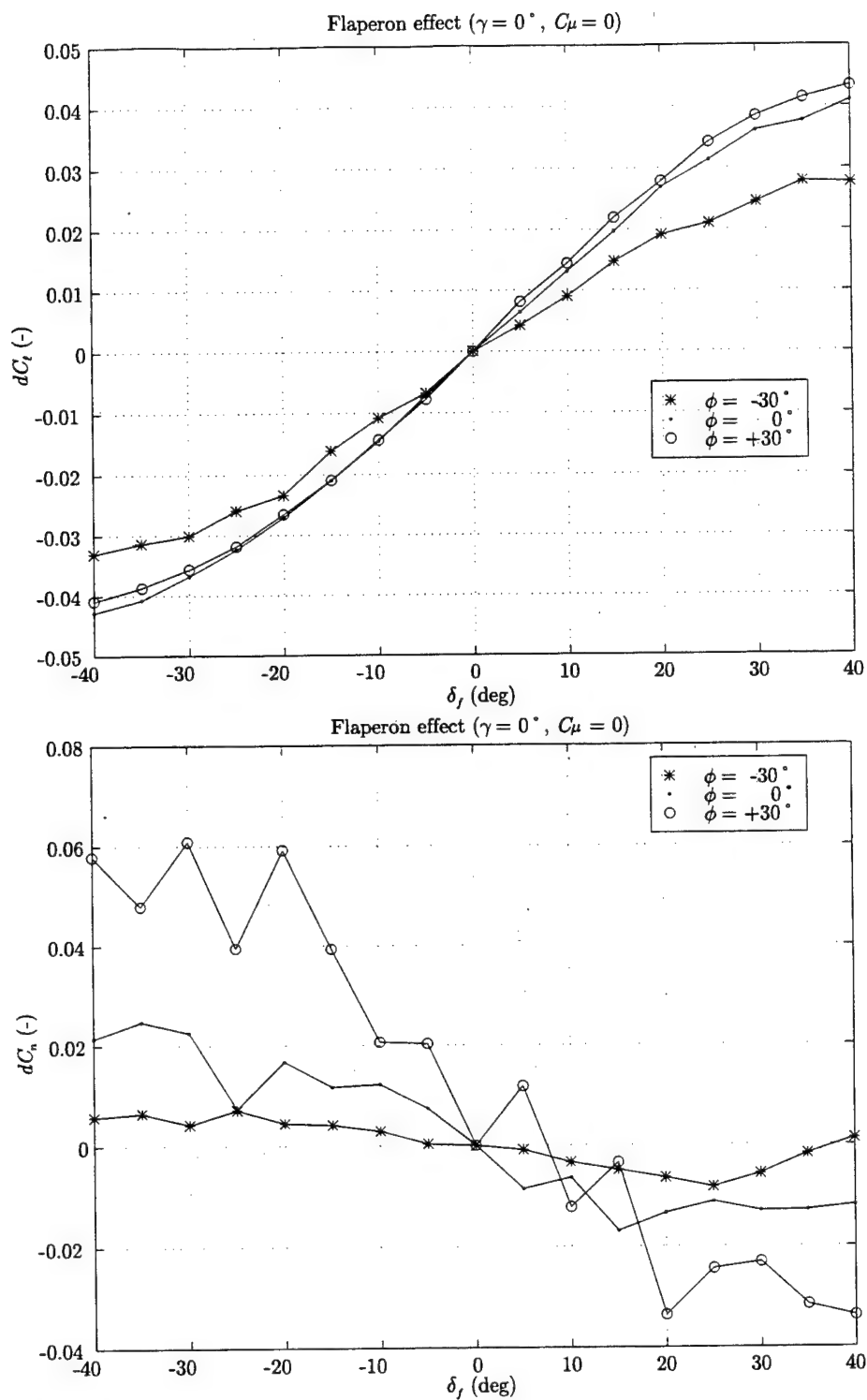


Figure 3.10: Roll/"Yaw" moment increment v.s.  $\delta_f$ ,  $\phi$  ( $\gamma = 0^\circ$ ,  $C_\mu = 0$ )

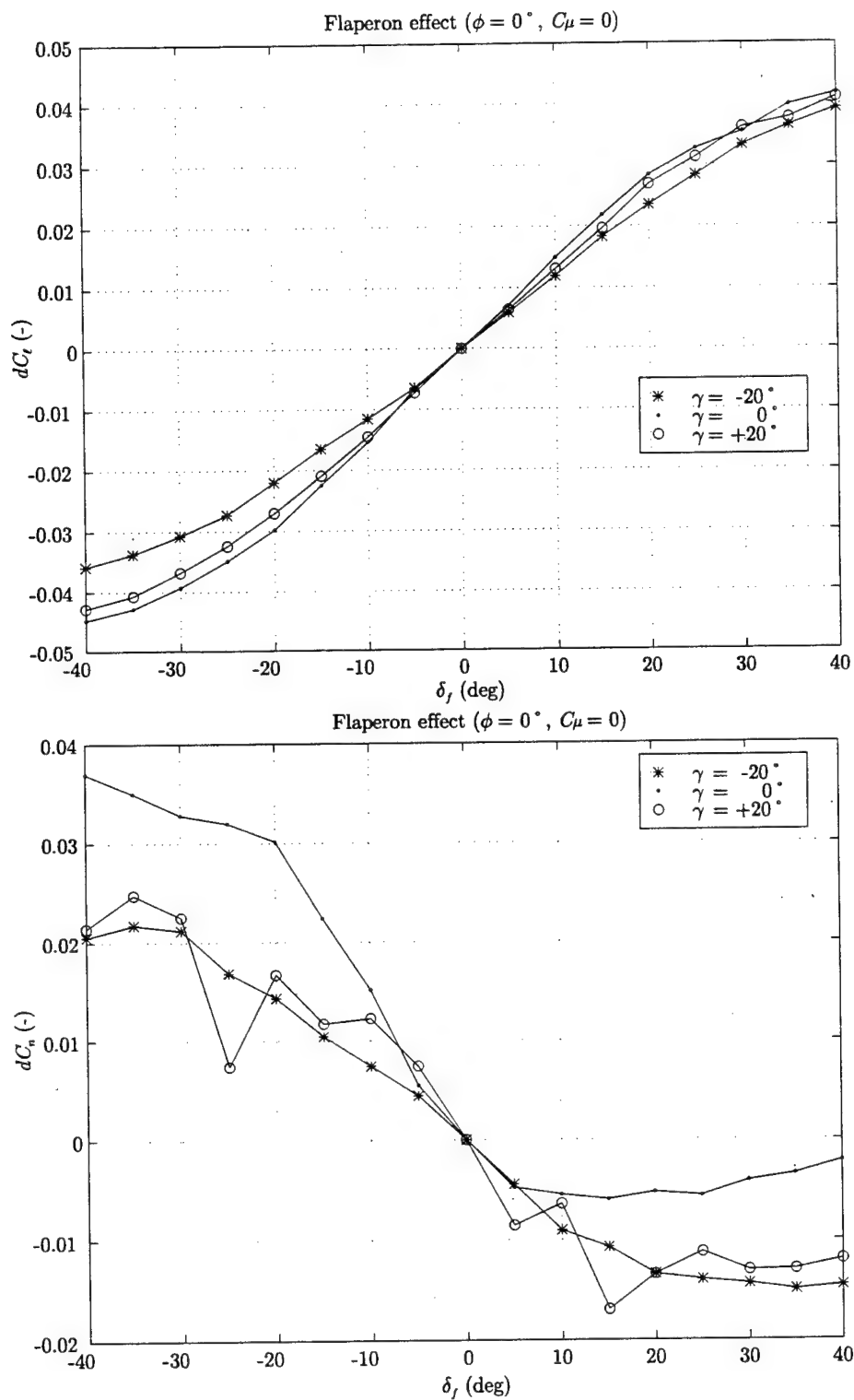
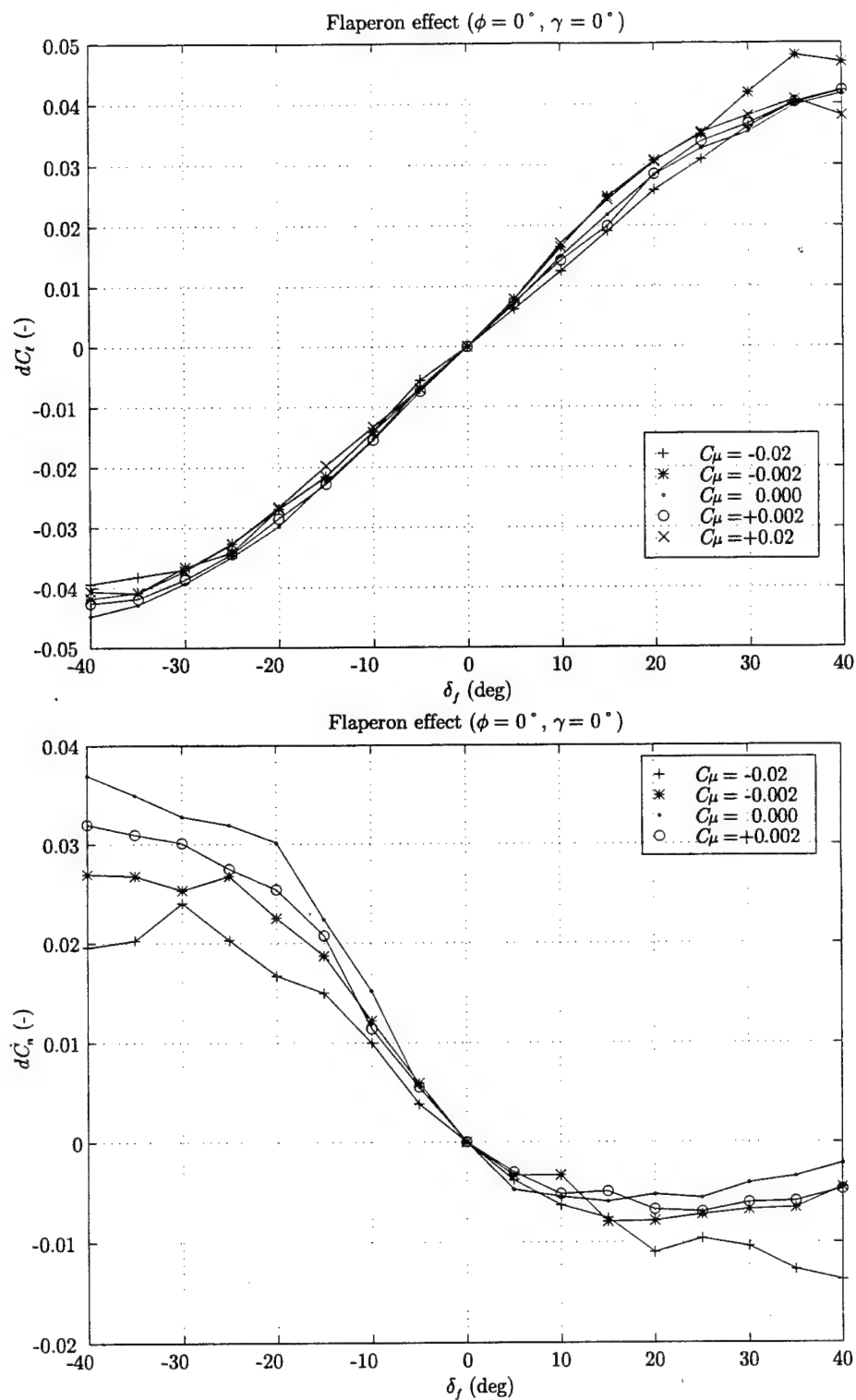


Figure 3.11: Roll/"Yaw" moment increment v.s.  $\delta_f, \gamma$  ( $\phi = 0^\circ$ ,  $C_\mu = 0$ )

Figure 3.12: Roll/"Yaw" moment increment v.s.  $\delta_f, C_\mu$  ( $\phi = 0^\circ, \gamma = 0^\circ$ )

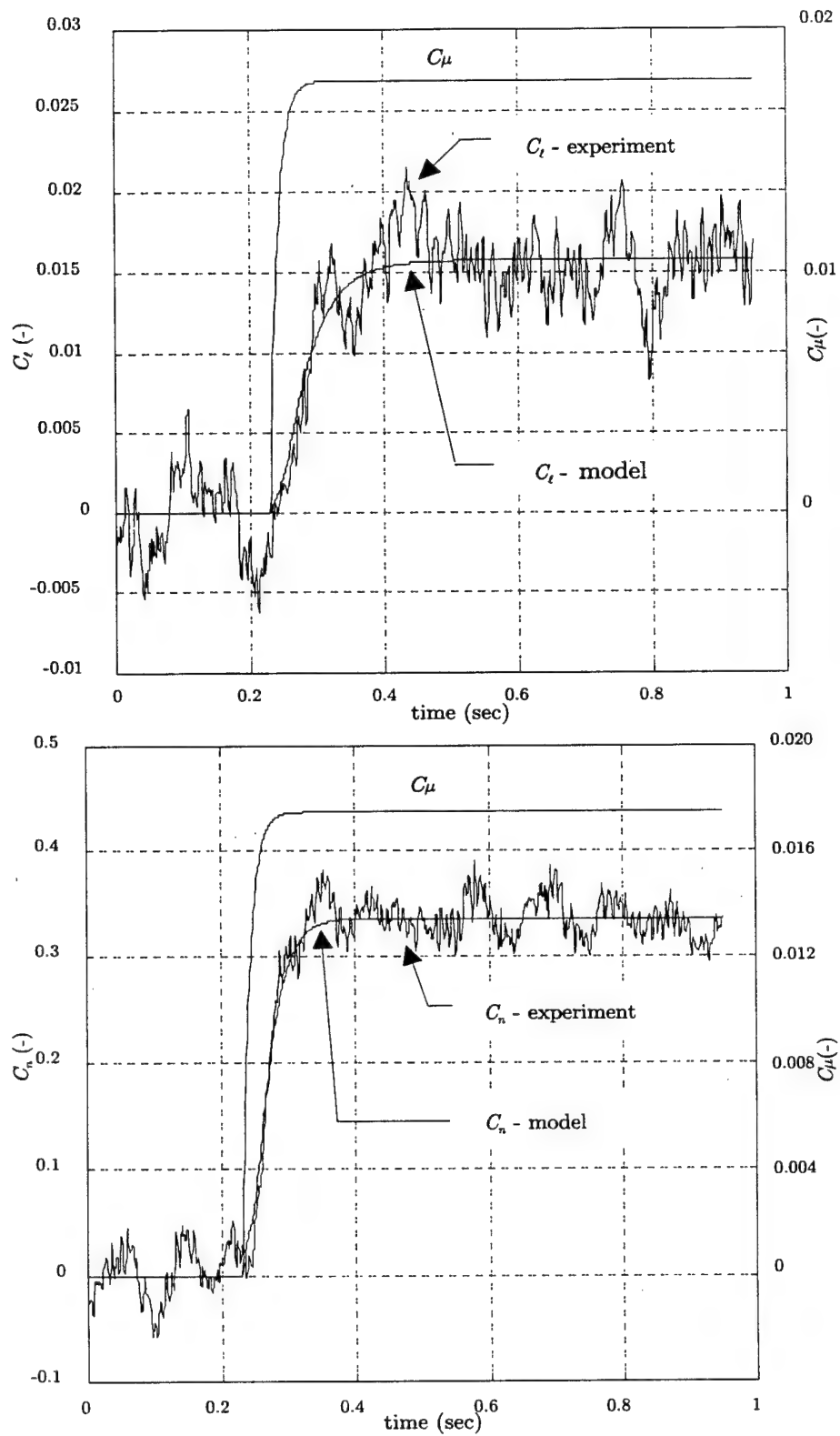


Figure 3.13: Transient moment due to blowing

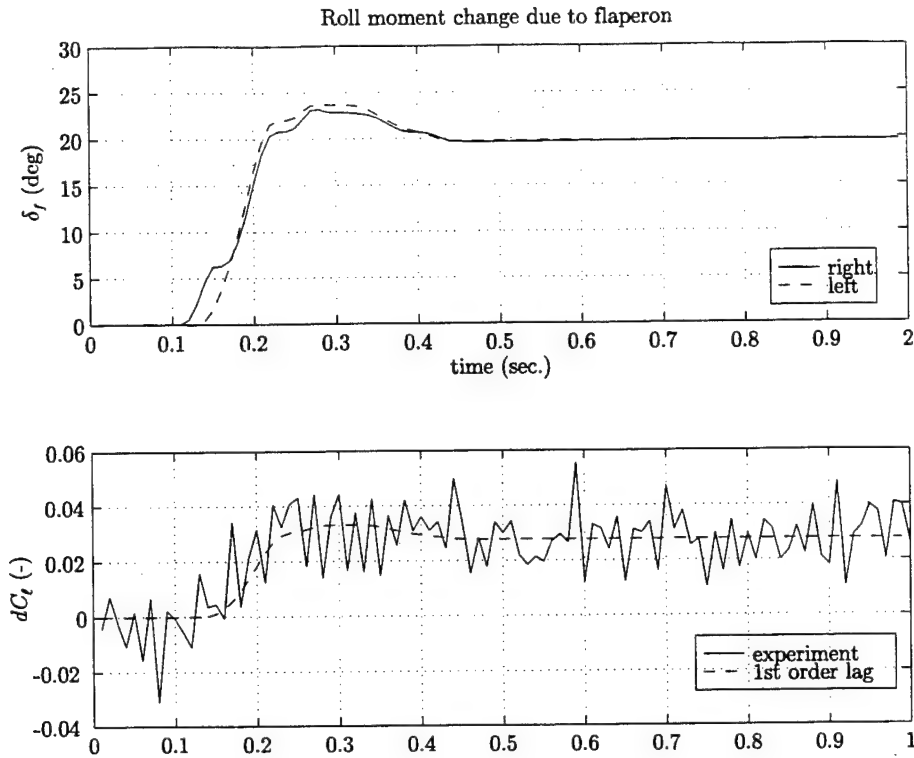


Figure 3.14: Transient roll moment due to flaperon

### 3.4 Model Uncertainties

For this research, it is assumed that all the properties of the rigid body are assumed known. (If there were uncertain parameters in the rigid body dynamics, they would be treated in the “virtual control design” described in Section 4.2.1 and Section 5.1.3.) The aerodynamics is considered to be the source of uncertainties. Further, the static moment characteristics are the dominant uncertain factor in the system. The uncertainties of the static moments come from the measurement errors of the static moments, the errors in the  $C_\mu$  servo control and variations in the air speed.

The static moment  $m_s(x, u)$ , which is a function of the rigid body states ( $x$ ) and the input ( $u = [C_\mu \delta_f]^T$ ), can be decomposed as follows:

$$m_s(x, u) = \bar{m}_s(x, u) + \delta m_s(x, u). \quad (3.16)$$



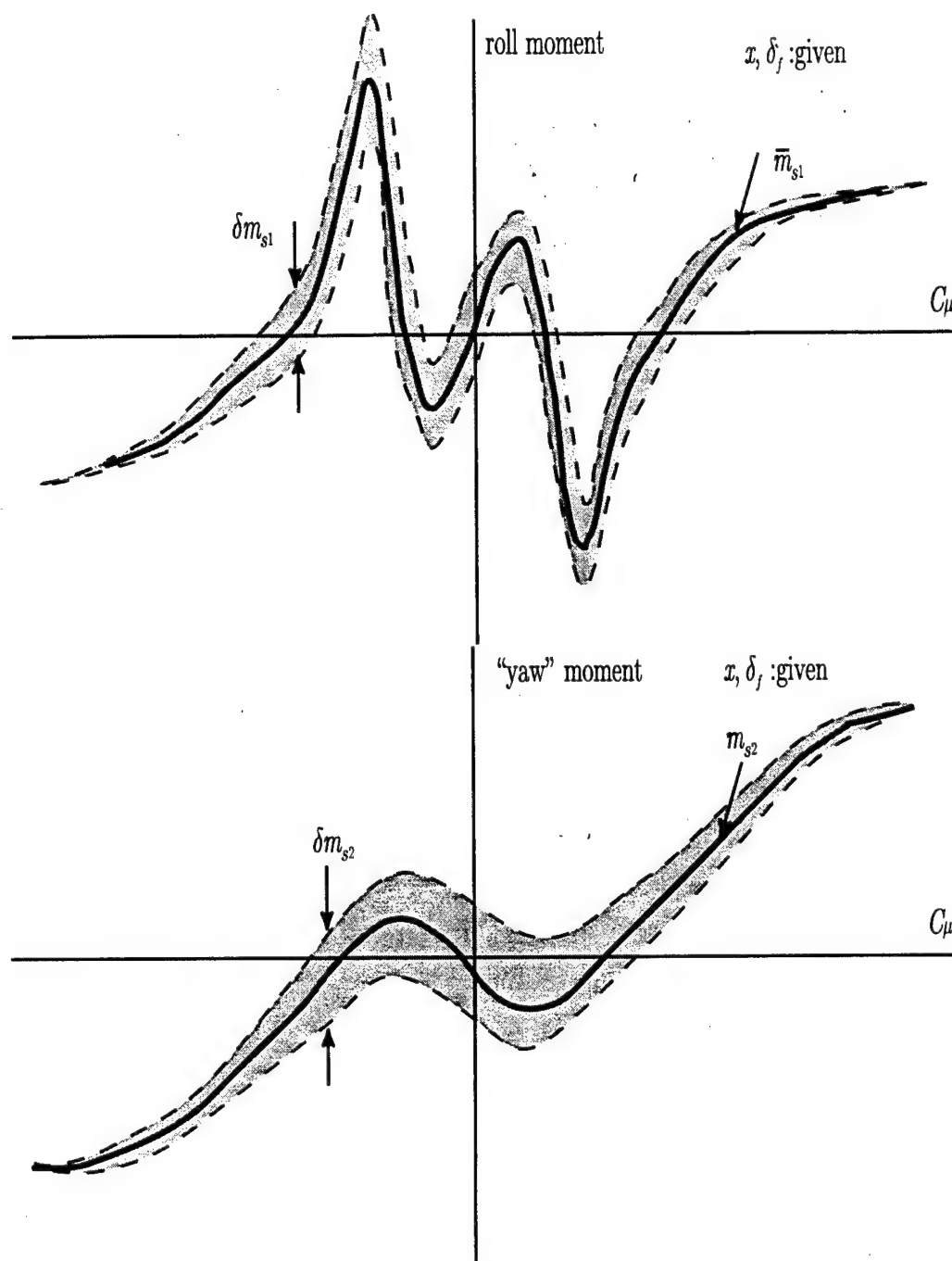


Figure 3.15: Uncertain Static Moment

where  $\bar{m}_s(x, u)$  is the vector of known nominal static aerodynamic moments given in numerical data (e.g. Figure 3.1), and  $\delta m_s(x, u)$  is the vector of uncertain static aerodynamic moments. Schematically, the uncertain static moment is shown in Figure 3.15. The constants  $\tau_1$  and/or  $\tau_2$  can also be uncertain. Hence, (3.15) can be expressed in the following form,

$$\dot{m} = (F_a + \delta F_a)m + (G_a + \delta G_a)(\bar{m}_s(x, u) + \delta m_s(x, u)). \quad (3.17)$$

If all the system uncertainties are lumped into  $w$ , defined as

$$w = G_a^{-1}(\delta F_a m + G_a \delta m_s(x, u) + \delta G_a \bar{m}_s(x, u) + \delta G_a \delta m_s(x, u)), \quad (3.18)$$

( $G_a$  is invertible. Refer to (3.14).) the resulting equation becomes

$$\dot{m} = F_a m + G_a(\bar{m}_s(x, u) + w). \quad (3.19)$$

Note that each component of  $w$  is not necessarily small but it is assumed bounded by an unknown constant, that is,

$$|w_i| \leq \rho_i \text{ (unknown)}, \quad (i = 1, 2). \quad (3.20)$$

### 3.5 Nominal Static Aerodynamic Moment

On constructing the nominal static aerodynamic moments,  $\bar{m}_{s_2}$  ("yaw") is assumed to be independent of  $\delta_f$ , because the effectiveness of  $\delta_f$  is much smaller than that of  $C_\mu$ . (It is at most about 1/5 of that of  $C_\mu$ . See Section 3.3.1 for more details.) Further, it is assumed that  $\bar{m}_{s_1}$  (roll) linearly depends on  $\delta_f$ . (It is shown in Section 3.3.1 that the dependency of roll moment on the flaperon deflection can be approximated using a linear relation.) Therefore, we have the expressions:

$$\bar{m}_{s_1}(x, u) = \bar{m}_{s_1}(x, C_\mu, \delta_f) = \bar{m}_{s_1}(x, C_\mu) + k_{\delta_f} \delta_f \quad (3.21)$$

$$\bar{m}_{s_2}(x, u) = \bar{m}_{s_2}(x, C_\mu) \quad (3.22)$$

The neglected effects of the flaperon deflection on  $m_s$  are regarded as part of  $\delta m_s$ . These simplifications facilitate the real-time implementation of control because the process of finding control inputs ( $C_\mu$  and  $\delta_f$ ) can be very complicated and time-consuming. With

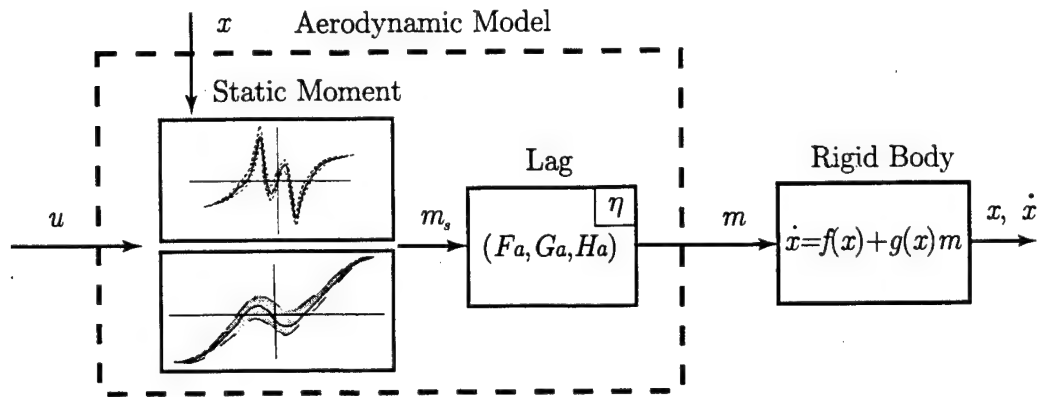


Figure 3.16: Block Diagram of FTB system structure

these simplifications, iterations for finding control inputs can be avoided. (Refer to Section 4.2.3.) For the purpose of 2-DOF control, FTB is used for controlling “yaw” ( $\gamma$ ) motion and the flaperons for roll ( $\phi$ ) motion.

### 3.6 FTB system

Combining (3.11) and (3.19) yields the final form of the system.

$$\dot{x} = f(x) + g(x)m \quad (3.23)$$

$$\dot{m} = F_a m + G_a(\bar{m}_s(x, u) + w) \quad (3.24)$$

Since both angular accelerations are assumed to be available for control and both angular rates are obtainable by numerically differentiating the roll and “yaw” angles, the measured output vector is

$$y = [q^T \dot{q}^T \ddot{q}^T]^T = [\phi \gamma \dot{\phi} \dot{\gamma} \ddot{\phi} \ddot{\gamma}]^T. \quad (3.25)$$

Note that angular accelerometers are available in the experimental system, and they can be provided on operational aircraft.

Finally each component of  $w$  is assumed to be bounded by

$$|w_i| \leq \rho_i \text{ (unknown), } (i = 1, 2). \quad (3.26)$$

The complete FTB system structure is depicted in Figure 3.16. The FTB system is represented by a cascade connection of highly nonlinear uncertain aerodynamics that generates moments acting on the aircraft and a nonlinear rigid body aircraft dynamics.

### 3.7 Summary

In this chapter, a mathematical model of the FTB system is developed. The FTB system is described as a cascade connection of highly nonlinear uncertain aerodynamics and nonlinear rigid body dynamics. The aerodynamics are modeled as first-order lagged static moments, which are highly nonlinear functions of the amount of blowing. The actual data of these nonlinear functions are presented.

The main source of the model uncertainties is considered to be aerodynamics. Specifically, the static moment characteristics and the time constants of the aerodynamic lags are treated as uncertain factors. Simplifications of the static moment characteristics are introduced for real-time implementation of the control laws developed in Chapter 4.

## Chapter 4

# Approach to Nonlinear Control

In this Chapter, a new nonlinear approach is developed for the control of a class of nonlinear systems represented by a cascade connection of a nonlinear dynamical system and an uncertain linear dynamical system. The FTB system developed in the previous chapter is of this class.

The approach yields a technique that robustly inverts the highly nonlinear and uncertain characteristics by taking the effect of uncertainties on the stability into account.

The approach is applied to the FTB system and the results in simulations and experiments are presented in Chapter 5. The control is shown to allow the system to operate in a region where the characteristics are highly nonlinear and uncertain and hence achieves the goal of reducing the amount of air required.

The control design consists of three simple steps. The first step is to design a virtual control, the second step is to construct a reduced order observer for the internal states if required, and the last step is to design a High-Gain Lyapunov control. Time-scale separation of each step is possible since the time scale of each step is specifiable. Information on the upper bounds of uncertainties is not required. If the information on the bounds is available, however, the worst-case performance can be evaluated *a priori* and the design parameters can be computed *a priori* that guarantee the required performance. Also a full dimensional Lyapunov function for the whole system is not required to generate the control law. Only a quadratic Lyapunov function for a lower dimensional manifold is used which simplifies the design process. Further, the design allows the trade-off between the performance and the control efforts by simply increasing or decreasing design parameters.

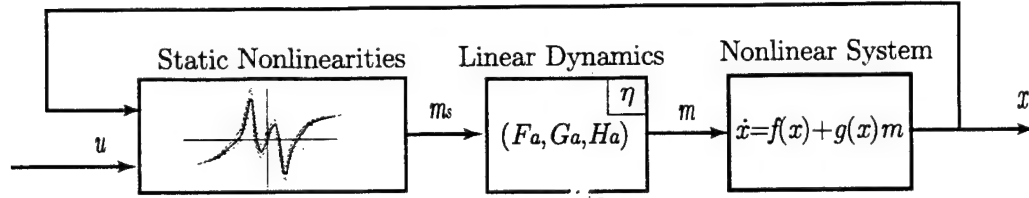


Figure 4.1: Block Diagram of nonlinear system under consideration

The chapter begins with the problem statement in which the system description and the assumptions regarding the system are described. Each step of the nonlinear control design is explained in detail and the proof of stability is given.

## 4.1 Problem Statement

### 4.1.1 System Description

The system under consideration is described as a cascade connection of a nonlinear dynamical system (main system, (4.1)) and an uncertain linear dynamical system (subsystem, (4.2), (4.3)) with uncertain static nonlinearities. The system class includes the FTB system developed in the previous chapter, but is more general because the linear subsystem (subsystem, (4.2), (4.3)) is not constrained to have only independent first order lags. The dynamics of the system are:

$$\dot{x} = f(x) + g(x)m \quad (4.1)$$

$$\dot{\eta}_o = (F_{a_o} + \delta F_a)\eta_o + (G_{a_o} + \delta G_a)(\bar{m}_s(x, u) + \delta m_s(x, u)) \quad (4.2)$$

$$m = H_{a_o}\eta_o \quad (4.3)$$

The measured output is

$$y = [x^T \ m^T]^T. \quad (4.4)$$

where  $x \in R^{n_x}$ ,  $\eta_o \in R^{n_\eta}$ ,  $m_s \in R^{n_m}$ ,  $m \in R^{n_m}$ ,  $u \in R^{n_u}$  and  $y \in R^{n_x+n_m}$  and  $n_\eta \geq n_m$ .  $F_{a_o}$ ,  $G_{a_o}$  and  $H_{a_o}$  are known nominal constant matrices of appropriate size.  $\delta F_a$  and  $\delta G_a$  are uncertain matrices.  $\bar{m}_s(x, u)$  is the vector of known nominal nonlinearities and  $\delta m_s(x, u)$  is the vector of uncertain nonlinearities. The block diagram is depicted in Figure 4.1.

## 4.1.2 Assumptions

Main system:

- $f(x)$  and  $g(x)$  are known.
- $g(x)$  is affinely bounded, i.e.,  $\exists c_{g_i} \geq 0$  ( $i = 1, 2$ ) such that

$$\|g(x)\|_2 \leq c_{g_1}\|x\|_2 + c_{g_2} \quad (4.5)$$

- $x$  is measurable.

Subsystem:

- All the uncertainties can be collected into a lumped uncertainty  $w \in R^{n_m}$  which satisfies the matching condition [27], i.e.,

$$G_{a_o}w = \delta F_a \eta_o + G_{a_o} \delta m_s(x, u) + \delta G_a \bar{m}_s(x, u) + \delta G_a \delta m_s(x, u), \quad (4.6)$$

$\forall x \in R^{n_x}, \forall \eta_o \in R^{n_\eta}, \forall u \in R^{n_u}, \forall \delta F_a, \forall \delta G_a$  and  $\forall \delta m_s(x, u)$  given  $F_{a_o}, G_{a_o}$  and  $\bar{m}_s(x, u)$ . Then, the subsystem (4.2) becomes

$$\dot{\eta}_o = F_{a_o} \eta_o + G_{a_o}(\bar{m}_s(x, u) + w). \quad (4.7)$$

- Each component of the unknown  $w$  is not necessarily small but is bounded by an unknown constant, i.e.,

$$|w_i| \leq \rho_i \text{ (unknown)}, \quad (i = 1, \dots, n_m). \quad (4.8)$$

$\forall x \in R^{n_x}, \forall u \in R^{n_u}$  and  $\forall \eta_o \in D$  where  $D = \{\eta_o \in R^{n_\eta} \mid \|\eta_o\|_2 < \infty\}$ .

- $F_a, G_a$  and  $H_a$  satisfy the following conditions.

1. The triple  $(F_{a_o}, G_{a_o}, H_{a_o})$  is minimal.
2.  $G_{a_o}$  and  $H_{a_o}$  are full rank.
3.  $\det(H_{a_o}G_{a_o}) \neq 0$  (relative degree is one.)
4. Invariant zeros of  $(F_{a_o}, G_{a_o}, H_{a_o})$  are in the open left half-complex plane.  
(Minimum phase)

- $m$  is measurable.

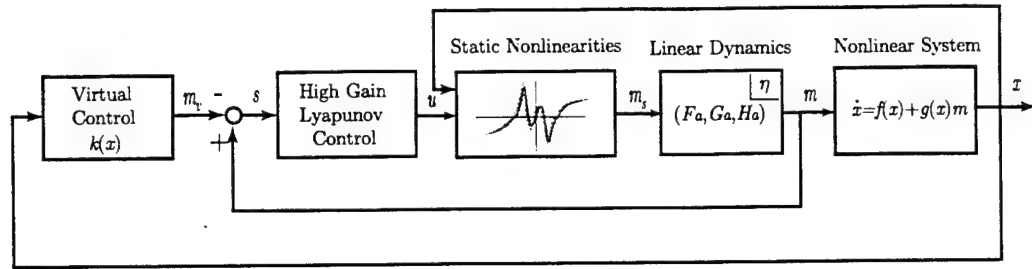


Figure 4.2: Block Diagram of Controller/Plant structure

## 4.2 Nonlinear Control Design

Given an uncertain nonlinear system in the class described above, the control should address the following three standard issues associated with all control design: The control must provide adequate performance, be sufficiently robust, and must minimize the amount of control power consumed. An approach to designing a nonlinear control is developed here that blends High Gain Control [31, 49], and Lyapunov techniques [21, 11, 26, 23]. It can control a class of uncertain nonlinear systems by robustly inverting the uncertain static nonlinearities.

Figure 4.2 depicts the control structure consisting of two control loops: the outer control loop (virtual control) and the inner control loop (High-Gain Lyapunov control). The control structure is similar to the standard successive loop closure. The outer loop is designed by assuming that the inner loop works perfectly ( $m_v = m$  in Figure 4.2). Then, the inner loop is designed to achieve the small error between  $m_v$  and  $m$  as quickly as possible regardless of the uncertainties so that the performance of the entire closed loop is close to the one without the inner loop. The design process is different from the successive loop closure in that the inner loop design explicitly depends on the outer loop control design.

The nonlinear control design consists of three major steps:

- Virtual control
- Reduced order observer, and
- High-Gain Lyapunov control,

which are described in detail in the following sections.



### 4.2.1 Step 1: Virtual Control

A continuous virtual controller ( $k(x)$ ) for the main system (4.1) is designed by ignoring the subsystem and regarding  $m$  as the control input. It is designed so that the closed-loop system

$$\dot{x} = f(x) + g(x)k(x) \quad (4.9)$$

is stable and achieves the desired performance. This step is performed to yield a slower time-scale closed loop (Figure 4.3) than a time-scales used in the Step 3.

Since this step ignores the existence of the subsystem and  $m$  is not the actual control input, the actual control needs to be determined so that  $m$  is “close” to  $k(x)$ . Before designing the actual control input, the internal states of the subsystem need to be estimated. This is described in the next step.

### 4.2.2 Step 2: Reduced Order Observer

Given the subsystem,

$$\dot{\eta}_o = F_{a_o}\eta_o + G_{a_o}(\bar{m}_s(x, u) + w) \quad (4.10)$$

$$m = H_{a_o}\eta_o, \quad (4.11)$$

an observer that achieves asymptotic decay of the state error in the presence of the lumped uncertainty ( $w$ ) needs to be designed because the state estimates are necessary in the next design step. The reduced order observer approach [50] achieves the asymptotic decay of the state error in the presence of the uncertainty without the information on the upper bounds of the uncertainty by transforming the system into a system where the uncertainty has no

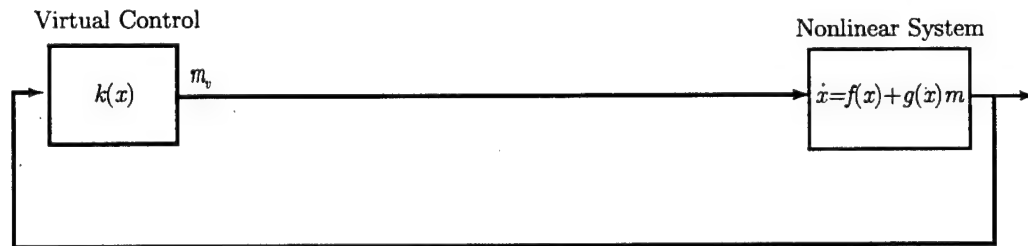


Figure 4.3: Virtual Closed Loop

direct effect on some of the states. The following describes the design process of a reduced order observer.

The conditions in Section 4.1.2 on the triple  $(F_{a_o}, G_{a_o}, H_{a_o})$  ensure that it can be linearly transformed into the following form [17, 18]:

$$F_a = \begin{bmatrix} F_{a_{11}} & F_{a_{12}} \\ F_{a_{21}} & F_{a_{22}} \end{bmatrix}, G_a = \begin{bmatrix} 0 \\ G_{a_2} \end{bmatrix}, H_a = [0 \ I], \quad (4.12)$$

The eigenvalues of  $F_{a_{11}}$  are the stable invariant zeros of  $(F_{a_o}, G_{a_o}, H_{a_o})$ .  $\eta_o$  is transformed into

$$\eta_o \rightarrow \eta = \begin{bmatrix} \eta_1 \\ m \end{bmatrix}.$$

In the new coordinates, the subsystem dynamics are expressed as follows:

$$\dot{\eta}_1 = F_{a_{11}}\eta_1 + F_{a_{12}}m \quad (4.13)$$

$$\dot{m} = F_{a_{21}}\eta_1 + F_{a_{22}}m + G_{a_2}(\bar{m}_s(x, u) + w). \quad (4.14)$$

The uncertainty ( $w$ ) is isolated from the part of the states ( $\eta_1$ ). It is assumed that the transformation from the original triple  $F_{a_o}, G_{a_o}, H_{a_o}$  to the triple  $F_a, G_a, H_a$  in (4.12) has been applied in the subsequent sections.

From the transformed system, it is straightforward to design a reduced order observer. A reduced order observer for  $\eta_1$  in (4.13) is constructed as follows:

$$\dot{\hat{\eta}}_1 = F_{a_{11}}\hat{\eta}_1 + F_{a_{12}}m \quad (4.15)$$

The error dynamics are

$$\dot{\tilde{\eta}}_1 = F_{a_{11}}\tilde{\eta}_1 \quad (4.16)$$

Since  $F_{a_{11}}$  is stable,

$$\tilde{\eta}_1 \rightarrow 0 \text{ as } t \rightarrow \infty \quad (4.17)$$

The estimate of  $\eta$  is

$$\hat{\eta} = \begin{bmatrix} \hat{\eta}_1 \\ m \end{bmatrix}.$$

The reduced order observer yields state estimate  $\hat{\eta}$  such that,

$$\tilde{\eta} = \eta - \hat{\eta} \rightarrow 0 \quad (t \rightarrow \infty). \quad (4.18)$$

Now that the internal states of the subsystem can be estimated by the observer in this step, the next step is to determine the actual control input ( $u$ ) so that the  $m$  is “close” to the virtual control ( $k(x)$ ) designed in the previous step.

### 4.2.3 Step 3: High-Gain Lyapunov Control

Lyapunov function techniques are employed in order to achieve “small” error between  $m$  and  $k(x)$ . The design process depends on the number of available inputs. In the following subsections, two cases are considered. First, the number of inputs is equal to the dimension of  $m$ , i.e.,  $n_u = n_m$ . In this case, each component of the error is controlled by the control inputs. In the second case, only one input is available while the dimension of  $m$  is more than one. In this case, only the norm of the error is controlled by the input. For more general cases ( $1 < n_u < n_m$ ), the combination of the two cases are applicable; that is, some components of the error are controlled but only the norm of the others are controlled.

#### Case 1: Number of inputs ( $n_u$ ) = Dimension of $m$ ( $n_m$ )

The inputs ( $u$ ) are determined from the following vector control Lyapunov function ( $V_s$ ) with  $w = 0, \eta = \hat{\eta}$ .

$$\dot{V}_s|_{w=0, \eta=\hat{\eta}} + 2 \operatorname{diag}(\alpha_s) V_s = -\operatorname{diag}(\kappa) s^2 \quad (4.19)$$

where a manifold ( $s$ ) is defined as the difference between the virtual control ( $k(x)$ ) and the aerodynamic moments ( $m$ ), i.e.,

$$s = m - k(x), \quad (4.20)$$

and  $V_s$  is a vector control Lyapunov function for  $s$ .

$$V_s = [V_{s_1} \cdots V_{s_{n_m}}]^T = \left[ \frac{1}{2} s_1^2 \cdots \frac{1}{2} s_{n_m}^2 \right]^T. \quad (4.21)$$

$s^2$  represents  $[s_1^2 \cdots s_{n_m}^2]^T$ , and  $\alpha_s = [\alpha_{s_1} \cdots \alpha_{s_{n_m}}]^T$  is the desired decay rate of  $s$ . The decay rate is defined as the largest  $\alpha_{s_i}$  such that

$$\lim_{t \rightarrow \infty} e^{\alpha_{s_i} t} |s_i(t)| = 0$$

holds for all trajectories of  $s_i(t)$ . This decay rate is selected normally five to ten times faster than the time-scale used in the virtual control design.  $\kappa = [\kappa_1 \cdots \kappa_{n_m}]^T$  is the vector of design parameters that determine the upper bound of  $|s_i|$ , ( $i = 1, \dots, n_m$ ). The bound can be made small by increasing  $\kappa_i$ , ( $i = 1, \dots, n_m$ ) as shown in Section 4.3.2. However, increasing  $\kappa$  generally leads to larger control efforts. Equation (4.19) can be rewritten as

$$\text{diag}(s)\dot{s}|_{w=0, \eta=\hat{\eta}} + \text{diag}(\alpha_s)s^2 = -\text{diag}(\kappa)s^2. \quad (4.22)$$

Since

$$\begin{aligned} \dot{s} &= \dot{m} - \dot{k}(x) \\ &= \dot{m} - \frac{\partial k(x)}{\partial x} \dot{x} \\ &= H_a(F_a \eta + G_a(\bar{m}_s(x, u) + w)) - \frac{\partial k(x)}{\partial x}(f(x) + g(x)m), \end{aligned} \quad (4.23)$$

and

$$\dot{s}|_{w=0, \eta=\hat{\eta}} = H_a(F_a \hat{\eta} + G_a \bar{m}_s(x, u)) - \frac{\partial k(x)}{\partial x}(f(x) + g(x)m), \quad (4.24)$$

then, (4.22) becomes

$$\text{diag}(s)[H_a(F_a \hat{\eta} + G_a \bar{m}_s(x, u)) - \frac{\partial k(x)}{\partial x}(f(x) + g(x)m)] + \text{diag}(\alpha_s)s^2 = -\text{diag}(\kappa)s^2. \quad (4.25)$$

Finally, the input ( $u$ ) can be determined by solving the following equation ( $n_m$  equations for  $n_u(=n_m)$  unknowns). Note that  $x$ ,  $m$  and  $\hat{\eta}$  are known. Thus, we have the relations:

$$\begin{aligned} \bar{m}_s(x, u) &= m_c(x, m, \hat{\eta}) - (H_a G_a)^{-1} \text{diag}(\kappa)s \\ &= m_c(x, m, \hat{\eta}) - [\tilde{\kappa}_1 \cdots \tilde{\kappa}_{n_m}]^T s, \end{aligned} \quad (4.26)$$

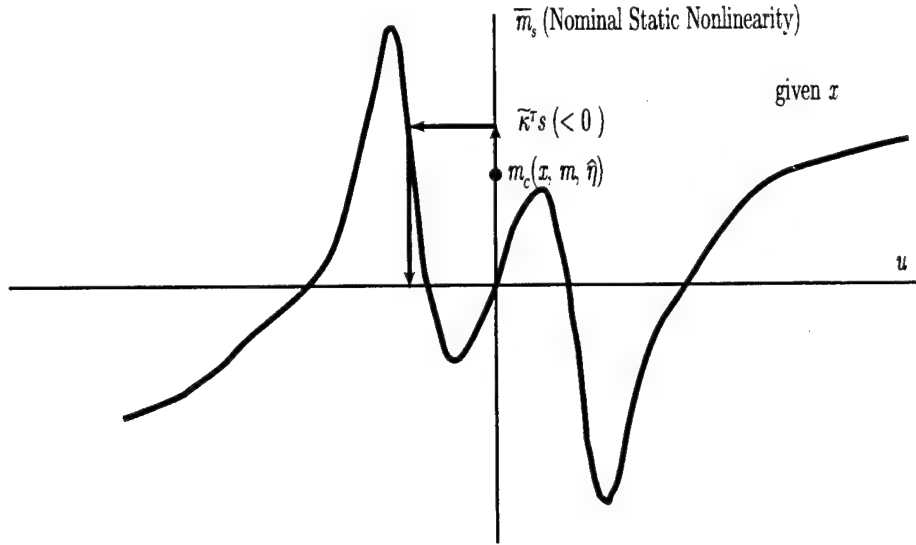


**Figure 4.4:** Inversion of nonlinearity (Determination of  $u$ )

where  $m_c(x, m, \hat{\eta})$  and  $\tilde{\kappa}_i, (i = 1, \dots, n_m)$  are defined as:

$$m_c(x, m, \hat{\eta}) = -(H_a G_a)^{-1} [H_a F_a \hat{\eta} - \frac{\partial k(x)}{\partial x} (f(x) + g(x)m) + \text{diag}(\alpha_s)s] \quad (4.27)$$

$$[\tilde{\kappa}_1 \dots \tilde{\kappa}_{n_m}]^T = (H_a G_a)^{-1} \text{diag}(\kappa) \quad (4.28)$$

The process of determining  $u$  from (4.26) requires an inversion of the static nonlinearities. Figure 4.4 depicts an example of how to determine a single control input ( $u$ ). In the figure, the curve represents the nominal static nonlinearity  $\bar{m}_s(x, u)$  given  $x$ . The input  $u$  is determined from a point where the curve intersects the horizontal line at  $(m_c(x, m, \hat{\eta}) - \tilde{\kappa}^T s)$ , which is known at any instance because  $x, m$  and  $\hat{\eta}$  are known. When multiple intersections exist, the minimum amount of the input will be chosen. Note that with the same  $m_c(x, m, \hat{\eta})$ , a different input results depending on the sign of  $\tilde{\kappa}^T s$ . In this way, the static nonlinearities are inverted to determine the inputs. In more general cases where multiple inputs need to be determined and every component of  $\bar{m}_s(x, u)$  is dependent on multiple inputs, it is difficult to find the inputs that satisfy (4.26). Some simplifications on the structure of  $\bar{m}_s(x, u)$  may be needed to make the process feasible in real-time implementation. One example of this process is to ignore the small effect of some inputs in the nominal static nonlinearities and regard the neglected effect as a part of uncertainties. As will be shown in Section 4.3, with the inputs selected as above, the stability of the system is guaranteed for

any positive design parameters ( $\kappa$ ). The performance and the control effort are traded-off with the design parameters in a systematic way in a sense that increasing the parameters leads to smaller bounds on the controlled variables and larger control effort, and vice versa.

### Case 2: Number of inputs ( $n_u$ ) = 1

When only a single input is available, the control input ( $u$ ) is determined from a scalar control Lyapunov function:

$$\dot{V}_s|_{w=0, \eta=\hat{\eta}} + 2\alpha_s V_s = -s^T K_s s, \quad (4.29)$$

where  $V_s$  is a scalar control Lyapunov function for  $s$ .

$$V_s = \frac{1}{2} s^T P_s s, P_s = P_s^T > 0, \quad (4.30)$$

$\alpha_s$  is a scalar decay rate of  $\|s\|_2$ , and  $K_s + K_s^T > 0$  is a design matrix that determines the upper bound of the  $\|s\|_2$ . As shown in Section 4.3.2, the bound can be made small by increasing  $\lambda_{\min}(K_s)$ . The left hand side of (4.29) is

$$\dot{V}_s|_{u=0, \eta=\hat{\eta}} + 2\alpha_s V_s = s^T P_s \dot{s}|_{w=0, \eta=\hat{\eta}} + \alpha_s s^T P_s s \quad (4.31)$$

$$= s^T P_s [H_a F_a \hat{\eta} + H_a G_a \bar{m}_s(x, u) - \frac{\partial k(x)}{\partial x} (f(x) + g(x)m) + \alpha_s s]. \quad (4.32)$$

Let

$$K_s = P_s \text{diag}(\kappa), \quad (4.33)$$

then (4.29) becomes

$$s^T P_s [H_a F_a \hat{\eta} + H_a G_a \bar{m}_s(x, u) - \frac{\partial k(x)}{\partial x} (f(x) + g(x)m) + \alpha_s s] = -s^T P_s \text{diag}(\kappa) s \quad (4.34)$$

Equation (4.34) depends only on  $u \in R^1$  only because  $x$ ,  $m$  and  $\hat{\eta}$  are known. From this relation,  $u$  is determined in a way similar to the multi-input case.

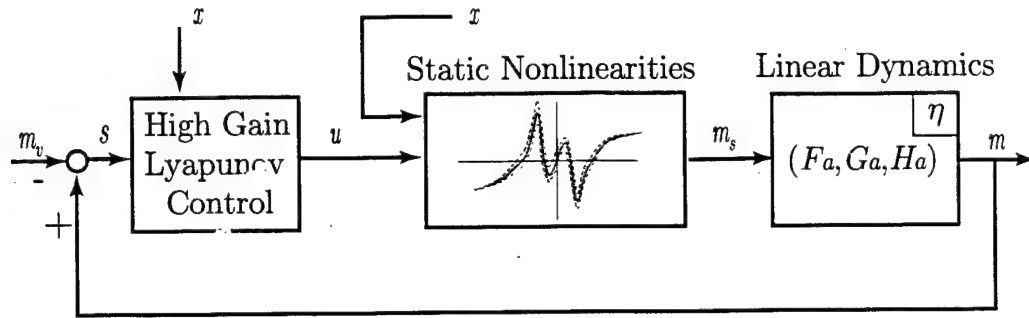


Figure 4.5: High-Gain Lyapunov Control

### Block Diagram of High-Gain Lyapunov Control Loop

A full dimensional Lyapunov function for the whole system in  $(x \in R^{n_x}, \eta \in R^{n_\eta})$  is not required to generate the control law. Only a low dimensional quadratic Lyapunov function for  $s \in R^{n_m}$  is used to generate the control law. This not only simplifies the control design process, but also makes the real-time implementation feasible. This feature is in contrast to other nonlinear control techniques such as Lyapunov Redesign and Backstepping. The block diagram is shown in Figure 4.5. High-Gain Lyapunov Control acts like a regulator for  $s$ .

#### 4.2.4 Discussion

The resulting controller/plant structure is depicted in Figure 4.2. The key element is that the inner loop achieves small error in the presence of the uncertainties. The inner loop control (High-Gain Lyapunov Control) takes the effect of the uncertainties on the stability into account in a selective way. When the size of the uncertainties is large, the control renders the effective gain of the controller “selectively high”. The control can adjust the control input to counteract the large uncertainties. The selective adjustment is made possible with the measurement of  $m$  that contains information of the uncertainties. The main idea behind the selective adjustment of the control gain according to the size of uncertainties comes from the nonlinear damping technique [26]. Essentially, the nonlinear approach in this chapter is an application of the nonlinear damping technique to a smaller dimensional error space. The idea comes from sliding mode control [23].

### 4.3 Proofs

It is shown that the steps described above yield a feasible controller by proving.

1.  $\tilde{\eta}$  is bounded,
2.  $u$  resulting from (4.26) or (4.34) renders  $s(t)$  bounded for any  $w$ ,
3.  $x$  is bounded, and
4.  $\eta$  is bounded.

#### 4.3.1 Boundedness of $\tilde{\eta}$

Since  $\tilde{\eta}_1 \rightarrow 0$ , and  $\tilde{\eta}$  is constructed as

$$\tilde{\eta} = \begin{bmatrix} \tilde{\eta}_1 \\ 0 \end{bmatrix},$$

$\tilde{\eta}$  is bounded.

$$\|\tilde{\eta}\|_2 \leq c_{\tilde{\eta}} \quad (4.35)$$

where  $c_{\tilde{\eta}}$  is the upper bound of  $\tilde{\eta}$ .

#### 4.3.2 Boundedness of $s$

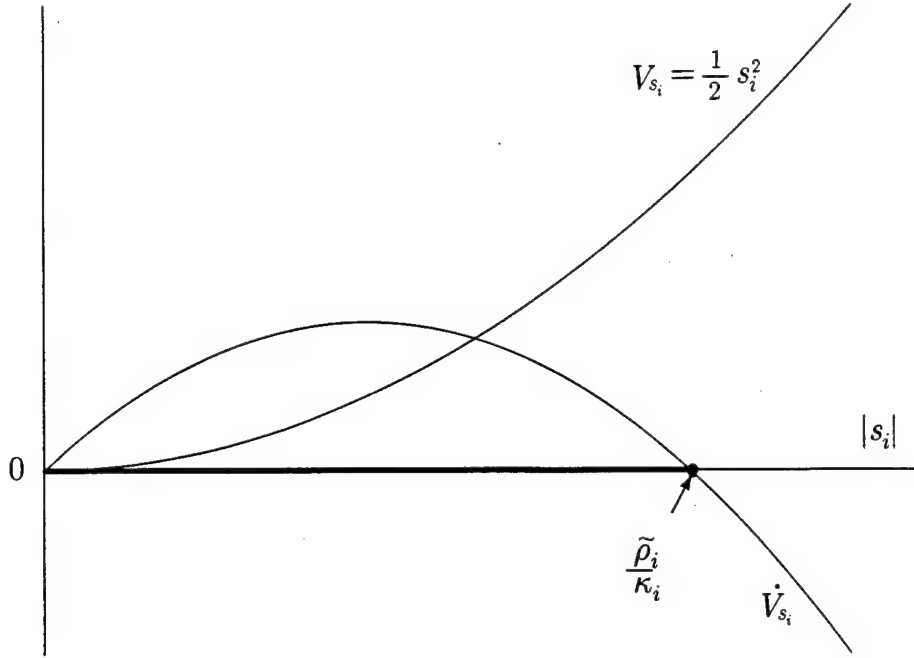
**Case 1: Number of inputs ( $n_u$ ) = Dimension of  $m$  ( $n_m$ )**

With  $u$  determined from (4.26), the vector control Lyapunov function ( $V_s$ ) with  $w \neq 0, \eta \neq \hat{\eta}$  is evaluated as follows:

$$\begin{aligned} \dot{V}_s + 2 \operatorname{diag}(\alpha_s) V_s &= \dot{V}_s|_{w=0, \eta=\hat{\eta}} + 2 \operatorname{diag}(\alpha_s) V_s + \operatorname{diag}(s)(H_a F_a \tilde{\eta} + H_a G_a w) \\ &= \operatorname{diag}(s)(H_a F_a \tilde{\eta} + H_a G_a w) - \operatorname{diag}(\kappa) s^2 \\ &= \operatorname{diag}(s) \tilde{w} - \operatorname{diag}(\kappa) s^2 \\ &\preceq \operatorname{diag}(|s|) \tilde{\rho} - \operatorname{diag}(\kappa) s^2 \end{aligned} \quad (4.36)$$

where  $\tilde{w} = H_a F_a \tilde{\eta} + H_a G_a w$  and  $\tilde{\rho}_i = |\tilde{w}_i|$ , ( $i = 1, \dots, n_m$ ).  $|s|$  is defined as  $[|s_1| \dots |s_2|]^T$ , and  $\preceq$  represents component-wise inequality. Note that  $\tilde{\rho}_i$ , ( $i = 1, \dots, n_m$ ) is unknown but



Figure 4.6: Boundedness of  $s$ 

bounded. The right-hand side of each component of (4.36) reduces to

$$\begin{aligned} -\kappa_i s_i^2 + \tilde{\rho}_i |s_i| &= -\kappa_i |s_i| \left( |s_i| - \frac{\tilde{\rho}_i}{\kappa_i} \right) \\ &= -\kappa_i \left( |s_i| - \frac{\tilde{\rho}_i}{2\kappa_i} \right)^2 + \frac{\tilde{\rho}_i^2}{4\kappa_i}, \quad (i = 1, \dots, n_m) \end{aligned} \quad (4.37)$$

In summary, it has been shown

$$\begin{cases} V_{s_i} = \frac{1}{2} s_i^2 & \geq 0 \\ \dot{V}_{s_i} + 2\alpha_{s_i} V_{s_i} & \leq -\kappa_i \left( |s_i| - \frac{\tilde{\rho}_i}{2\kappa_i} \right)^2 + \frac{\tilde{\rho}_i^2}{4\kappa_i} \end{cases} \quad (4.38)$$

Figure 4.6 depicts the situation when  $\alpha_s$  is zero. When  $|s_i(t)|$  is larger than  $\frac{\tilde{\rho}_i}{\kappa_i}$ ,  $\dot{V}_{s_i}$  becomes negative. This implies that  $V_{s_i}$  is decreasing as a function of time. Therefore,  $|s_i(t)|$  also decreases because  $V_{s_i}$  is a radially unbounded positive definite function of  $|s_i(t)|$ . In this way,  $|s_i(t)|$  is ultimately bounded above by  $\frac{\tilde{\rho}_i}{\kappa_i}$ . The bound can be made small by increasing  $\kappa_i$ , ( $i = 1, \dots, n_m$ ) without knowing the upper bound of the uncertainties ( $\tilde{\rho}_i$ ). However, increasing  $\kappa$  normally leads to larger control efforts. Therefore, it is concluded

that  $s_i, (i = 1, \dots, n_m)$  is ultimately bounded for any  $\kappa_i > 0, i.e.,$

$$|s_i(t)| \leq \frac{\tilde{\rho}_i}{\kappa_i}, (i = 1, \dots, n_m) \quad (4.39)$$

For all positive design parameter ( $\kappa$ ),  $s$  is bounded and  $\kappa$  determines the upper bound of  $s$ . If the estimates of the bounds ( $\tilde{\rho}$ ) of uncertainties are available, the upper bounds of  $s$  can be computed *a priori* from (4.39). The information can be used to estimate the upper bound of the controlled variables (the worst-case performance). Therefore,  $\kappa$  can be computed *a priori*, given the requirement of the worst-case performance. The upper bounds of uncertainties could be under-estimated in the High-Gain Lyapunov control because any positive  $\kappa$  can stabilize the system. This is in contrast to sliding mode control approach, where the upper bounds of uncertainties are required to be known or over-estimated in order to guarantee the stability of the closed loop system. The price paid in the High-Gain Lyapunov control for the additional stability protection is the possible excessive use of control effort.

Note that  $\tilde{\eta}$  is not required to converge to 0, but merely to be bounded. Also note that the 2-norm of  $s$  is bounded since each component of  $s$  is bounded.

$$\|s\|_2 \leq c_s(\kappa) \quad (4.40)$$

where  $c_s(\kappa)$  is the upper bound of  $\|s\|_2$ , which is a function of  $\kappa$ .

#### Case 2: Number of inputs ( $n_u$ ) = 1

With  $u$  determined from (4.34), the following inequality holds.

$$\begin{aligned} \dot{V}_s + 2\alpha_s V_s &= \dot{V}_s|_{w=0, \eta=\tilde{\eta}} + 2\alpha_s V_s + s^T P_s H_a (F_a \tilde{\eta} + G_a w) \\ &= s^T P_s H_a F_a \tilde{\eta} + s^T P_s H_a G_a w - s^T K_s s \\ &\leq (\|P_s H_a F_a\|_2 c_{\tilde{\eta}} + \|P_s H_a G_a\|_2 \rho) \|s\|_2 - s^T K_s s \\ &\leq c_{\rho, \tilde{\eta}} \|s\|_2 - \lambda_{\min}(K_s) \|s\|_2^2 \\ &\leq -\lambda_{\min}(K_s) \left( \|s\|_2 - \frac{c_{\rho, \tilde{\eta}}}{2\lambda_{\min}(K_s)} \right)^2 + \frac{c_{\rho, \tilde{\eta}}^2}{4\lambda_{\min}(K_s)} \end{aligned} \quad (4.41)$$

where

$$c_{\rho, \tilde{\eta}} = \|P_s H_a F_a\|_2 c_{\tilde{\eta}} + \|P_s H_a G_a\|_2 \rho. \quad (4.42)$$

Equation (4.41) shows that  $s$  is bounded and its bound can be made small by increasing  $\lambda_{\min}(K_s)$  regardless of  $w$  just as in the previous multi-input case. Therefore, it follows

$$\|s\|_2 \leq c_s(K_s), \quad (4.43)$$

where  $c_s(K_s)$  is the upper bound of  $\|s\|_2$ , which is a function of  $K_s$ .

### 4.3.3 Boundedness of $x$

Let  $V_x$  be a Lyapunov function for the rigid body states  $(x)$ . Since the main system (4.1) closed with the virtual control  $(k(x))$  is (for simplicity, exponentially) stable, the following inequalities hold from the Converse Lyapunov Theorem [27].

$$c_1 \|x\|_2^2 \leq V_x(x) \leq c_2 \|x\|_2^2 \quad (4.44)$$

$$\dot{V}_x(x) = \frac{\partial V_x(x)}{\partial x} (f(x) + g(x)k(x)) \leq -c_3 \|x\|_2^2 \quad (4.45)$$

$$\left\| \frac{\partial V_x(x)}{\partial x} \right\|_2 \leq c_4 \|x\|_2 \quad (4.46)$$

for some positive constants  $c_i, (i = 1, \dots, 4)$ . With the use of the same Lyapunov function  $V_x(x)$  for the system with actual  $m$  not with the virtual control  $(k(x))$ ,  $\dot{V}_x(x)$  is evaluated as follows:

$$\begin{aligned} \dot{V}_x(x) &= \frac{\partial V_x}{\partial x} (f(x) + g(x)m) \\ &= \frac{\partial V_x}{\partial x} (f(x) + g(x)(k(x) + s)) \\ &\leq -c_3 \|x\|_2^2 + \frac{\partial V_x}{\partial x} g(x)s \\ &\leq -c_3 \|x\|_2^2 + c_4 \|x\|_2 \|g(x)\|_2 \|s\|_2. \end{aligned} \quad (4.47)$$

From the assumptions in Section 4.1.2,  $g(x)$  is affinely bounded.

$$\|g(x)\|_2 \leq c_{g1} \|x\|_2 + c_{g2}, \quad c_{g_i} \geq 0 \quad (i = 1, 2) \quad (4.48)$$

Therefore,

$$\begin{aligned}\dot{V}_x(x) &\leq -(c_3 - c_4 c_{g1} c_s) \|x\|_2^2 + c_4 c_{g2} c_s \|x\|_2 \\ &= -c' \left( \|x\|_2 - \frac{c_4 c_{g2} c_s}{2c'} \right)^2 + \frac{(c_4 c_{g2} c_s)^2}{4c'}\end{aligned}\quad (4.49)$$

where

$$c' = c_3 - c_4 c_{g1} c_s \quad (4.50)$$

From the above inequality, if we can show that  $c' > 0$ , it follows that  $x$  is also bounded. Note  $c' > 0$  is always true if  $g(x)$  is norm-bounded, because  $c_{g1} = 0$  in this case and  $c' = c_3 > 0$ . Also note that the bound on  $x$  can be made small by increasing  $\kappa$  or  $K_s$  because increased gain leads to smaller ultimate bound ( $c_s$ ) of  $s$ . Thus, it can be concluded that the bound on  $x$  is also controlled by  $\kappa$  or  $K_s$ .

#### 4.3.4 Boundedness of $\eta$

Since  $s$  and  $x$  are bounded, and  $k(x)$  is continuous,  $m(= k(x) + s)$  is also bounded. Therefore, it can be concluded from (4.13) that  $\eta_1$  is bounded, since  $F_{a11}$  is stable and  $m$  is bounded. Consequently, all the internal states ( $\eta$ ) of the aerodynamic system ( $F_a, G_a, H_a$ ) are bounded.

### 4.4 Summary

In this chapter, a nonlinear control approach is developed that stabilizes a class of uncertain nonlinear systems in multiple time scales by robustly inverting uncertain static nonlinearities. It is applicable to nonlinear systems with large uncertainties in the input subsystem. It consists of a few simple steps that allow a two time-scale design. It does not require the upper bound of uncertainties. That is, it is not necessary to know precisely the region where the actual nonlinearities reside. However, if the estimates of the bounds are available, the information can be used, *i.e.*, the control performance can be evaluated *a priori*. The upper bounds of uncertainties can be under-estimated, because under-estimated values do not induce instability of the system. This is in contrast to existing approaches such as sliding mode control, with which the upper bounds of uncertainties are required known or

over-estimated in order to guarantee the stability of the closed loop system. Only a low dimensional quadratic Lyapunov function is used to generate the control law. This simplifies the control design process. Furthermore, it allows trade-off between the performance and the control efforts by simply increasing or decreasing the design parameters ( $\kappa$  or  $K_s$ ) while preserving the stability.

## Chapter 5

# Control Results

The nonlinear control approach developed in the previous chapter is applied to the FTB system and the utility of the approach is demonstrated. Specifically, three configurations are chosen for the purpose of demonstration in simulations and experiments. The first case is 1-DOF roll angle set-point tracking. The 1-DOF system is linear except in the highly nonlinear static roll moment characteristics. Both simulation and experimental results are provided.

The second case is stabilization of the 2-DOF system. Simulations are conducted under the assumption of the perfect active torque cancellation. This assumption makes the configuration closer to actual flight conditions, because the gravitational torque and the large inertia of the supporting system are perfectly eliminated.

Finally, experimental results in set-point tracking of the 2-DOF system are provided and the performance and the control efforts are compared with a result using a conventional control approach (Bang-Bang control).

In all cases, the nonlinear control approach can stabilize the FTB system and/or achieve the set points with small levels of blowing. However, the performance with the small usage of air is degraded compared to a conventional Bang-Bang control, which is a special case for the nonlinear control in the sense that the nonlinear control structure becomes the Bang-Bang control with large control parameters. Therefore, it can be said that the nonlinear control approach allows the trade-off between the performance and the control effort by tuning design parameters.

## 5.1 Application to the FTB system

### 5.1.1 Control Objective

The nonlinear control design is applied to the FTB system. The control objectives include

- Determine  $u=C_\mu$  or  $u=[C_\mu \delta_f]$  to stabilize robustly or perform set-point tracking of the uncertain system given measurement of  $y$ , and
- Control should minimize the amount of blowing to exploit the effectiveness of FTB.

### 5.1.2 System Description

From Section 3.6, the FTB system is expressed in the following form:

$$\dot{x} = f(x) + g(x)m \quad (5.1)$$

$$\dot{m} = F_a m + G_a(\bar{m}_s(x, u) + w) \quad (5.2)$$

where  $x \in R^4$ ,  $m \in R^2$ ,  $m_s \in R^2$ ,  $u \in R^1$  or  $u \in R^2$ . The measured output vector is

$$y = [q^T \dot{q}^T \ddot{q}^T]^T = [\phi \gamma \dot{\phi} \dot{\gamma} \ddot{\phi} \ddot{\gamma}]^T. \quad (5.3)$$

In order to be able to apply the nonlinear control design developed in Chapter 4 to the FTB system, it is required to know  $m$  in real time. For the FTB system,  $m$  can be computed from equation (3.8) using the angular accelerations ( $\ddot{\phi}$  and  $\ddot{\gamma}$ ). Therefore, the output is equivalent to

$$y = [x^T m^T]^T \quad (5.4)$$

The noise in the accelerations directly results in an error in  $m$ . Therefore, both accelerations are filtered with analog prefilters. The error in  $m$  can be regarded as another source of uncertainties.

The uncertainty  $w$  is assumed to satisfy the following:

$$|w_i| \leq \rho_i \text{ (unknown)}, (i = 1, 2). \quad (5.5)$$

The function  $g(x)$  in (5.1) is norm bounded, i.e.,

$$\|g(x)\|_2 \leq c_{g2}, \quad (5.6)$$

because

$$g(x) = \begin{bmatrix} 0 \\ H(q)^{-1} \end{bmatrix} \quad (5.7)$$

from (3.9), and  $H(q)$  satisfies [15]

$$\underline{\lambda}_{min} I \leq H(q) \leq \bar{\lambda}_{max} I \quad (5.8)$$

for all possible  $q$ . Therefore,  $c'$  in (4.50) is always positive because  $c_{g1} = 0$  in this case.

$$c' = c_3 - c_4 c_{g1} c_s = c_3 > 0 \quad (5.9)$$

Since two independent first order lags for both aerodynamic moments are considered, all the conditions (Section 4.1.2) on the triple  $F_{a_o}, G_{a_o}, H_{a_o}$  are satisfied. Note that full state information is also available in this case, so the reduced order observer (Step 2) is not necessary.

### 5.1.3 Virtual Control

There are multiple possible approaches to design the continuous virtual control ( $k(x)$ ) for the rigid body dynamics, such as Feedback Linearization [42], Passivity-based approach [15] and Proportional and Derivatives (Integral) (PID) control [2]. A PD (PID) controller is employed here, since it is typically more robust than the other approaches because it does not require exact system parameters. As can be seen in the design of the virtual control in Section 5.3.1 and Section 5.3.2, the performance is acceptable. Also, it has the advantage of simplicity of implementation. For example,  $\frac{\partial k(x)}{\partial x}$  needs to be evaluated in the design process where this term simply becomes the gain matrices when  $k(x)$  is PD (PID) control.

### 5.1.4 High-Gain Lyapunov Control

As shown in Section 4.2.3, separate cases with two and one actuator(s) are considered.

#### Two inputs: $C_\mu$ and $\delta_f$

As a result of the simplifications on the construction of the nominal static moment characteristics in Section 3.5, (4.26) reduces to two equations in two unknowns ( $C_\mu$  and  $\delta_f$ ).



These are:

$$\bar{m}_{s_1}(x, C_\mu) + k_{\delta_f} \delta_f = m_{c_1}(x, m) - \tilde{\kappa}_1^T s \quad (5.10)$$

$$\bar{m}_{s_2}(x, C_\mu) = m_{c_2}(x, m) - \tilde{\kappa}_2^T s \quad (5.11)$$

where  $m_c(x, m)$  and  $\tilde{\kappa}_i$ , ( $i = 1, 2$ ) are defined as:

$$m_c(x, m) = -G_a^{-1} [F_a m - \frac{\partial k(x)}{\partial x} (f(x) + g(x)m) + \text{diag}(\alpha_s)s] \quad (5.12)$$

$$[\tilde{\kappa}_1 \ \tilde{\kappa}_2]^T = G_a^{-1} \text{diag}(\kappa). \quad (5.13)$$

In this simplified form, no iterations are required to solve for the two control inputs ( $C_\mu$  and  $\delta_f$ ) from the two nonlinear characteristics, because  $C_\mu$  can be determined solely from (5.11).

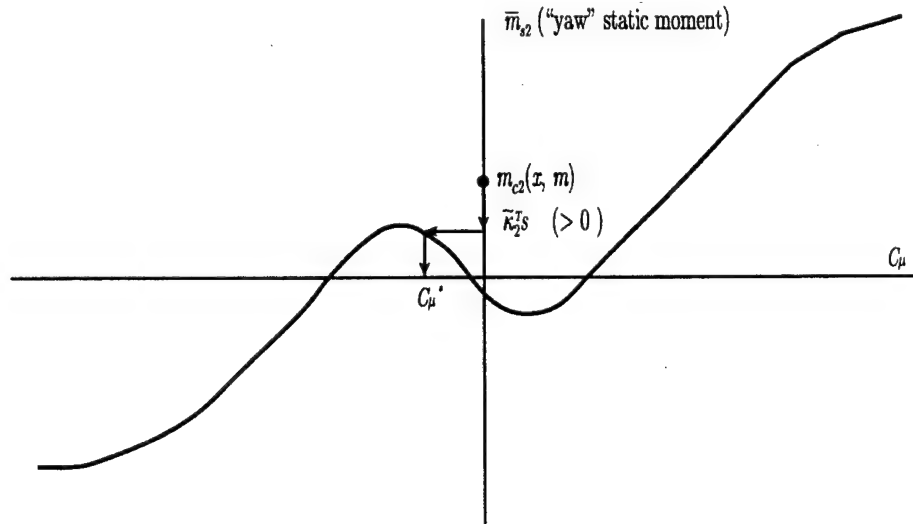


**Figure 5.1:** Inversion of a nonlinear static moment (Determination of  $C_\mu$ )

The schematic diagram that shows how to determine  $C_\mu$  is given in Figure 5.1. Given  $x$ , the nominal “yaw” moment curve ( $\bar{m}_{s_2}(x, C_\mu)$ ) is fixed.  $C_\mu$  is determined by finding values of  $\bar{m}_s(x, C_\mu)$  equal to  $(m_{c_2}(x, m) - \tilde{\kappa}_2^T s)$ . Note that with the same  $m_{c_2}(x, m)$ , a different  $C_\mu$  results depending on the sign of  $\tilde{\kappa}_2^T s$ , as explained in Section 4.2.3. In this way, the nominal “yaw” moment curve is inverted to find  $C_\mu$ . When multiple solutions exist, the minimum  $C_\mu$  will be chosen. When  $\kappa$  is so large that no  $C_\mu$  exists that solves (5.11), the extreme

values of  $C_\mu$  will be used because the moments generated by the values are sign-definite (less uncertain in larger blowing region). This scheme renders the control structure Bang-Bang control. Once  $C_\mu$  is determined,  $\delta_f$  is computed from (5.10).

### One input: $C_\mu$ only

Equation (4.34) for this case is as follows:

$$s^T P_s [F_a m + G_a \bar{m}_s(x, C_\mu) - \frac{\partial k(x)}{\partial x} (f(x) + g(x)m) + \alpha_s s] = -s^T P_s \text{diag}(\kappa_1, \kappa_2) s \quad (5.14)$$

which is a function of  $C_\mu$  only, because  $x$  and  $m$  are known. From this function,  $C_\mu$  is determined also by inverting the nonlinear function (5.14). Although the nonlinear function is more complicated than the multi-input case, only the single unknown ( $C_\mu$ ) is searched. Therefore, the process of finding  $C_\mu$  is no harder than the multi-input case.

## 5.2 1-DOF ( $\phi$ )

### 5.2.1 System Description

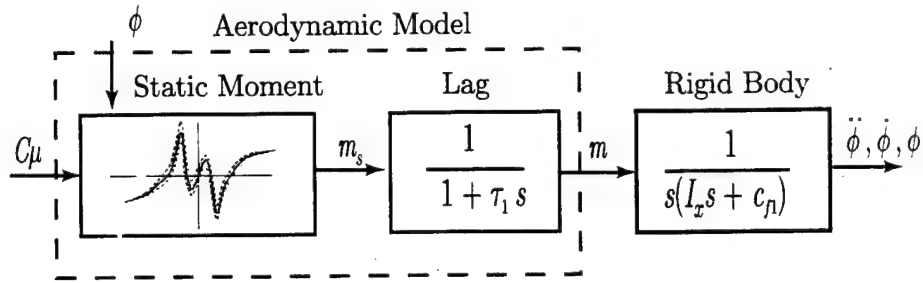
In order to demonstrate the effectiveness of the control approach in a simple setting, 1-DOF roll( $\phi$ ) motion is used as an example. In this case, the nonlinearity lies only in the static roll moment characteristic. Roll motion is chosen over “yaw” motion, because, as shown in the figures in Chapter 3, the nonlinearities in the roll moment characteristics are stronger than those of “yaw” moment in the sense that the slopes are steeper and the sign change of the slopes is more frequent. Furthermore, the active torque cancellation is not necessary because there is no gravitational moment about the roll axis, and this axis has a much smaller moment of inertia.

When the FTB system is confined to the 1-DOF roll axis at  $\gamma = 0^\circ$ , the rigid body dynamics reduce to a simple Linear Time-Invariant (LTI) system. The system is described as follows:

$$\dot{x} = F_r x + G_r m, \quad (5.15)$$

$$\dot{m} = F_a m + G_a m_s(x, C_\mu), \quad (5.16)$$

$$x = [\phi \ \dot{\phi}]^T$$

Figure 5.2: Block Diagram of the 1-DOF system ( $\phi$ )

$$y = [\phi \ \dot{\phi} \ \ddot{\phi}]^T \rightarrow [x \ m]^T$$

$$F_r = \begin{bmatrix} 0 & 1 \\ 0 & -\frac{c_\phi}{I_x} \end{bmatrix}, G_r = \begin{bmatrix} 0 \\ \frac{1}{I_x} \end{bmatrix}, F_a = -\frac{1}{\tau_1}, G_a = \frac{1}{\tau_1},$$

A block diagram representation of the dynamics ((5.15), (5.16)) is given in Figure 5.2.

### 5.2.2 Set-point Tracking

A common approach to achieve set point tracking is to add an integrator for zero steady state error. Thus, the system is augmented with an integrator as follows:

$$\phi_{err} = \phi_{cmd} - \phi \quad (5.17)$$

$$\dot{x} = F_r x + G_r m. \quad (5.18)$$

The extended state vector is

$$x_e = \left[ \int \phi_{err} dt \ \phi \ \dot{\phi} \right]^T. \quad (5.19)$$

### Virtual Control

Since the rigid body dynamics form a simple LTI system, the virtual control can be designed using any linear control technique. Pole assignment is used here because it is one of the simplest techniques to design a linear controller for an LTI system when all the states are available. The bandwidth of the closed loop system is set about 10 rad/s so that the closed loop system has a time constant of approximately 0.1 seconds. The 10 (rad/s) bandwidth of the closed loop is about 1/10 of the bandwidth of the  $C_\mu$  servo control (Refer to Section 2.4). Therefore, as a rule of thumb, the dynamics of the  $C_\mu$  servo control can be neglected

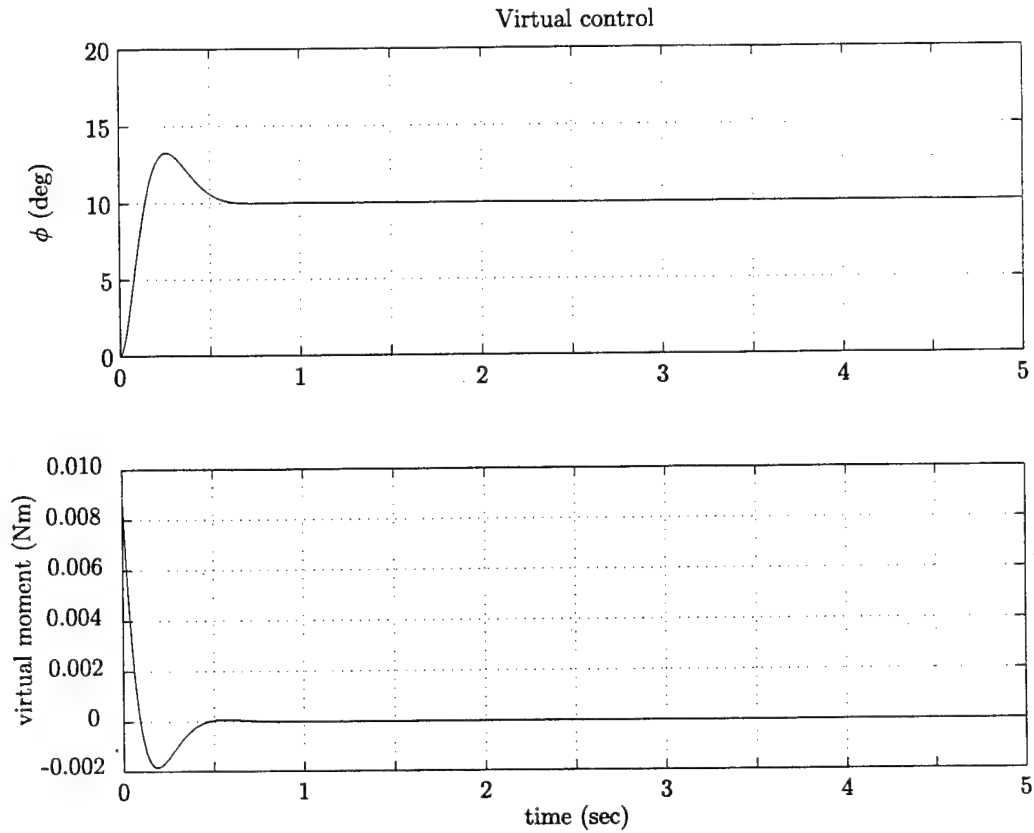


Figure 5.3: Virtual control (1-DOF set-point tracking)

in designing an outer loop control. The damping of the dominant poles is set around 0.7 to strike a balance between the overshoot and the rise time. When the poles of the closed loop are assigned at  $[-8.5 \pm 8.5j, -8.5]$ , then the linear feedback gain is obtained as follows:

$$k(x_e) = K_{re}x_e = -[K_i \ K_p \ K_d]x_e,$$

where

$$K_p = 0.0509, K_i = 0.2162, K_d = 0.0029.$$

With this gain matrix, the virtual closed loop is stable and its response to the step input is shown in Figure 5.3. The response of  $\phi$  is as desired. The maximum virtual moment is about 0.008 (Nm). This is small enough to be achieved with  $C_\mu$ .

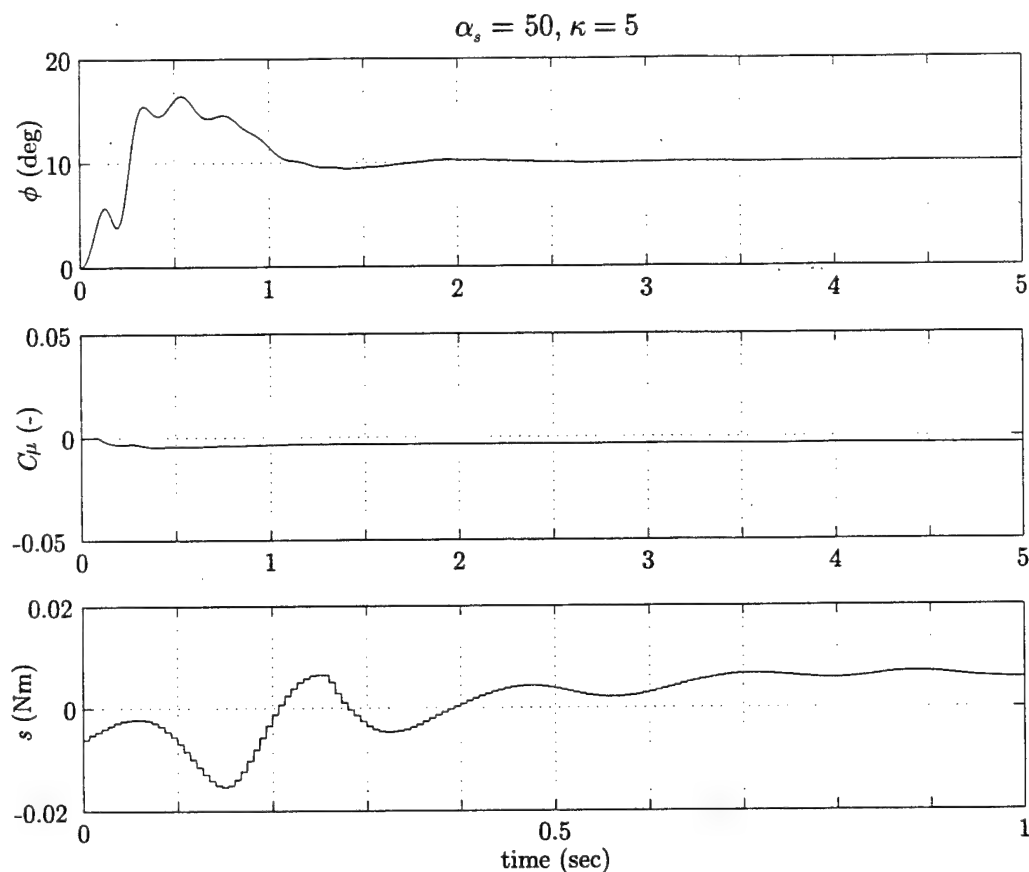


Figure 5.4: 1-DOF ( $\phi$ ) set-point tracking (Simulation),  $\kappa = 5$

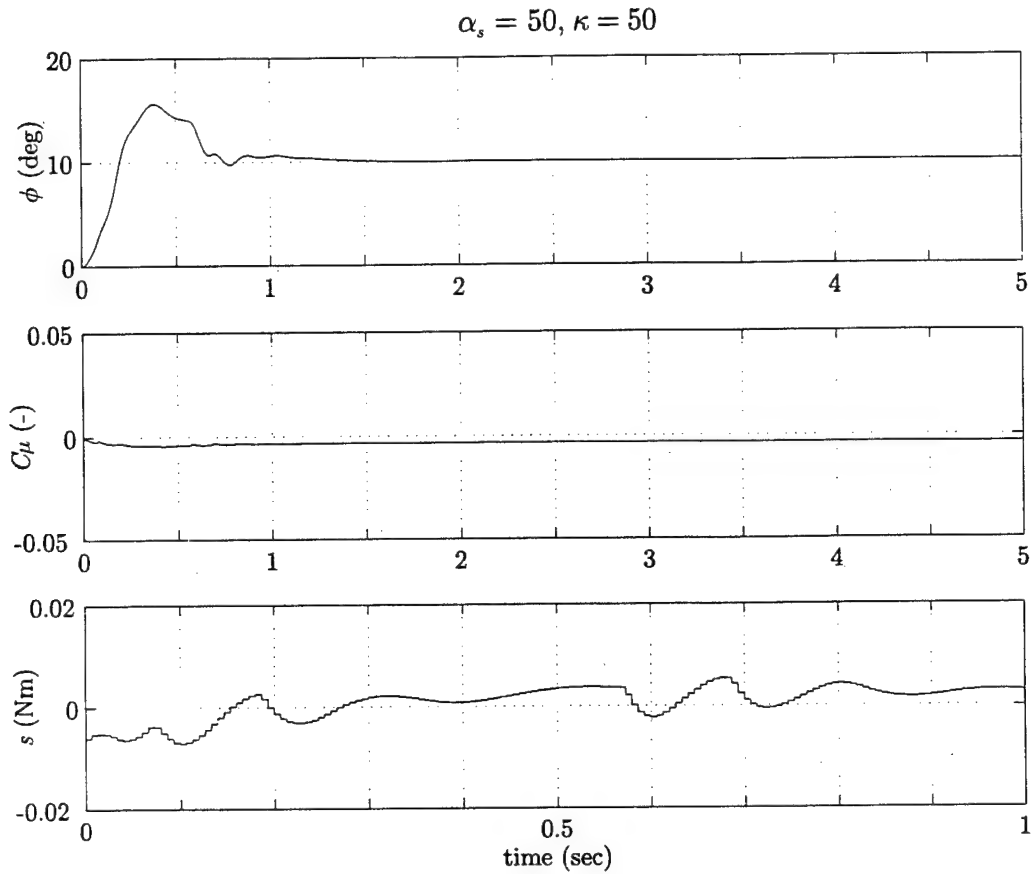
### High-Gain Lyapunov Control

The decay rate of  $s$  is set at  $\alpha_s = 50.0$  so that this becomes 5 times faster than the bandwidth of the virtual closed loop of the rigid body dynamics.

### Simulation Results

In simulations, a constant bias in  $C_\mu$  is used as a source of error ( $\delta C_\mu = 0.0005$ ). This bias error is chosen to test the robustness of the control approach because a small bias leads to large errors ( $\delta m_s = 0.016 \approx 70\%$  of full range) in the static roll moment due to the steep slope in the characteristics.

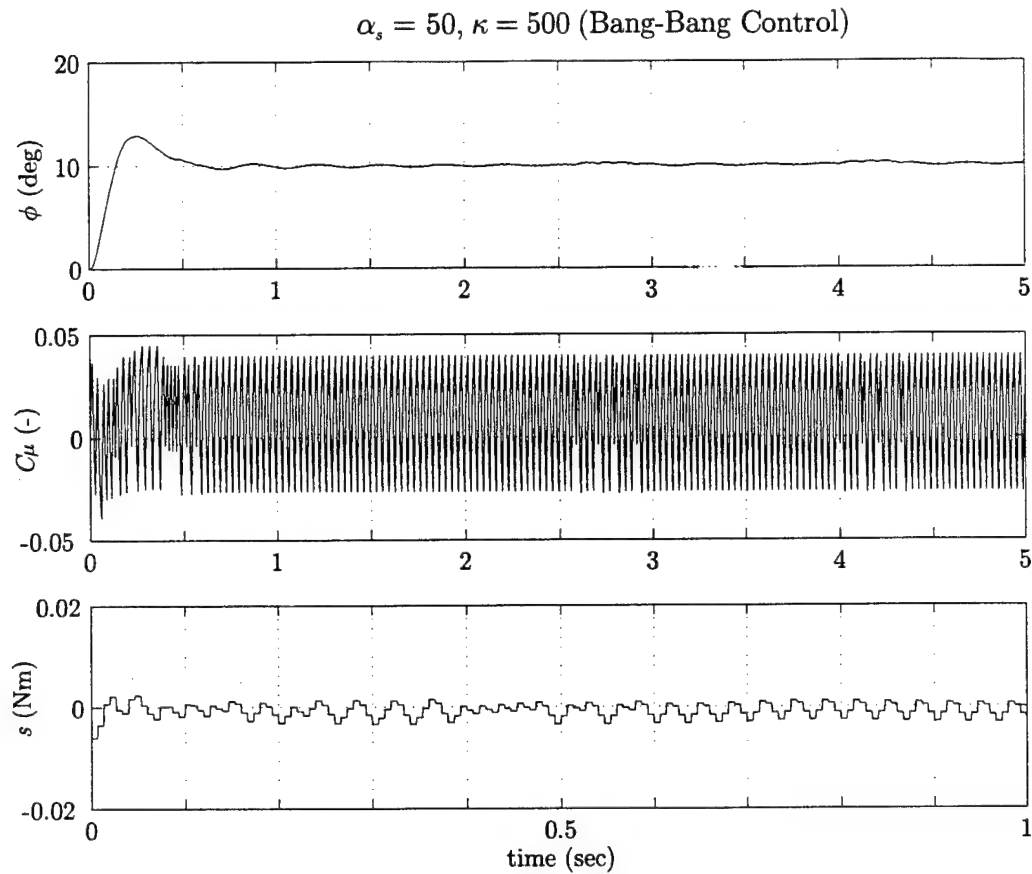
Simulation results are shown in Figure 5.4, Figure 5.5 and Figure 5.6 for different values of  $\kappa$ . Table 5.1 shows the summary of the simulation results. Figure 5.4 shows a result

Figure 5.5: 1-DOF ( $\phi$ ) set-point tracking (Simulation),  $\kappa = 50$ 

$\kappa$	$s$	$\phi$ peak	$\Delta\phi$	$C_\mu$
5	0.0112	16.44°	0.1380°	0.0036
50	0.0062	15.63°	0.0168°	0.0037
500	0.0042	12.92°	0.2022°	0.0208

Table 5.1: Summary of 1-DOF simulation results

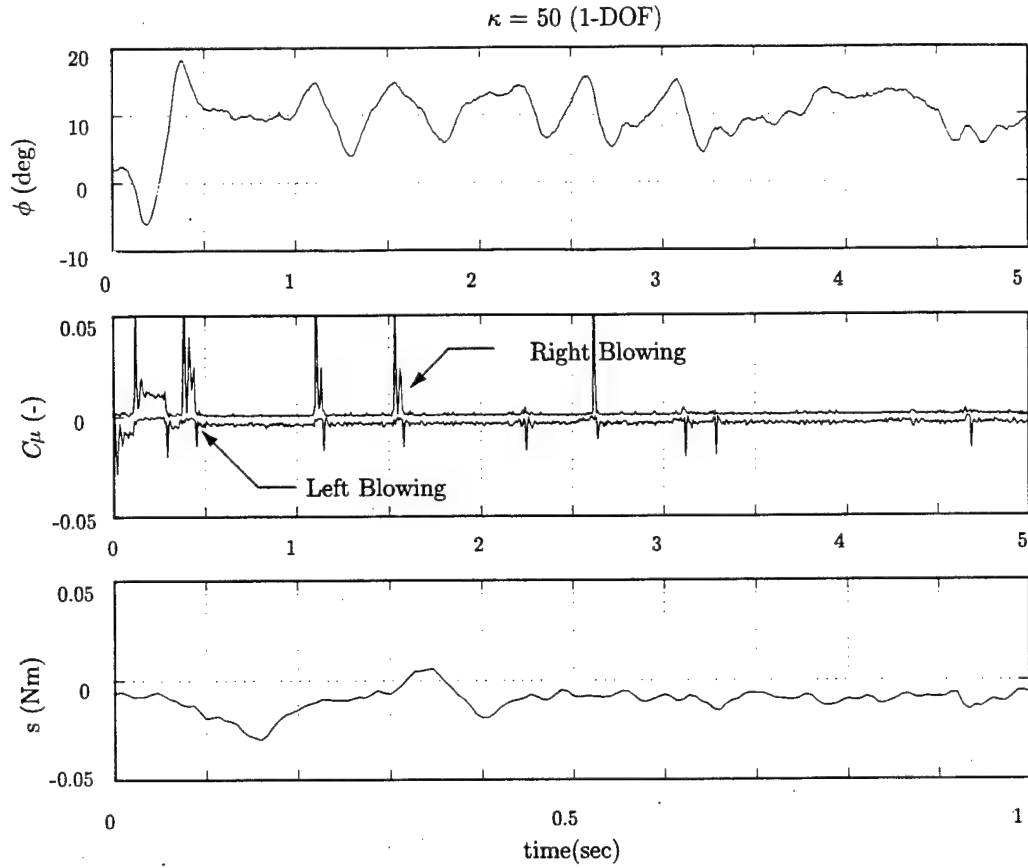
with a smaller  $\kappa$  ( $=5$ ).  $\phi$  achieves the commanded value ( $10^\circ$ ) with very small  $C_\mu$ . The average  $C_\mu$  is 0.0036 in  $t \in [0 \ 5]$  in the figure. However, the response is not as smooth as in Figure 5.5 where a larger  $\kappa$  ( $=50$ ) is used and the average  $C_\mu$  is 0.0037. Also, the bound of  $s$  ( $\Delta s = 0.0112$ ) in Figure 5.4 is larger than that ( $\Delta s = 0.0062$ ) in Figure 5.5. The overall response of  $\phi$  in Figure 5.5 is smooth and is comparable to that of the virtual control response (See Figure 5.3). In Figure 5.6, a result with a very large  $\kappa$  ( $=500$ ) is presented. With the large  $\kappa$ , the control structure becomes Bang-Bang control as described in Section



**Figure 5.6:** 1-DOF ( $\phi$ ) set-point tracking (Simulation),  $\kappa = 500$  (Bang-Bang)

5.1.4. (Bang-Bang control is a conventional approach to the control of nonlinear uncertain systems [45].) The set point is achieved without steady state error, the response is very smooth, and  $s$  is contained in a small bound ( $\Delta s = 0.0042$ ), but the level of  $C_\mu$  is very large compared to the previous two results. In this case, the average  $C_\mu$  is 0.0208.

As  $\kappa$  is increased, the bound of  $s$  is decreased and the overall response becomes closer to that of the virtual control. However, increasing  $\kappa$  leads to a larger control effort as explained in Section 5.1.4. In this specific case, increasing  $\kappa$  from 5 to 50 does not result in a large increase in  $C_\mu$ , because the roll moment characteristics exhibit strong nonlinearities that can generate large roll moment with a small  $C_\mu$ . (For example, see Figure 3.1.) The larger  $\Delta\phi$  at  $\kappa = 500$  is due to the  $C_\mu$  servo system limitation. The command  $C_\mu$  changes so rapidly that the  $C_\mu$  servo does not follow the command perfectly.

Figure 5.7: 1-DOF ( $\phi$ ) set-point tracking (Experiment),  $\kappa = 50$ 

$\kappa$	$s$	$\phi$ peak	$\Delta\phi$	$C_\mu$
50	0.0179	18.38°	5.681°	0.0059
500	0.0147	14.37°	4.343°	0.0546

Table 5.2: Summary of 1-DOF experimental results

### Experimental Results

The nonlinear controller is implemented in a C program on a PC. Equation (5.11) is solved for  $C_\mu$  at every time step (150Hz). Figure 5.7 and Figure 5.8 present experimental results, and the summary of the experimental results is shown in Table 5.2.

Figure 5.7 shows a result with  $\kappa = 50$ .  $\phi$  initially moves in the opposite direction and then achieves the commanded value (10°) without steady state bias with small  $C_\mu$  both in transient and steady state. (The maximum  $|C_\mu|$  in the transient is about 0.01 and the



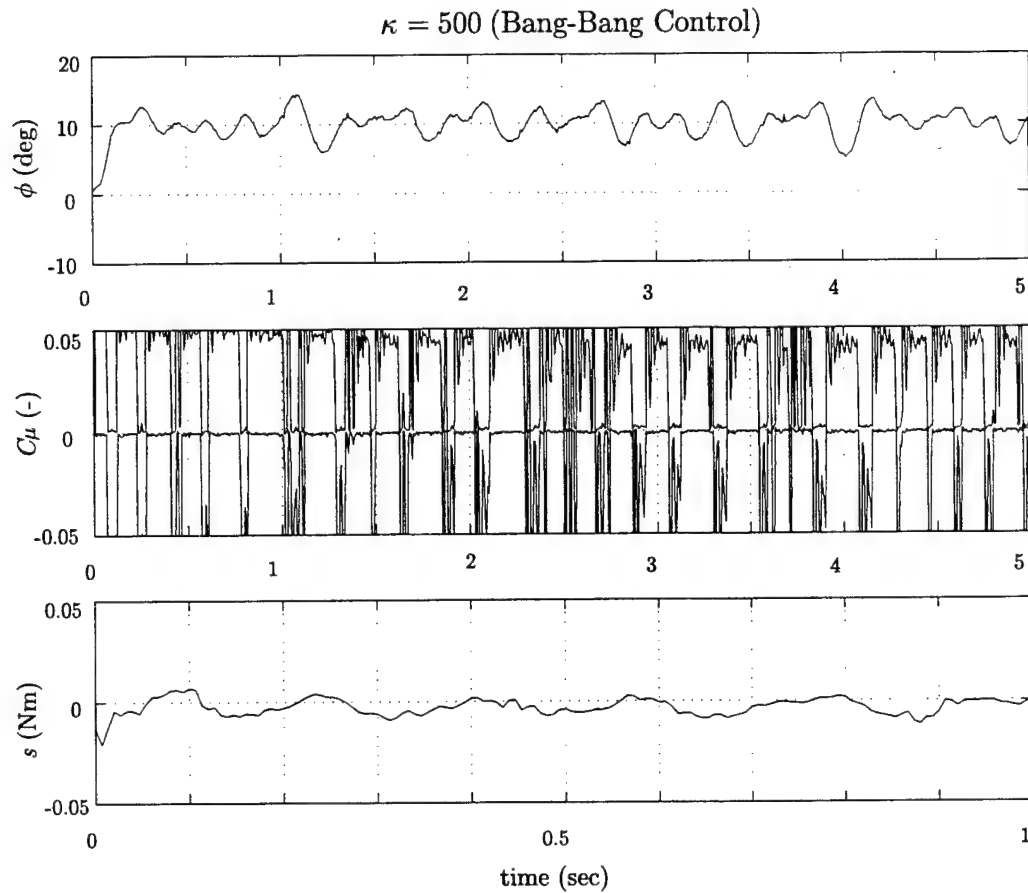


Figure 5.8: 1-DOF ( $\phi$ ) set-point tracking (Experiment),  $\kappa = 500$  (Bang-Bang)

average value in the steady state is about 0.006.) Also,  $s$  is contained in a small bound ( $\Delta s = 0.0179$ ). The spikes in  $C_\mu$  do not result from the commanded  $C_\mu$  but are an artifact of the valve hardware. The bound of  $\phi$  ( $\Delta\phi = 5.68^\circ$ ) at the steady state (after about 1 second) is larger than the bound ( $\Delta\phi = 4.34^\circ$ ) in Figure 5.8 which shows a result with  $\kappa = 500$  (Bang-Bang control). The Bang-Bang control achieves the same set point without steady state error, and  $s$  is contained in a smaller bound ( $\Delta s = 0.0147$ ). However, the control effort ( $C_\mu$ ) with the Bang-Bang control is much larger ( $|C_\mu| = 0.05$ ). (The  $|C_\mu| = 0.05$  is used because the roll moment corresponding to the  $C_\mu = 0.05$  is positive for all  $\phi$  and  $C_\mu = -0.05$  generates negative roll moment for all  $\phi$ .)

By comparing the two experimental results, the same trend occurring in the simulation is observed. As  $\kappa$  becomes large, the bound of  $s$  decreases and the response of  $\phi$  becomes closer to that of the virtual control but the control effort becomes large. In this way, the

performance and the control efforts can be explicitly traded-off in practice by adjusting the design parameter  $\kappa$ .

### 5.2.3 Summary of 1-DOF cases

The nonlinear control approach has been applied to 1-DOF roll angle set-point tracking. The 1-DOF system is linear except in the highly nonlinear static roll moment characteristics. It has been shown that both simulations and experiments results have the same trend that increasing  $\kappa$  results in better performance and larger control effort ( $C_\mu$ ). This trend is predicted by the theory in Chapter 4. Therefore, the performance and the control effort can be traded-off by adjusting the design parameter ( $\kappa$ ). Also, when a very large  $\kappa$  is used, the control structure becomes a conventional Bang-Bang control and the performance of the conventional Bang-Bang control can be recovered as a special case. The results show that the nonlinear control approach can make use of FTB effectively.

## 5.3 2-DOF ( $\phi$ and $\gamma$ )

Results of stabilization with one input ( $C_\mu$ ) and set-point tracking with two inputs (blowing,  $C_\mu$  and flaperon,  $\delta_f$ ) are provided. In stabilization with one input, simulation results are provided assuming the active torque cancellation is perfect. (The active torque cancellation is described in Appendix B.) In set-point tracking with two inputs, experimental results are given with the active torque cancellation working.

### 5.3.1 Stabilization

Stabilization of the 2-DOF system with only  $C_\mu$  is discussed. In this case, while the dimension of  $m$  is two, the number of the inputs is one. Therefore, a scalar Lyapunov function ( $V_s = \frac{1}{2}s^T P_s s$ ) is used in High-Gain Lyapunov control (Refer to Section 4.2.3.). As noted above, since the active torque cancellation is assumed perfect,  $I_A = 0, m_g = m_m = 0$  are used in the system equations ((3.1), (3.2)). An open-loop response of the 2-DOF system under these conditions is shown in Figure 5.9. Obviously the open-loop system is unstable. In particular,  $\gamma$  diverges quickly.

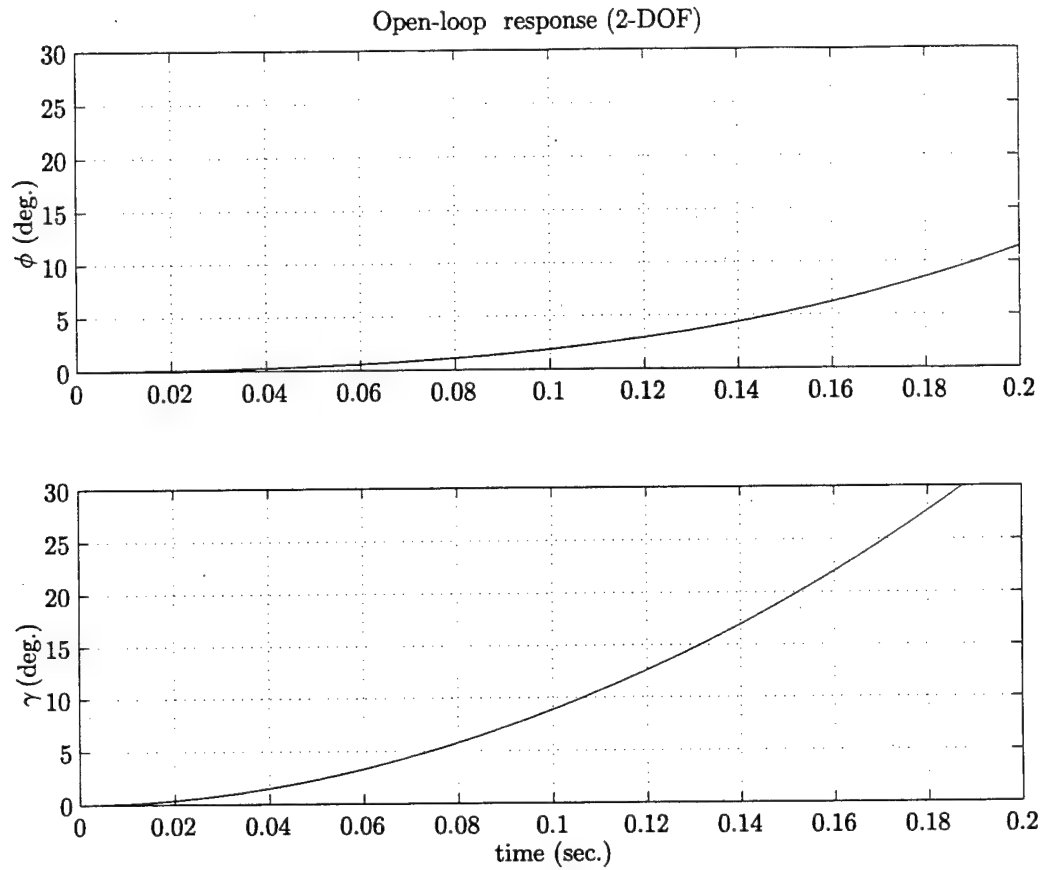


Figure 5.9: Open-loop response (2-DOF)

### Virtual Control

A PD controller in the following form is considered.

$$k(x) = -(K_p q + K_d \dot{q}) \quad (5.20)$$

where  $K_p + K_p^T > 0$ ,  $K_d + K_d^T > 0$ .

$K_p$  and  $K_d$  selection: Any  $K_p + K_p^T > 0$  and  $K_d + K_d^T > 0$  can stabilize the system, because the system is a rigid body [42]. However, the performance changes with the choice of the gains. Therefore, suitable choice of these gains is important. One approach is to optimize the performance of the PD controller using convex optimization. Since the constraints  $K_p + K_p^T > 0$ ,  $K_d + K_d^T > 0$  are Linear Matrix Inequalities (LMI) (therefore, convex), convex optimization techniques are applicable if the objectives are convex. Since it is impossible,

however, to handle the nonlinear dynamics directly, the optimization can be performed over a set of  $N$  linearized operating points. That is, the system can be approximated as a collection of linear systems:

$$\dot{x} = A_i x + B_i m_v, (i = 1, 2, \dots, N) \quad (5.21)$$

For this collection of linear systems, we consider a single Lyapunov function,

$$V = \frac{1}{2} x^T Q_x^{-1} x, \quad Q_x = Q_x^T > 0$$

After proper scaling, the condition number ( $\beta$ ) of  $Q_x$  is minimized, which represents the peaking factor. Peaking factor is defined as the ratio of the norm between the initial states and the farthest point of the trajectory from the origin. In other words, it gives a bound on how far any trajectory can wander relative to how far it was when it started, before converging back to the origin.

$$\begin{aligned} & \min \quad \beta \\ & \text{subject to} \quad Q_x(A_i - B_i K_x)^T + (A_i - B_i K_x)Q_x + 2\alpha_x Q_x < 0, (i = 1, 2, \dots, N) \\ & \quad K_x = [K_p \ K_d] \\ & \quad K_p + K_p^T > 0 \\ & \quad K_d + K_d^T > 0 \\ & \quad I < Q_x = Q_x^T < \beta I \\ & \quad \|m_v\|_2 < \mu, \forall \|x(0)\|_2 < 1 \end{aligned}$$

This is not an LMI in  $Q_x$  and  $K_x$ , but is a Bilinear Matrix Inequality (BMI). However, with a change of variables ( $Y = K_x Q_x$ ), this BMI can be converted to an LMI [3].

$$\begin{aligned} & \min \quad \beta \\ & \text{subject to} \quad Q_x A_i^T + A_i Q_x + 2\alpha_x Q_x - B_i Y - Y^T B_i^T < 0, (i = 1, 2, \dots, N) \\ & \quad I < Q_x = Q_x^T < \beta I \\ & \quad \begin{bmatrix} Q_x & Y^T \\ Y & \mu^2 I \end{bmatrix} > 0 \end{aligned}$$

With  $Q_x$ ,  $K_x$  is computed from  $K_x = Y Q_x^{-1}$  and  $K_p$  and  $K_d$  are obtained from  $K_x = [K_p \ K_d]$ . If  $K_p + K_p^T > 0$  and  $K_d + K_d^T > 0$  are not satisfied,  $\alpha_x$  and/or  $\mu$  need to be

relaxed. ( $\alpha_x$  needs to be decreased to allow for slower convergence, and  $\mu$  needs to be increased to permit larger inputs.) The control parameters used in the 2-DOF stabilization are:

$$\alpha_x = 2.0,$$

$$\mu = 0.1$$

$\alpha_x = 2.0$  is chosen as 1/10 of the bandwidth of the flaperon servo control in order to avoid interference between the dynamics of the flaperon servo control and the motion control. The time constant corresponding to  $\alpha_x$  is 0.5 seconds. This is an adequate number for the motion of the wind tunnel model.  $\mu = 0.1$  is determined as a result of iterations to make sure that the levels of the moment required from the virtual control do not exceed available moment.

The resulting parameters are:

$$Q_x = \begin{bmatrix} 2.1323 & 0.0000 & -1.5590 & 0.0000 \\ 0.0000 & 3.0992 & 0.0000 & -1.8975 \\ -1.5590 & 0.0000 & 3.3619 & -0.0000 \\ 0.0000 & -1.8975 & 0.0000 & 2.7152 \end{bmatrix} > 0$$

$$K_p = \begin{bmatrix} 0.0037 & 0.0000 \\ 0.0000 & 0.0355 \end{bmatrix}, K_d = \begin{bmatrix} 0.0003 & 0.0000 \\ 0.0000 & 0.0055 \end{bmatrix}$$

The gains ( $K_p, K_d$ ) are diagonal. This is not surprising, because the inertia properties of the model ( $I_{xz} = 0$  and  $I_y \approx I_z$ ) make the rigid body dynamics diagonal (Refer to (3.8)). Furthermore, all the nonlinear terms in (3.8) are very small due to the second property ( $I_y \approx I_z$ ). This means that the rigid body dynamics is comprised of two independent LTI systems ( $\phi$  and  $\gamma$ ). The initial response of the virtual control is shown in Figure 5.10. Both roll and "yaw" angles converge to the origin as designed. The levels of both roll moment ( $m_1$ ) and "yaw" moment ( $m_2$ ) are adequate in a sense that these moments are available from both actuations ( $C_\mu$  and  $\delta_f$ ).

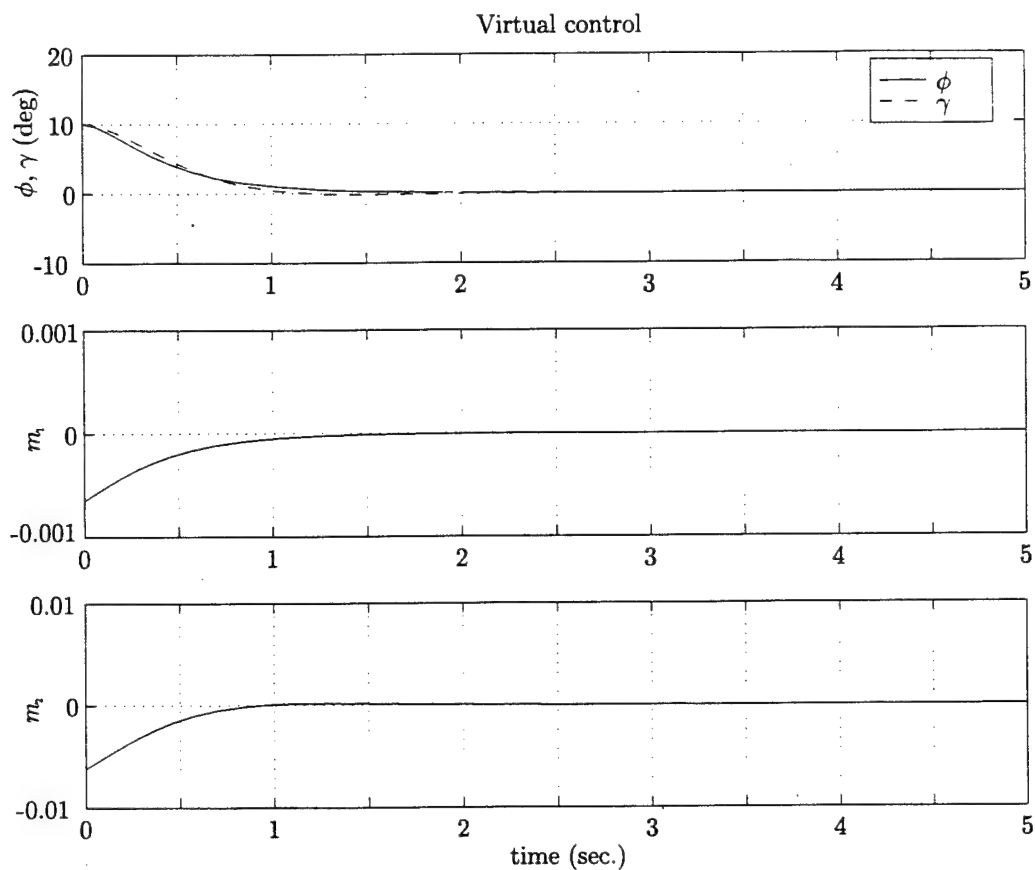


Figure 5.10: Virtual control (2-DOF stabilization)

### High-Gain Lyapunov Control

The control input ( $C_\mu$ ) is determined from (5.14). The parameters in (5.14) are as follows:

The scalar decay rate ( $\alpha_s$ ) of  $\|s\|_2$  is set to

$$\alpha_s = 10.0,$$

which is about 5 times faster than the virtual closed loop for the rigid body dynamics.

Lyapunov matrix  $P_s$  is chosen as

$$P_s = \begin{bmatrix} 1 & 0 \\ 0 & 0.01 \end{bmatrix}.$$

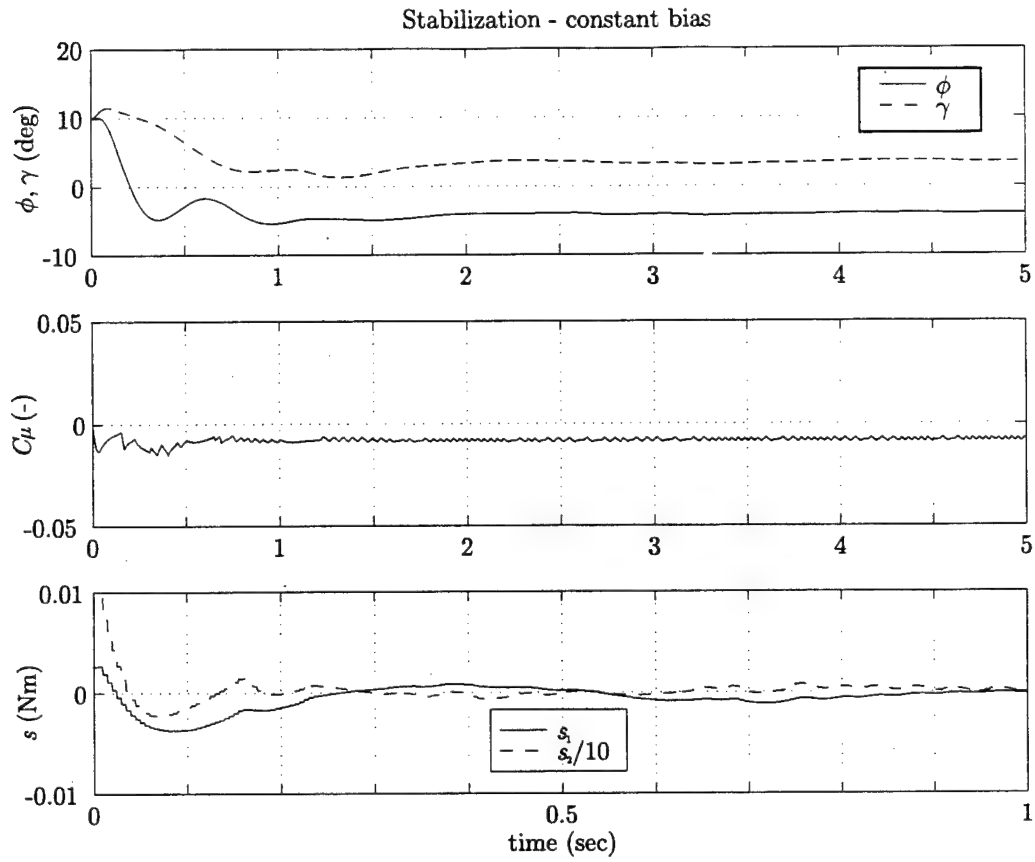


Figure 5.11: 2-DOF Stabilization (Simulation, bias error)

$P_s$  is chosen so that  $P_{s_{11}}s_1^2$  and  $P_{s_{22}}s_2^2$  are of the same order. This is done because  $|m_1|_{\max}/I_x$  and  $|m_2|_{\max}/I_z$  are comparable and  $I_x$  is about 1/10 of  $I_z$ . Therefore, the effect of  $m_2$  on the motion (the acceleration) is 1/10 of  $m_1$ . Therefore,  $s_1(= m_1 - k(x)_1)$  and 1/10 of  $s_2(= m_2 - k(x)_2)$  have the same level of impact on the motion. The design parameters are thus given as

$$\kappa_1 = 50.0, \kappa_2 = 100.0.$$

$$K_s = P_s \begin{bmatrix} \kappa_1 & 0 \\ 0 & \kappa_2 \end{bmatrix} \quad (5.22)$$

### Simulation Results

First, shown in Figure 5.11 is a result with constant bias error in  $C_\mu$  ( $\delta C_\mu = -0.001$  corresponding to  $\delta m_s \approx 80\%$  of full range at maximum). Second, a result with a periodic

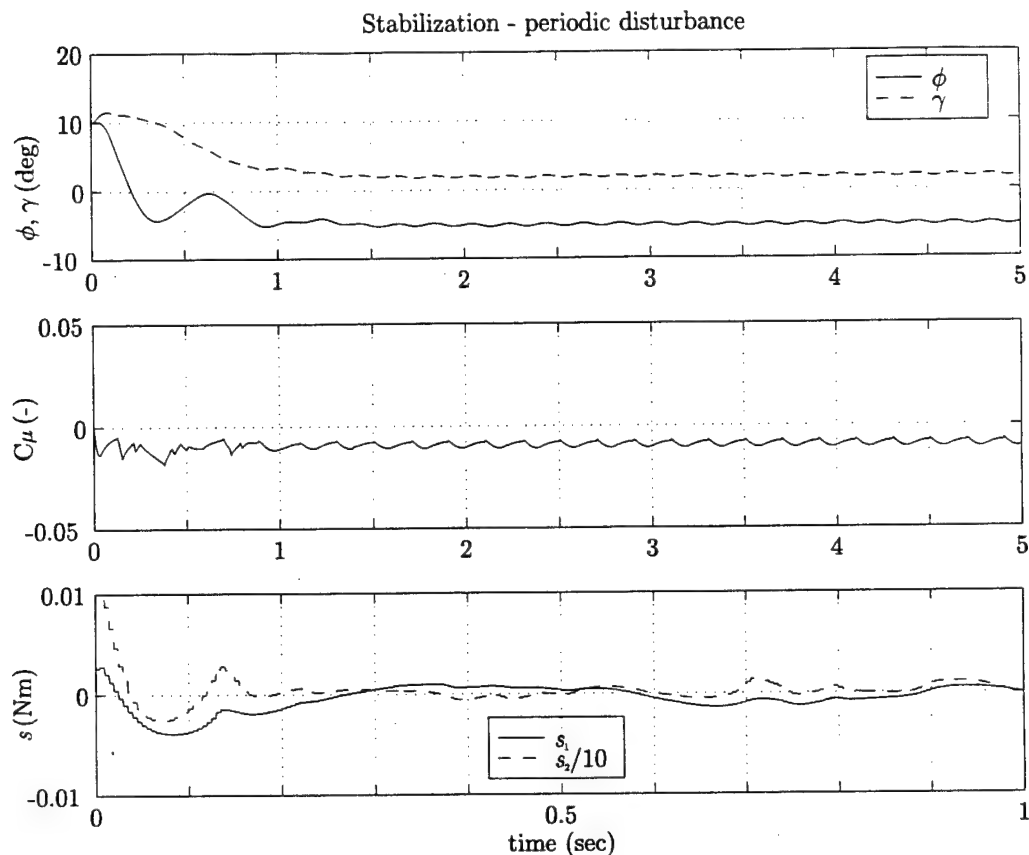


**Figure 5.12:** 2-DOF Stabilization (Simulation, periodic disturbance)

disturbance ( $\delta C_\mu = 0.001 \sin(2\pi \cdot 5t)$ ) in  $C_\mu$  is shown in Figure 5.12. In both cases, it is seen that despite large errors between the actual moment characteristics and nominal moment characteristics due to the errors, the system is stabilized with a small amount of blowing. Also, each component of  $s$  converges to a small number quicker than both  $\phi$  and  $\gamma$ . In Figure 5.12, it is observed that the periodic disturbance is effectively rejected. Overall responses of both  $\phi$  and  $\gamma$  are similar to the bias error case.

Only  $C_\mu$  is used as a control effector so far. In the next section, two inputs (blowing,  $C_\mu$  and flaperon,  $\delta_f$ ) are used to achieve set-point tracking of the FTB system.



### 5.3.2 Set-Point Tracking

Set-Point Tracking of the 2-DOF system with FTB and flaperons is discussed. In this case, the number of the inputs ( $= 2$ ) are equal to the dimension of  $m$  ( $= 2$ ). Therefore, a vector Lyapunov function is employed.

#### Virtual Control

PID control for rigid body dynamical systems gives semi-globally stabilizing control due to the passive nature of the rigid body [2]. As stated in the previous section, the rigid body dynamics of the FTB system is basically decomposed into two independent LTI systems. Therefore, the virtual control for set-point tracking is designed with simple pole assignment for each LTI system. The control parameters used in the 2-DOF set-point tracking are

$$K_p = \begin{bmatrix} 0.0206 & 0 \\ 0 & 0.4164 \end{bmatrix}, K_i = \begin{bmatrix} 0.0419 & 0 \\ 0 & 0.4854 \end{bmatrix}, K_d = \begin{bmatrix} 0.0027 & 0 \\ 0 & 0.1364 \end{bmatrix}$$

The step response of the virtual control is shown in Figure 5.13. Both roll and “yaw” angles achieve the set points ( $\phi = 20^\circ$ ,  $\gamma = 10^\circ$ ). Levels of both roll moment ( $m_1$ ) and “yaw” moment ( $m_2$ ) are also within actuator capability.

#### High-Gain Lyapunov Control

Each of the decay rates of  $s_i$ ,  $i = 1, 2$  is set to 10, which is about 10 times faster than the virtual closed loop for the rigid body dynamics. Thus, the vector of desired decay rates is simply

$$\alpha_s = [10 \ 10]^T.$$

#### Experimental Results

2-DOF set-point tracking experiments are conducted at a 100Hz sampling rate. The results are shown in Figure 5.14 and Figure 5.15. Figure 5.14 shows the data when  $\kappa$  is relatively small

$$\kappa = [40 \ 140]^T.$$

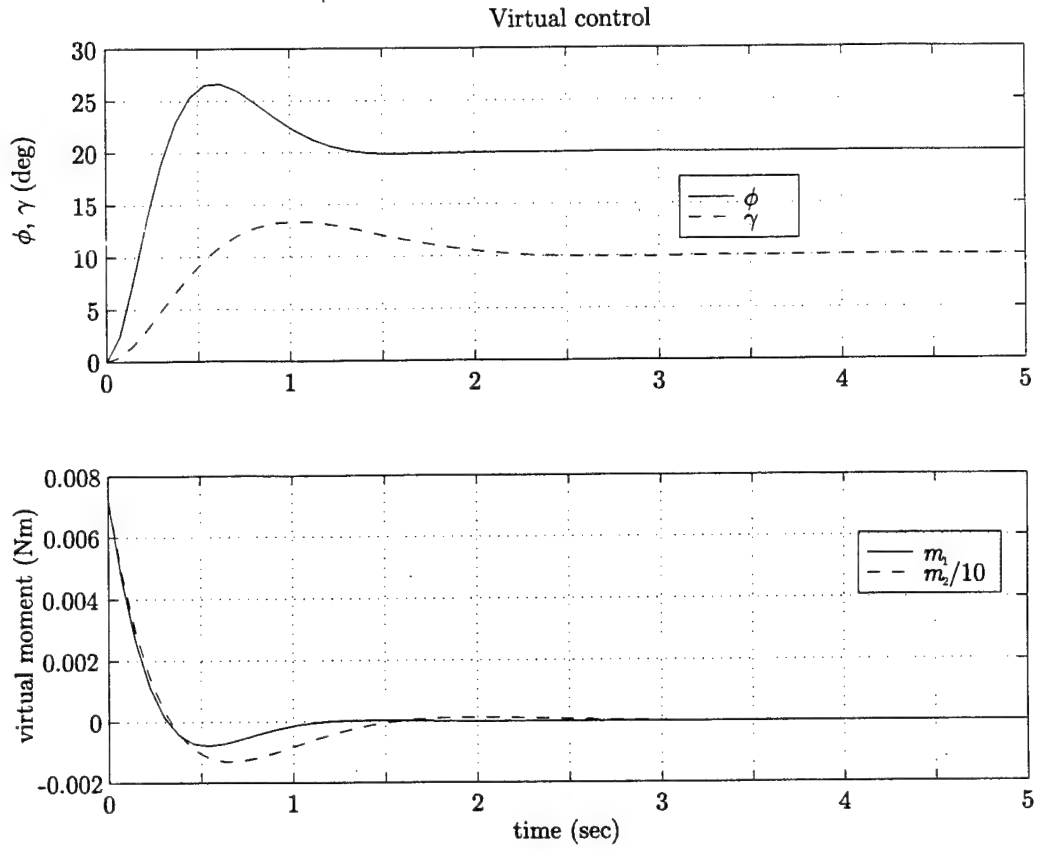


Figure 5.13: Virtual control (2-DOF set-point tracking)

Figure 5.15 represents a case where  $\kappa$  is  $\kappa = [400 \ 1400]^T$ . At this level  $\kappa$ , the control structure behaves like a conventional Bang-Bang control

$$\kappa = [400 \ 1400]^T.$$

In Figure 5.14, it is seen that the set-points ( $\phi = 20^\circ, \gamma = 10^\circ$ ) are achieved with smaller air usage (The average  $C_\mu = 0.01$  in  $t \in [0 \ 5]$ ) than in Figure 5.15 (The average  $C_\mu = 0.029$  in  $t \in [0 \ 5]$ ). Each component of  $s$  rapidly converges to within a small bound as depicted in Figure 5.14, while each component of  $s$  is contained in a small bound in Figure 5.15. The bounds of both  $\phi$  ( $\Delta\phi = 5.1^\circ$ ) and  $\gamma$  ( $\Delta\gamma = 1.7^\circ$ ) in the steady state in Figure 5.14 are degraded compared to the result of the Bang-Bang control ( $\Delta\phi = 2.5^\circ, \Delta\gamma = 2.1^\circ$ ). Also, note that the flaperons move very rapidly in order to cancel the roll moment generated by the small levels of blowing. The roll moment in the small levels of blowing is large and

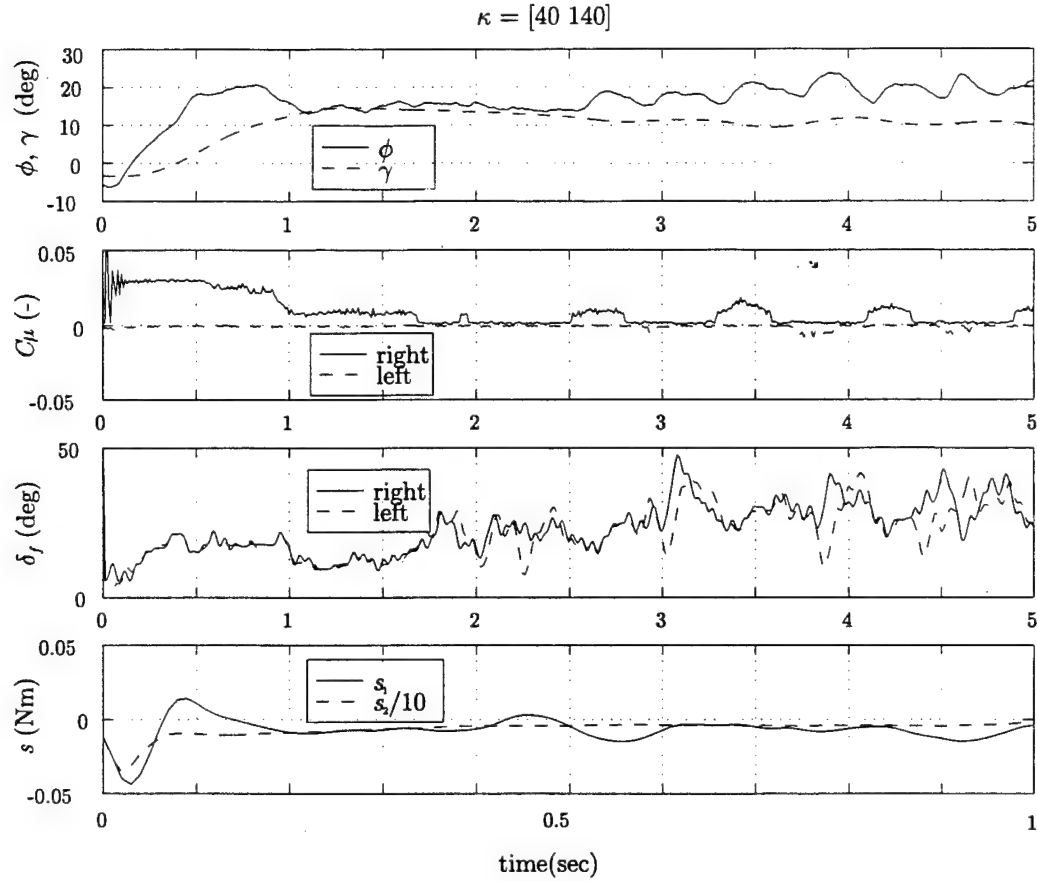


Figure 5.14: 2-DOF set-point tracking (Experiment),  $\kappa = [40 \ 140]$

rapidly changing with  $C_\mu$  (Section 3.3). On the other hand, the flaperons in the Bang-Bang control do not move rapidly due to the benign roll moment characteristics in the large levels of blowing. By comparing the two cases shown above, it is observed that with the smaller  $\kappa$ , the amount of air usage is reduced to about 1/3 while the bound of the controlled output is increased by a factor of two.

### 5.3.3 Summary of 2-DOF cases

For the stabilization of the 2-DOF system, simulations have been conducted under the assumption that the active torque cancellation (Appendix B) works perfectly. It has been shown that the 2-DOF system can be stabilized with small levels of blowing, *i.e.*, the effectiveness of the FTB has been fully exploited.

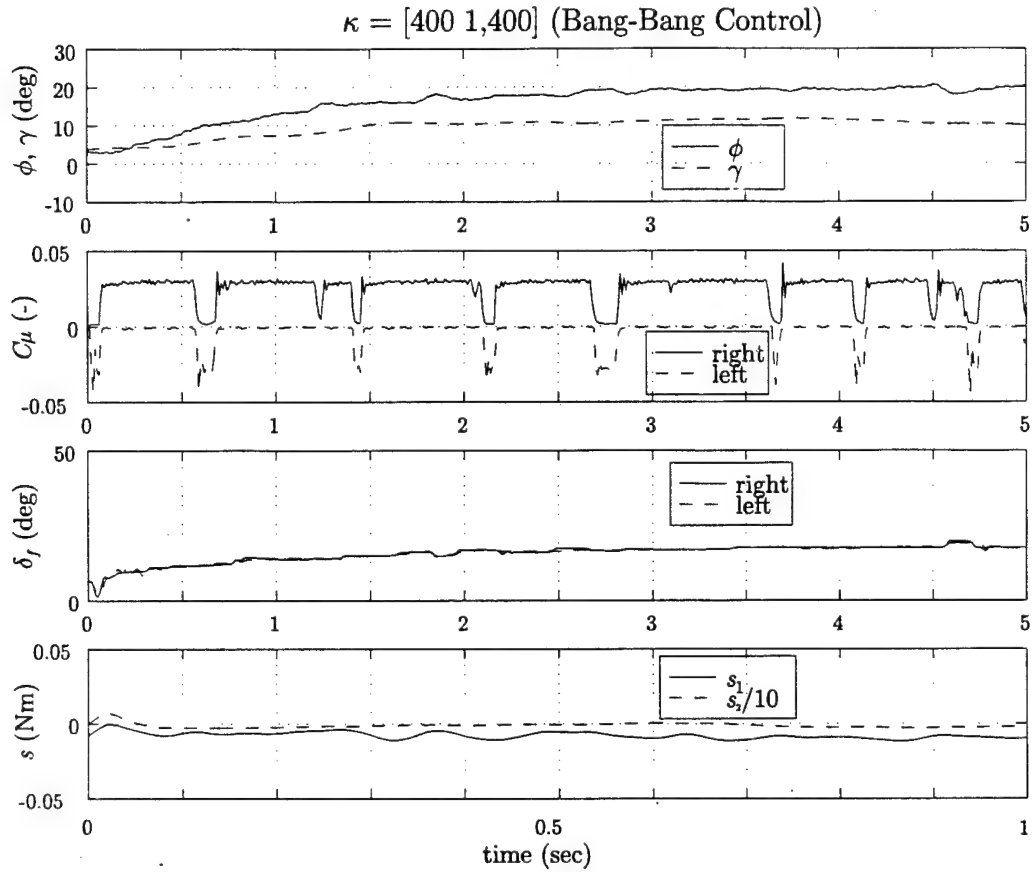


Figure 5.15: 2-DOF set-point tracking (Experiment),  $\kappa = [400 \ 1400]$  (Bang-Bang)

Experimental results in set-point tracking of the 2-DOF system with 2 inputs are provided. Again, it is observed that the nonlinear control approach makes it possible to exploit the effectiveness of small levels of FTB. As compared to a conventional Bang-Bang control, the air consumption reduces to about 1/3 while the bound of the controlled output is increased by a factor of two. In this case,  $C_\mu$  is used to control the “yaw” motion. As seen, for example, in Figure 3.1, the “yaw” moment characteristics is less highly nonlinear compared to the roll moment. That is, in order to obtain a large “yaw” moment, a large  $C_\mu$  is necessary. Therefore, the reduction in  $C_\mu$  is not as significant as in the 1-DOF roll case. However, according to a feasibility study of FTB [28],  $C_\mu = 0.01$  roughly corresponds to the maximum available normal bleed air from the engines. Therefore, the reduction in  $C_\mu$  from 0.03 to 0.01 is significant in this case.

## 5.4 Summary

The control approach developed in the previous chapter is applied to the FTB system in three configurations. In all cases, it has been shown that the nonlinear control approach can stabilize the FTB system and/or achieve the set points with small levels of blowing. However, the performance with the small usage of air is degraded compared to the conventional Bang-Bang control, which is a special case for the nonlinear control in the sense that the control structure becomes Bang-Bang control with large control parameters ( $\kappa$  or  $K_s$ ). Therefore, when the amount of air is very expensive and the degradation in performance can be tolerated, small parameters can be used to reduce the air usage. On the other hand, when the air usage is not expensive and the performance is critical, the Bang-Bang control should be used. In this way, the nonlinear control approach allows the trade-off between the performance and the control effort by tuning design parameters.

## Chapter 6

# Conclusions

In this final chapter, the results of this research are summarized and the main contributions are described. Also included are recommendations for future research.

### 6.1 Summary

This dissertation is on the development and experimental demonstration of a nonlinear approach to developing control laws for a class of uncertain nonlinear systems represented by a cascade connection of a nonlinear dynamical system and an uncertain linear dynamical system. The class of systems is motivated by an aircraft dynamics at high angles of attack incorporating Forebody Tangential Blowing (FTB).

FTB has been shown to be a very powerful means of generating forces and moments on aircraft operating in flight regimes where the effectiveness of conventional aerodynamic surfaces is reduced (e.g. post stall). Consequently, it provides a mechanism that could greatly expand the flight envelope of future aircraft systems.

The approach to control design developed in this thesis makes it possible for the first time to greatly reduce the amount of blowing required to control an aircraft model incorporating FTB.

The nonlinear control approach is based on combining High-Gain Control (HGC) and Lyapunov techniques. The structure of the control is similar to the standard successive loop closure. It can robustly invert highly nonlinear uncertain characteristics. The resulting control allows the system to operate in a region where characteristics are highly nonlinear and uncertain.

The design steps consist of three simple steps, and do not require information on the upper bounds of uncertainties in order to guarantee the stability of the system (boundedness of the states). If the information is available, the control parameters could be computed *a priori* that guarantee the required performance.

Also, a full dimensional Lyapunov function is not required to generate the control law. Only a low dimensional quadratic Lyapunov function is used. Therefore, the difficult process of finding a full dimensional Lyapunov function can be avoided. Further, this feature facilitates the real-time implementation of the control.

The nonlinear control design was applied to an aircraft model with FTB. Three configurations of the FTB system are used to demonstrate the utility of the approach. Simulation and experimental results were provided that showed the effectiveness of the approach. By successfully inverting the highly nonlinear and uncertain characteristics of FTB, the control allowed the FTB system to operate at low levels of blowing where FTB is powerful but highly nonlinear and uncertain. The design approach was shown to be able to fully exploit the FTB efficiency.

## 6.2 Conclusions and Contributions

The main contributions that became apparent in the course of the research are presented below.

**Development of Nonlinear Control Design:** A nonlinear control approach is developed that robustly controls a class of uncertain nonlinear systems. It has the following features:

- It is applicable to a class of nonlinear systems represented by a cascade connection of a nonlinear dynamical system and an uncertain linear dynamical system.
- It robustly inverts uncertain static nonlinearities.
- It consists of a few simple steps that allow two time-scale design. Virtual control, reduced order observer and High-Gain Lyapunov control comprise the procedures. The time-scale of each step can be specified so that time-scale separation can be introduced artificially.

- It does not require information on the bound of the uncertainties. If the information on the bounds is available, the design parameters can be computed *a priori* that guarantee the required performance.
- It requires only a low dimensional Lyapunov function. This not only simplifies the control design process, but also makes the real-time implementation feasible.
- It allows an explicit trade-off between the performance and the control effort by simply increasing or decreasing the design parameters while preserving the stability. Large design parameters yield a conventional Bang-Bang control structure.

**Application to FTB:** The control approach has been applied to the FTB system to exploit fully FTB efficiency. The highly nonlinear but powerful characteristics of FTB are exploited to achieve an effective use of FTB.

**Experimental Demonstration:** Independent set-point tracking control of 2-DOF system (roll and yaw angles) with FTB and flaperons at 45 degrees of nominal incidence has been successfully demonstrated experimentally.

- Air usage is reduced to about 1/3 while the bound of the controlled output increases by a factor of two compared to a conventional Bang-Bang control.

## 6.3 Recommendations

The following list describes recommendations for future study.

**Increase of DOF:** All the simulations and experiments are at most 2-DOF in this research. Actual aircraft are 6-DOF systems and FTB generates not only roll/yaw moment but also pitch moment, axial, side and normal forces. Investigation into multiple degrees of freedom is an interesting area of research. With the added complexity, new approaches such as neural networks may be necessary for finding the amount of blowing for stability/performance requirements. Also, interaction with existing control surfaces such as flaperons/elevators needs to be addressed.

**Adaptive Scheme for  $\kappa$**  The nonlinear control design proposed in this work can allow explicit trade-off between the performance and the control efforts while preserving



the stability. For all positive high-gain design parameter ( $\kappa$ ), the system is stable and  $\kappa$  determines the trade-off. In this work,  $\kappa$  is tuned and fixed thereafter. However,  $\kappa$  can be determined adaptively. In this case, since an additional loop for determining  $\kappa$  will be closed, the stability property needs reevaluation.

**Flexible Aircraft Dynamics** Actual moments acting on the aircraft model are estimated from equations-of-motion in this research. This is possible because the aircraft model is assumed rigid. However, in the case of flexible systems, this method is not applicable. More complicated estimation methods such as neural networks are required. Also, the stability proof relies on the condition that  $g(x)$  is affinely bounded. Flexible systems do not necessarily satisfy this condition.

**Multiple Sources of Uncertainties** Basically, in this work uncertainties are matched, *i.e.*, the uncertain static moments are matched with respect to the known manipulatable nominal static moments. If there exist large uncertainties such as parametric ones in the vehicle dynamics, those uncertainties are no longer matched with respect to the manipulatable input. In this case, a more complex approach such as backstepping is necessary.

## Appendix A

# Model Properties

The dimensions and mass/inertia properties of the wind tunnel model are summarized in this Appendix. Also included is the physical parameters used in simulations and experiments.

### A.1 Dimensions

The detailed dimensions of the wind tunnel model used in the experiments are shown in Figure A.1. The forebody portion of the model is the same one used in [34]. Refer to the reference for more information on the blowing slots. The nose tip radius, which affects the FTB characteristics significantly is 0.01 in and the fineness ratio is 1.98 [8].

Relevant geometric characteristics of the model are summarized in Table A.1.

Characteristics	Value
Conical forebody semi-apex angle	14 deg
Wing leading edge sweep angle	70 deg
Wing span, $b$	5.80 in
Wing planform area $S_{ref}$	23.11 in <sup>2</sup>
Wing aspect ratio $AR$	1.46
Mean aerodynamic chord, $MAC$	5.31 in
Tunnel blockage for $\alpha_0=45$ degrees	7 %
Tunnel blockage for $\alpha_0=90$ degrees	10 %

**Table A.1:** Geometric characteristics of the wing tunnel model

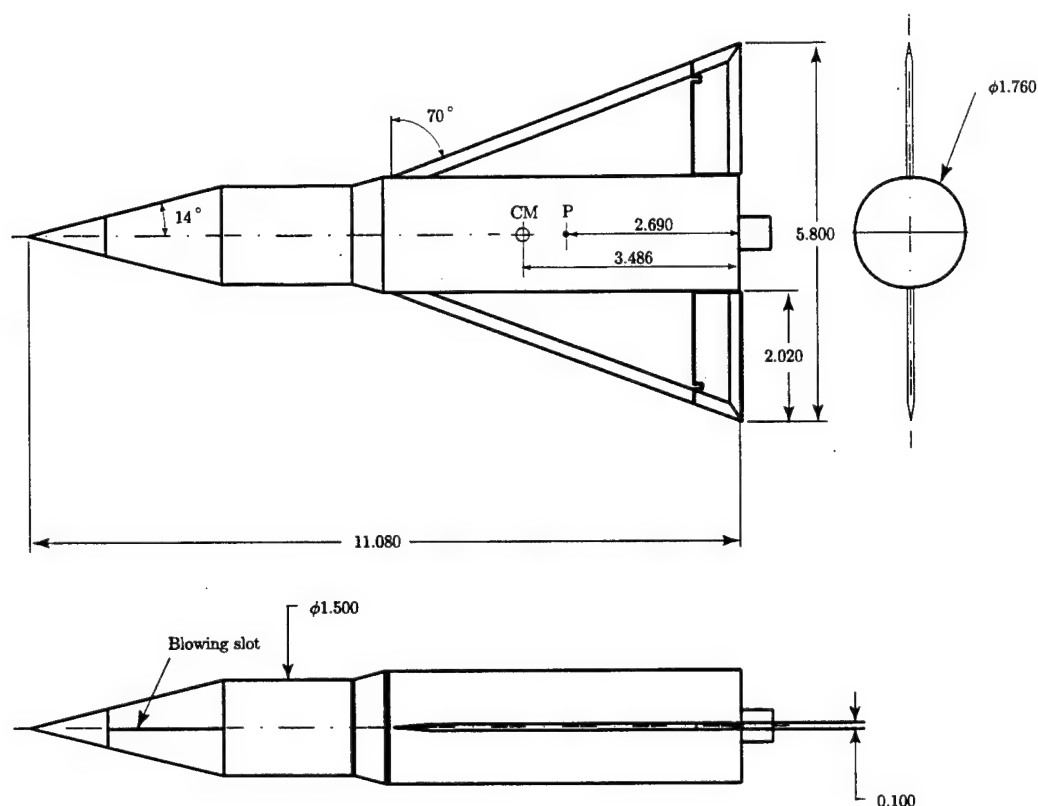


Figure A.1: Wind tunnel model - 3 view

## A.2 Mass/Inertia Properties

The mass and inertia properties are listed in Table A.2. The inertia of the model with respect to the orthonormal frame of reference with the origin of the center of mass were determined experimentally using a torsional pendulum [25]. The values of inertia about the point P are also included. The latter is used for the development of the equations of motion.

## A.3 Other Parameters

Other physical parameters used in simulations and experiments are summarized in Table A.3.

Inertia Component $kg, kgm^2$	Origin of Reference Frame	
	Point P	Center of mass
$I_x$	$(3.5620 \pm 0.29) \times 10^{-4}$	$(3.5620 \pm 0.29) \times 10^{-4}$
$I_y$	$(3.7067 \pm 0.05) \times 10^{-3}$	$(3.3782 \pm 0.03) \times 10^{-3}$
$I_z$	$(3.9531 \pm 0.05) \times 10^{-3}$	$(3.6246 \pm 0.03) \times 10^{-3}$
$I_{xy}$	0.0	0.0
$I_{yz}$	0.0	0.0
$I_{xz}$	$\approx 0.0$	$\approx 0.0$
<i>mass</i>	$0.8027 \pm 0.0001$	

Table A.2: Mass/Inertia Properties of the wind tunnel model

Parameters	Value
$V_\infty$	24.5 (m/s)
$I_A$	0.1772 (kgm <sup>2</sup> )
$c_{f1}$	$1.54 \times 10^{-3}$ (Nm/s)
$c_{f2}$	$1.10 \times 10^{-2}$ (Nm/s)
$\tau_1$	0.0200 (s)
$\tau_2$	0.0183 (s)

Table A.3: Other physical parameters

## Appendix B

# Active Torque Cancellation

Active torque cancellation (ATC) eliminates the effect of the gravity torque and reduces the effect of the large moment of inertia of the apparatus so that the motion of the aircraft model is dominated by aerodynamic loads. However, it does not try to eliminate the entire inertia of the supporting system (only 90 %) because the high accuracy for all the measurements and a very high bandwidth for the torque control are required and these are difficult to achieve.

### B.1 Hardware

Figure B.1 shows the schematic of ATC. The servo motor attached to the “yaw” shaft provides the torque for ATC that eliminates the effect of the gravity torque ( $m_g$ ) and reduces the effect of the large moment of inertia of the apparatus so that the motion of the aircraft model is dominated by aerodynamic loads ( $m$ ). The torque sensor [33] sends out the motor torque ( $m_m$ ) applied from the motor to the “yaw” shaft. The command torque ( $m_{m_c}$ ) to the motor is computed from  $\gamma$  and  $\ddot{\gamma}$ . The torque loop is formed to track the command torque using the feedback from the torque sensor. (Figure B.2)

### B.2 Inertia cancellation

For simplicity, a case where  $\phi \equiv 0$ ,  $m_g = 0$  and  $m_{f2} = 0$  in (3.2) is considered. (3.2) reduces to

$$(I_A + I_z)\ddot{\gamma} = m_2 + m_m \quad (\text{B.1})$$

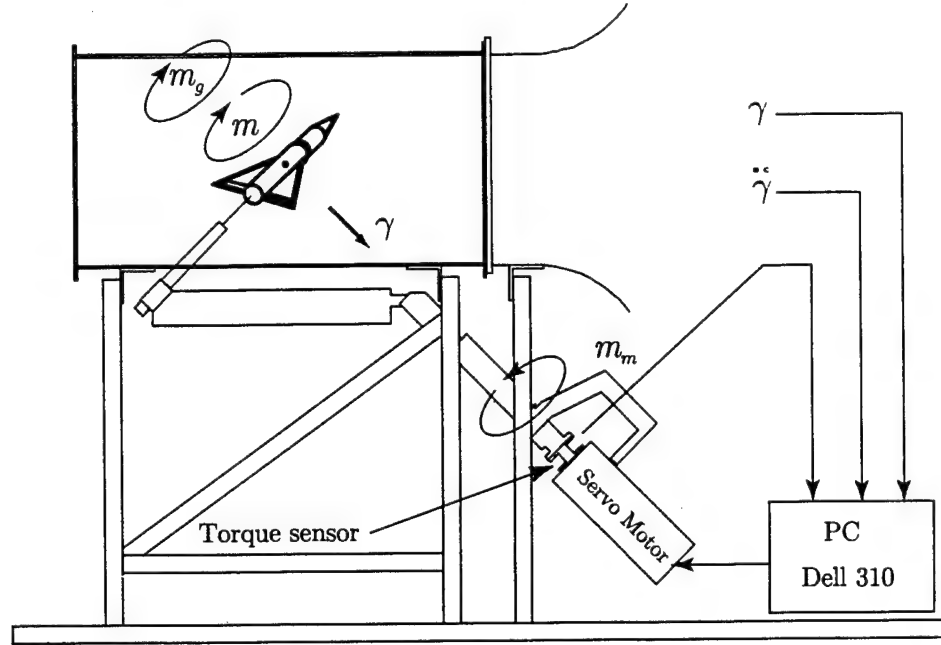


Figure B.1: Hardware of Active Torque Cancellation

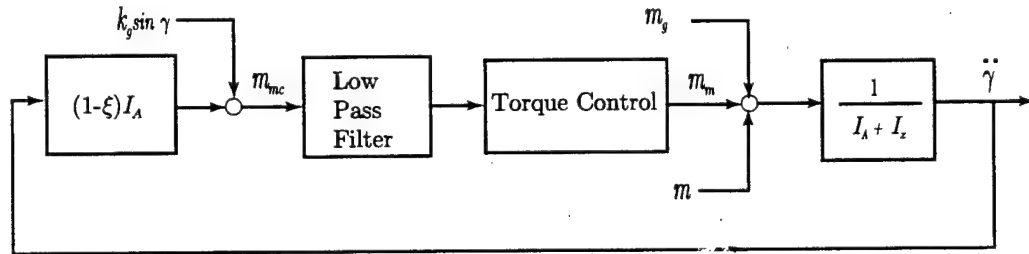


Figure B.2: Block Diagram of Active Cancellation

Ideally, ATC should instantly apply the torque equal to

$$m_m = I_A \ddot{\gamma} \quad (\text{B.2})$$

so that the resulting motion of the model is governed by the aerodynamic moment only,

$$I_z \ddot{\gamma} = m_2. \quad (\text{B.3})$$

However, it is impossible to apply the required torque in (B.2) instantaneously due to the limited bandwidth of ATC. The limitation of ATC stems from the limited bandwidth of the

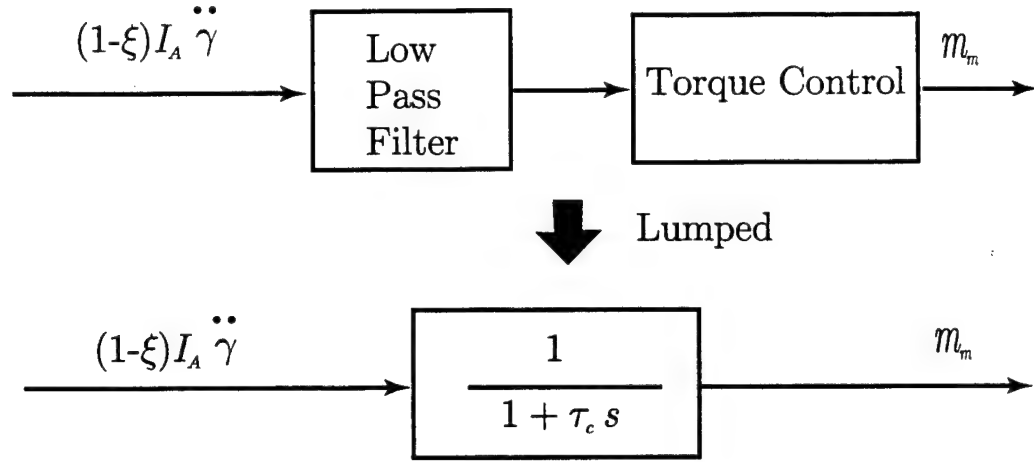


Figure B.3: Torque Command

torque control and the low pass filter required for cleaning noise-contaminated acceleration signal ( $\ddot{\gamma}$ ), from which the command torque is computed.

### B.2.1 Bandwidth of ATC

A first-order lag ( $\tau_c$ ) from the command torque to the actual torque applied from the motor is considered. The bandwidth of ATC is

$$(BW)_{ATC} \approx \frac{1}{\tau_c} \quad (B.4)$$

This is a lumped lag that includes the effect of the low-pass filter for  $\ddot{\gamma}$  and the limited bandwidth of the torque control (Figure B.3). Let  $\xi$  be the ratio of the inertia of the apparatus left uncanceled. ( $\xi=0$  means that the all inertia is cancelled.) The actual torque applied from the motor is expressed as follows:

$$m_m = \frac{1}{1 + \tau_c s} m_{m_c}, \quad (B.5)$$

where

$$m_{m_c} = (1 - \xi) I_A \ddot{\gamma}. \quad (B.6)$$

Substituting (B.5) and (B.6) into (B.1) gives the equations

$$\frac{\ddot{\gamma}_{ATC}}{\ddot{\gamma}_{ideal}} = \frac{1}{1 + \nu \frac{\xi + \tau_c s}{1 + \tau_c s}} \quad (B.7)$$

$$= \frac{1}{1+\nu} + \frac{\nu(1-\xi)}{(1+\nu)(1+\nu\xi)} \frac{1}{1 + \frac{1+\nu}{1+\nu\xi} \tau_c s}, \quad (\text{B.8})$$

where

$$\nu = \frac{I_A}{I_z} = \frac{0.1772}{3.9531 \times 10^{-3}} \approx 45 \quad (\text{B.9})$$

$$\ddot{\gamma}_{ideal} = \frac{m_2}{I_z}. \quad (\text{B.10})$$

From (B.8), the bandwidth of the acceleration due to ATC ( $\ddot{\gamma}_{ATC}$ ) is approximately obtained as

$$(BW)_{\ddot{\gamma}_{ATC}} \approx \frac{1+\nu\xi}{1+\nu} (BW)_{ATC}, \quad (\text{B.11})$$

since  $\frac{1}{1+\nu}$  term is very small ( $\approx 0.02$ ). In order to show that cancelling all the inertia of the supporting system is not feasible, let  $\xi$  be set to zero in (B.11). Then, we obtain

$$(BW)_{\ddot{\gamma}_{ATC}} = \frac{1}{1+\nu} (BW)_{ATC} \approx 0.02 (BW)_{ATC}. \quad (\text{B.12})$$

This implies that the bandwidth of the acceleration due to ATC ( $\ddot{\gamma}_{ATC}$ ) is about 1/50 of the bandwidth of ATC. A normalized step response ( $\frac{\ddot{\gamma}_{ATC}}{\ddot{\gamma}_{ideal}}$ ) is plotted as a solid line for  $\xi = 0$  in Figure B.4 when the bandwidth of ATC is 10 (Hz) ( $\approx 60$  (rad/s)). It is observed that the response is so slow that it will interfere with the motion control with the bandwidth of 1.2 (rad/s). (The bandwidth of the motion control is set around 1.2 rad/s (Chapter 5).) From the figure, it is concluded that even with the very fast ATC (time constant  $\approx 0.02$  sec.), the acceleration due to ATC can be very slow (time constant  $\approx 1.0$  sec.) due to the large inertia ratio ( $\nu$ ). This is problematic because the motion due to ATC should not interfere with the motion due to aerodynamics. ATC should work very quickly so that the motion is dominated by aerodynamic loads. The acceleration due to ATC should be at least five times faster than the bandwidth of the motion control so that the motion control can be designed on the basis of the frequency separation. This means that ATC should work much faster than the motion control. The bandwidth of ATC should be

$$(BW)_{ATC} \approx 50 \times 5 \times (BW)_{\text{motion control}} = 300 \text{ (rad/s)} \quad (\text{B.13})$$



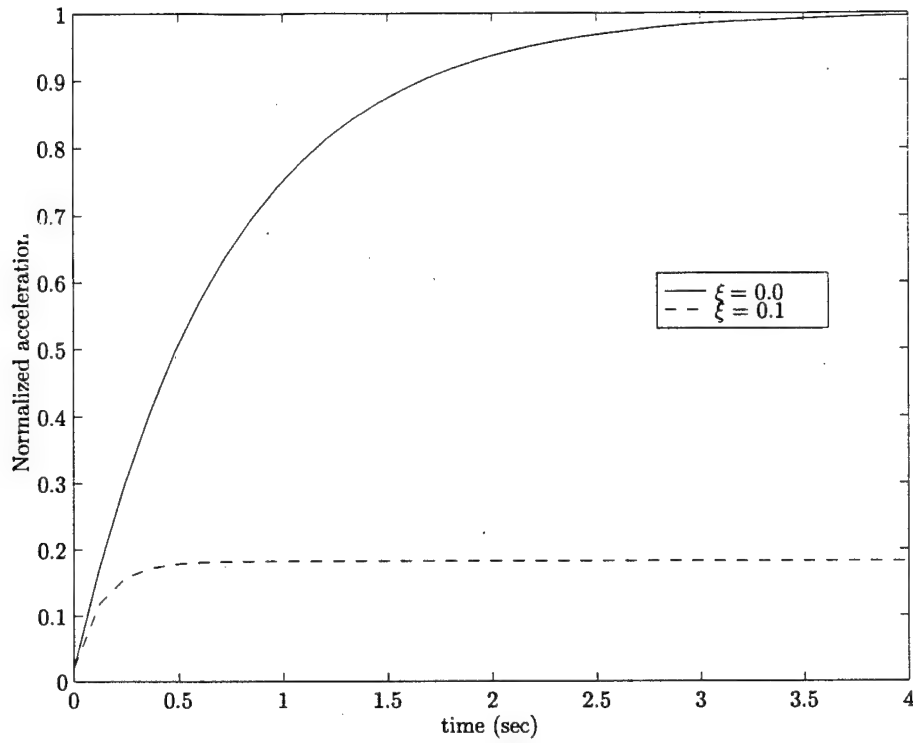


**Figure B.4:** Normalized step response of  $\ddot{\gamma}$

This level of high bandwidth of ATC is difficult to achieve because of the noise in  $\ddot{\gamma}$  signal and the limited bandwidth of the torque control. Therefore, cancelling all the inertia of the supporting system is not feasible.

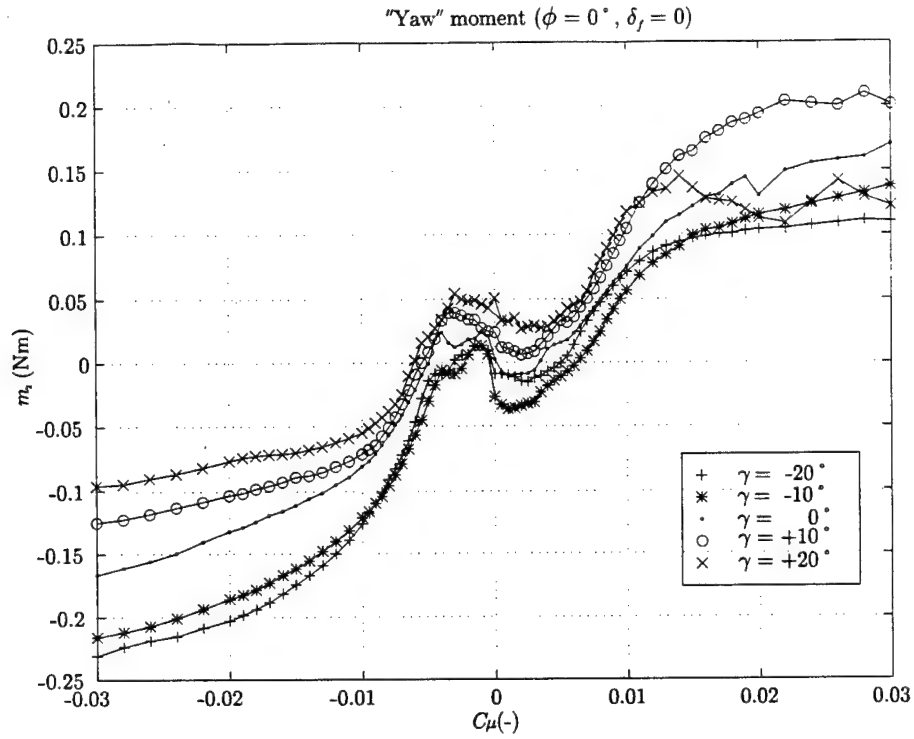
#### $\ddot{\gamma}$ signal

From (B.6), the command torque error due to the error in  $\ddot{\gamma}$  signal is expressed as

$$\delta m_m = (1 - \xi) I_A \delta \ddot{\gamma}. \quad (\text{B.14})$$

This error should be smaller than the aerodynamic moment in the frequency range of interest. Otherwise, the motion is disturbed by the torque originating from the error in  $\ddot{\gamma}$  signal. The error should be less than 1/10 of the available aerodynamic moment, *i.e.*,

$$(1 - \xi) I_A \delta \ddot{\gamma} < 0.1 \times 0.25 \text{ (Nm)} \quad (\text{B.15})$$

Figure B.5: "yaw" moment v.s.  $C_\mu, \gamma$  ( $\phi = 0^\circ, \delta_f = 0^\circ$ )

0.25 (Nm) is the maximum "yaw" moment due to FTB as shown in Figure B.5. Therefore,  $\delta\ddot{\gamma}$  needs to satisfy

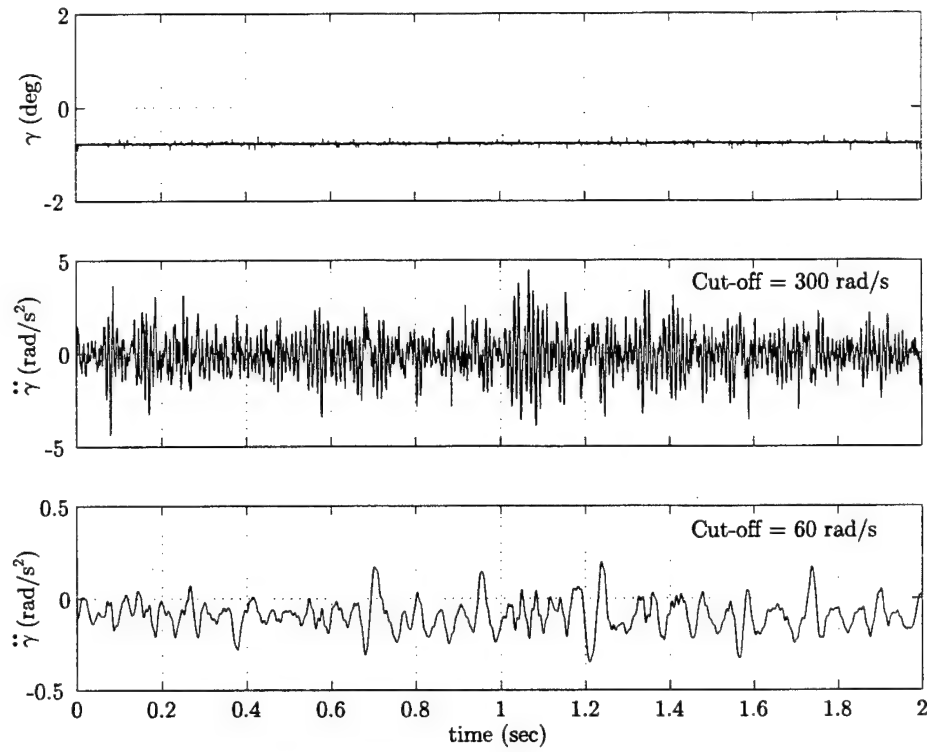
$$|\delta\ddot{\gamma}| < 0.025 \frac{1}{(1-\xi)I_A} \quad (\text{B.16})$$

$$\approx 0.141 \frac{1}{1-\xi} \quad (\text{B.17})$$

in the frequency range of interest. If  $\xi$  is set to zero, the following needs to hold up to 300 (rad/s) (From (B.13)):

$$|\delta\ddot{\gamma}| < 0.141 \text{ (rad/s}^2\text{)}. \quad (\text{B.18})$$

Figure B.6 shows the  $\ddot{\gamma}$  signal filtered with 300 and 60 rad/s cut-off frequency when  $\gamma$  axis is clamped at about  $-0.8^\circ$ . With a low pass filter (LPF) of 300 rad/s cut-off, the error in  $\ddot{\gamma}$  signal reaches 4 rad/s, which is about 30 times larger than the requirement of 0.141 rad/s. In order to achieve the high level of accuracy (0.141 rad/s<sup>2</sup>) for  $\ddot{\gamma}$  signal, an LPF of about 60 rad/s cut-off is required (assuming that  $\xi$  is small enough that the requirement of 0.141

Figure B.6: Filtered  $\ddot{\gamma}$ 

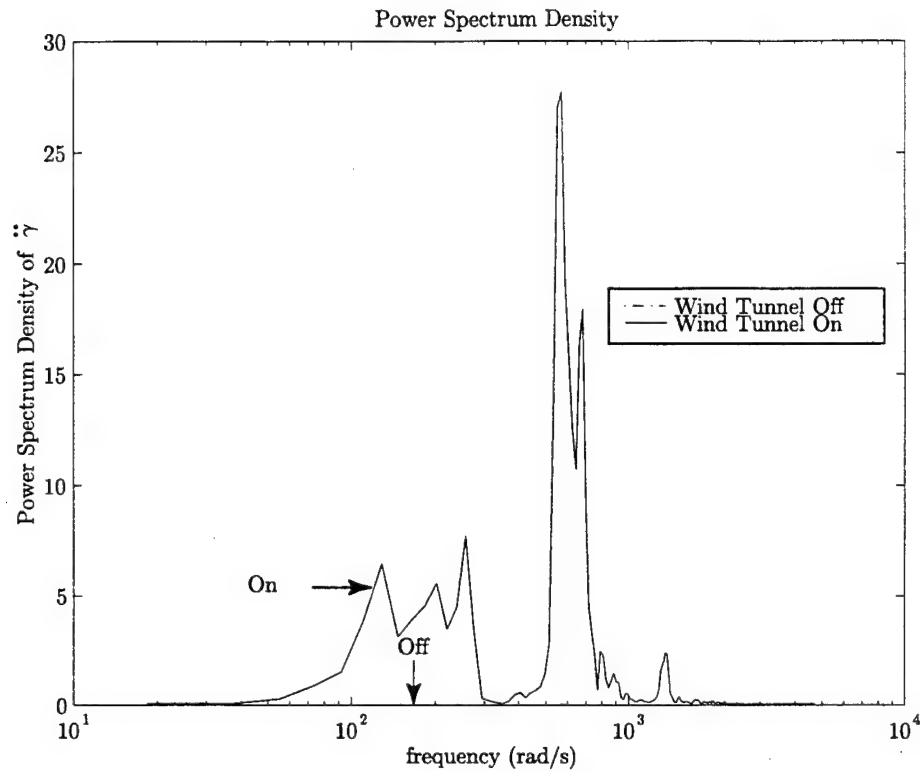
( $\text{rad/s}^2$ ) will not change significantly.). With an LPF of 60  $\text{rad/s}$  cut-off, the noise reduces significantly: the magnitude is thus

$$|\delta \ddot{\gamma}| = 0.2 (\text{rad/s}^2). \quad (\text{B.19})$$

This LPF is a part of the lag of ATC (Figure B.3):

$$(BW)_{ATC} \leq 60 \text{ rad/s}. \quad (\text{B.20})$$

Figure B.7 shows the power spectrum of the  $\ddot{\gamma}$  signal. From the power spectrum, it is observed that the noise power is strong beyond 100  $\text{rad/s}$ . The low frequency (less than 300  $\text{rad/s}$ ) contents of the noise come mainly from the vibration of the wind tunnel. This is difficult to reduce under the existing facility. Thus, an LPF with cut-off around 60  $\text{rad/s}$  is required to clean the signal.

Figure B.7: Power spectrum of  $\ddot{\gamma}$  signal

### Torque control

A normalized open-loop Bode plot from the torque motor driver to the torque sensor is depicted in Figure B.8. The plot is obtained by applying Pseudo Random Binary Signal [14] to the torque motor driver. It can be seen that up to 200 rad/s, the gain is flat and the peak is about 20 dB. Therefore, the torque control that achieves the bandwidth of about 60 rad/s can be designed with a pure integrator compensation. The step response to 0.5 (Nm) command of the resulting closed-loop (Figure B.9) is shown in Figure B.10. The time-constant is about 0.015 sec and it corresponds to 66 rad/s bandwidth.

#### B.2.2 Selection of $\xi$

Since the bandwidth of ATC is limited to about 60 rad/s. Cancelling the all inertia of the supporting system is not feasible. Shown in the following discussion is what percent of the supporting system can be uncanceled given the limited bandwidth of ATC, so that the

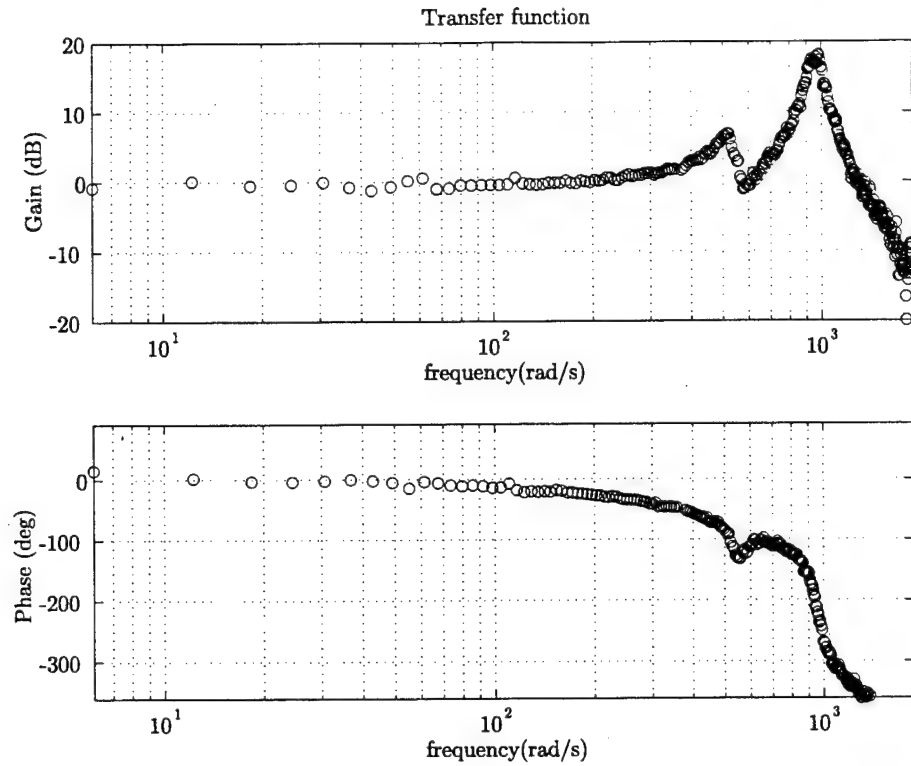


Figure B.8: Open-loop Bode plot of the torque characteristic

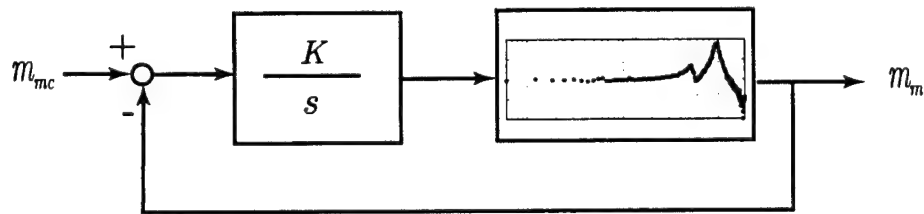


Figure B.9: Block Diagram of Torque Control

motion control design (e.g.  $\gamma$  control) with ATC working can be designed on the basis of the frequency separation. The requirements for the bandwidths are as follows:

$$(BW)_{\gamma_{ATC}} \approx 6.0 \text{ rad/s} \quad (\text{B.21})$$

$$(BW)_{ATC} \approx 60.0 \text{ rad/s} \quad (\text{B.22})$$

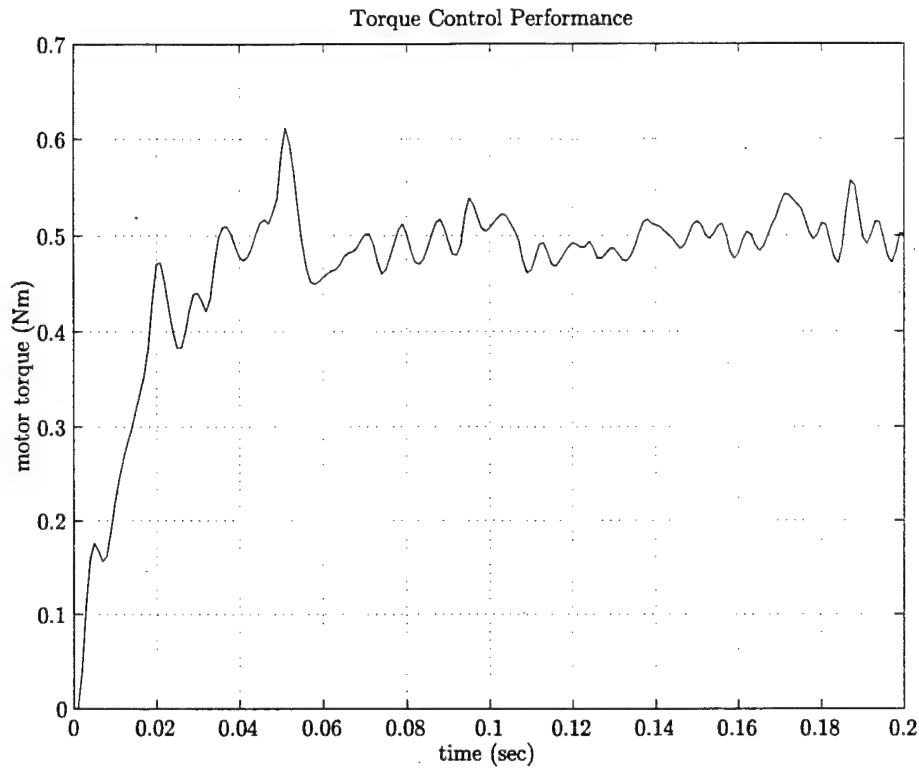


Figure B.10: Step response of torque control

where  $(BW)_{\ddot{\gamma}_{ATC}} \approx 6.0$  comes from the requirement that the bandwidth of the acceleration due to ATC is at least 5 times that of the motion control.  $(BW)_{ATC} \approx 60.0$  is from the limited bandwidth of ATC mainly from LPF requirement for cleaning the  $\ddot{\gamma}$  signal.  $\xi$  can be solved from (B.11) as

$$\xi = ((1 + \nu) \frac{(BW)_{\ddot{\gamma}_{ATC}}}{(BW)_{ATC}} - 1) / \nu \approx 0.1 \quad (\text{B.23})$$

With  $\xi = 0.1$ , a normalized step response  $(\frac{\ddot{\gamma}_{ATC}}{\ddot{\gamma}_{ideal}})$  is plotted in Figure B.4 as a dashed line when the bandwidth of ATC is  $\approx 60$  (rad/s). The level of the acceleration is small but the response is much faster than the case for  $\xi = 0.0$  and the interference of the motion control with the bandwidth of 1.2 (rad/s) can be avoided.

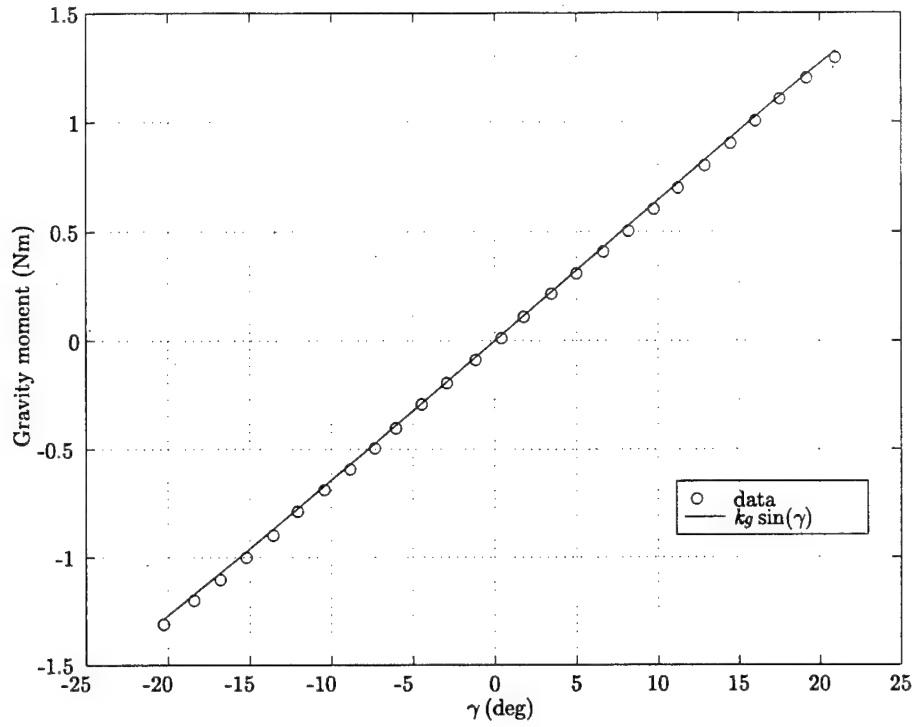


Figure B.11: Gravity torque

### B.3 Gravity torque cancellation

Gravity restoring torque can be expressed as

$$m_g = -k_g \sin(\gamma) \quad (\text{B.24})$$

where  $k_g$  can be determined from the total mass and the arm length from the center of mass to the “yaw” axis. However,  $k_g$  is determined from the experimental data using a least squares method because information such as mass and arm lengths are not exactly known. In Figure B.11, the comparison between data and the curve fit result is presented. The spring constant  $k_g$  is calculated as

$$k_g = 3.56 \text{ (Nm)}. \quad (\text{B.25})$$

Note that the bandwidth required for the inertia cancellation is sufficiently fast for the gravity torque cancellation.

# Bibliography

- [1] Richard J. Adams, James M. Buffington, and Siva S. Banda. Active vortex flow control for VISTA F-16 envelope expansion. AIAA94-3681CP, 1994.
- [2] Suguru Arimoto and Fumio Miyazaki. Stability and robustness of PID feedback control for robot manipulators of sensory capability. In *Proceeding of the 1st International Symposium of Robotics Research*, pages 783-799, 1983.
- [3] Stephen Boyd, L.EL Ghaoui, Eric Feron, and V.Balakrishnan. *Linear Matrix Inequalities in System and Control Theory*. Studies in Applied Mathematics, Vol.15. SIAM, 1994.
- [4] Zeki Z. Celik, Nelson Pedreiro, and Lenard Roberts. The control of wing rock by forebody blowing. AIAA93-3685, 1993.
- [5] Zeki Z. Celik, Nelson Pedreiro, and Lenard Roberts. Dynamic roll and yaw control by tangential forebody blowing. AIAA94-1853, 1994.
- [6] Zeki Z. Celik and Lenard Roberts. Vortical flow control on a wing-body combination using tangential blowing. AIAA92-4430, 1992.
- [7] Zeki Z. Celik and Leonard Roberts. Aircraft control at high-alpha by tangential blowing. AIAA92-0021, 1992.
- [8] Jonathan K Chow, Nelson Pedreiro, and Stephen M. Rock. The impact of forebody geometries at high-angles-of-attack with forebody tangential blowing. AIAA98-4522, 1998.
- [9] Jonathan K Chow and Stephen M. Rock. A nonlinear indicial response model for forebody tangential blowing at high angles of attack. AIAA99-4179, 1999.



- [10] Martin Corless. Control of uncertain nonlinear systems. *Journal of Dynamic System, Measurement and Control*, 115(1):362-372, 1993.
- [11] Martin J. Corless and George Leitmann. Continuous state-feedback guaranteeing uniform ultimate boundeness for uncertain dynamic systems. *IEEE Transaction on Automatic Control*, 26(5):1139-1144, 1981.
- [12] K.C. Cornelius, N. Pandit, R.F. Osborn, and R.W. Guyton. An experimental study of pneumatic vortex flow control on high angle of attack forebody model. AIAA92-0018, 1992.
- [13] Russel M. Cummings, Lewis B. Schiff, and John D. Duino. Experimental investigation of tangential slot blowing on a generic chined forebody. *Journal of Aircraft*, 32(4):818-824, 1995.
- [14] W. D. T. Davies. *System Identification for Self-Adaptive Control*. Wiley-Interscience, 1970.
- [15] Carlos Canudas de Wit and Bruno Siciliano. *Theory of robot control*. Springer Verlag, 1996.
- [16] Raymond A. DeCarlo, Stanislaw H. Zak, and Gregory P. Matthews. Variable structure control of nonlinear multivariable systems: A tutorial. *Proceedings of the IEEE*, 76(3):212-232, 1988.
- [17] Christopher Edwards. *Sliding Mode Schemes Using Output Information with Application to Heating Plant Problems*. PhD thesis, University of Leicester, 1995.
- [18] Christopher Edwards and Sparah K. Spurgeon. On the development of discontinuous observers. *International Journal of Control*, 59(5):1211-1229, 1994.
- [19] F. Esfandiary and H.K. Khalil. Stability analysis of a continuous implementation of variable structure control. *IEEE Transaction on Automatic Control*, 36(5):616-620, 1991.
- [20] Ken Gee, Yehia M. Rizk, and Lewis B. Schiff. Analysis of Tangential Slot Blowing on F/A-18 Isolated Forebody. *Journal of Aircraft*, 32(5):1040-1046, 1995.

- [21] S. Gutman. Uncertain dynamical systems - Lyapunov Min-Max approach. *IEEE Transaction on Automatic Control*, 24(1):437-443, 1979.
- [22] F. Hodgkin and N.J. Wood. Forebody flow control for extended high-angle-of-attack maneuvers. *Journal of Aircraft*, 35(2):212-217, 1998.
- [23] James C. Hung and Weibing Gao. Variable structure control of nonlinear systems: A new approach. *IEEE Transaction on Industrial Electronics*, 40(1):45-55, 1993.
- [24] John Y. Hung, Weibing Gao, and James C. Hung. Variable structure control: A survey. *IEEE Transaction on Industrial Electronics*, 40(1):2-22, 1993.
- [25] Steven Ims. Inertia measuring system, ARL Memo 75. Technical report, Stanford University Aerospace Robotics Laboratory, 1991.
- [26] I. Kanellakopoulos, Petar V. Kokotovic, and A.S. Morse. A toolkit for nonlinear feedback design. *Systems & Control Letters*, 18:83-92, 1992.
- [27] Hassan Khalil. *Nonlinear Systems*. Prentice Hall, second edition, 1996.
- [28] Ian Kroo and Leonard Roberts. Forebody tangential blowing for control at high angles of attack - feasibility study final report, JIAA TR-101. Technical report, Joint Institute for Aeronautics and Acoustics, 1991.
- [29] M. Krstic, I. Kanellakopoulos, and Petar V. Kokotovic. *Nonlinear and Adaptive Control Design*. Wiley-Interscience, 1995.
- [30] Grant Sur man Wong. *Experiments in the Control of Wing Rock at High Angles of Attack Using Tangential Leading Edge Blowing*. PhD thesis, Stanford University, 1992.
- [31] Riccardo Marino. High-gain feedback in non-linear control systems. *International Journal of Control*, 42(6):1369-1385, 1985.
- [32] T.T. Ng and G.N. Malcolm. Aerodynamic control using forebody strakes. AIAA91-0618, 1991.
- [33] Nelson Pedreiro. Development of an Apparatus for Wing Tunnel Dynamic Experiments at High- $\alpha$ , JIAA TR -119. Technical report, Joint Institute for Aeronautics and Acoustics, 1997.

- [34] Nelson Pedreiro. *Experiments in Aircraft Roll-Yaw Control Using Forebody Tangential Blowing*. PhD thesis, Stanford University, 1997.
- [35] Nelson Pedreiro, Stephen M. Rock, Zeki Z. Celik, and Leonard Roberts. Roll-yaw control at high angle of attack by forebody tangential blowing. AIAA96-0773, 1996.
- [36] Nelson Pedreiro, Stephen M. Rock, Zeki Z. Celik, and Leonard Roberts. Roll-yaw control at high angle of attack by forebody tangential blowing. *Journal of Aircraft*, 35(1):69-77, 1998.
- [37] Nelson Pedreiro, Yuji Takahara, and Stephen M. Rock. Aileron effectiveness at high angles of attack - interaction with forebody blowing. AIAA98-4518, 1998.
- [38] John Pye. *An Investigation of the Flap Edge Flow field*. PhD thesis, Stanford University, 1999.
- [39] D. M. Rao, C. Moskovitz, and D.G. Murri. Forebody vortex management for yaw control at high angles of attack. *Journal of Aircraft*, 24(4):248-254, 1988.
- [40] Fredrick W. Roos. Synthetic jet microblowing for vortex asymmetry management on a hemisphere-cylinder forebody. AIAA97-1111, 1997.
- [41] A.M. Skow, W.A. Moore, and D.J. Lorincz. Forebody vortex blowin - a novel concept to enhance the departure/spin recovery characteristics of fighter aircraft. *AGARD-CP*, 262(24):24-1-24-17, 1979.
- [42] J E. Slotine and W. Li. *Applied Nonlinear Control*. Prentice Hall, 1991.
- [43] S.K. Spurgeon. Non-linear control for uncertain systems. In *Proceeding of Institution of Mechanical Engineers*, volume 208, pages 205-213, 1994.
- [44] S.K. Spurgeon and R. Davies. Nonlinear control via sliding modes for uncertain non-linear systems. *Control-Theroy and Advanced Technology*, 10(4):713-736, 1994.
- [45] Vadim I. Utkin. *Sliding Modes in Control Optimization*. Springer Verlag, 1992.
- [46] D. Willams and J. Bernhardt. Proportional control of asymmetric forebody vortices with the unsteady bleed technique. AIAA90-1529, 1990.

- [47] S.P. Willams and K.P. Garry. An experimental investigation into yaw control at high alpha on a chined forebody using slot blowing. *Aeronautical Journal*, pages 355-363, 1996.
- [48] Y. Yongnian and et al. Active control of asymmetric forces at high incidence. *Journal of Aircraft*, 25(2):190-193, 1988.
- [49] Karkeung D. Young, Petar V. Kokotovic, and Vadim I. Utkin. A singular perturbation analysis of high-gain feedback systems. *IEEE Transactions on Automatic Control*, 22(6):931-938, 1977.
- [50] Stanislaw H. Zak and S. Hui. Output feedback variable structure controllers and state estimators for uncertain/nonlinear dynamic systems. *IEE Proceedings-D*, 140(1):41-50, 1993.